

**PROSPECTS OF LEPTOQUARK DISCOVERY  
WITH ATLAS AT THE LHC**

by

**Vikas Bansal**

B. Tech. in Engineering Physics, Indian Institute of Technology,  
Bombay, 2003

Submitted to the Graduate Faculty of  
the Department of Physics & Astronomy in partial fulfillment  
of the requirements for the degree of

**Doctor of Philosophy**

University of Pittsburgh

2009

UNIVERSITY OF PITTSBURGH  
DEPARTMENT OF PHYSICS & ASTRONOMY

This dissertation was presented

by

Vikas Bansal

It was defended on

August 24th 2009

and approved by

Dr. Vladimir Savinov, Professor, Department of Physics & Astronomy

Dr. Bard Ermentrout, Professor, Mathematics Department

Dr. Adam Leibovich, Professor, Department of Physics & Astronomy

Dr. Donna Naples, Professor, Department of Physics & Astronomy

Dr. Andrew Zentner, Professor, Department of Physics & Astronomy

Dissertation Director: Dr. Vladimir Savinov, Professor, Department of Physics &  
Astronomy

Copyright © by Vikas Bansal

2009

# PROSPECTS OF LEPTOQUARK DISCOVERY WITH ATLAS AT THE LHC

Vikas Bansal, PhD

University of Pittsburgh, 2009

Final states with high- $p_T$  leptons and jets are predicted by many Beyond the Standard Model (BSM) scenarios including leptoquarks, Left-Right Symmetry, various implementations of Grand Unification Theory (GUT), and other models. Such theoretical models extend the application of Quantum Field Theory to energies far above the Electroweak Symmetry Breaking (EWSB) energy scale and seek to provide a much more elegant and symmetric description of the fundamental forces. The implications of such models include possible answers to the origins of flavor,  $CP$  violation, baryogenesis, and other fundamental questions beyond EWSB.

This dissertation describes the study of leptoquarks in dielectron-jets final states in proton-proton collisions at a center of mass energy of 14 TeV using ATLAS apparatus at the Large Hadron Collider at CERN. The presented analysis is based on fully-simulated data samples that contain two or more high- $p_T$  electron candidates and jets for an integrated luminosity of 100 pb<sup>-1</sup>. Signal event selection, analysis algorithms, and suppression of SM backgrounds are discussed. ATLAS can discover leptoquarks up to masses of 565 GeV with a branching ratio ( $\beta$ ) of 1 at 100 pb<sup>-1</sup> at a  $5\sigma$  significance level.

## TABLE OF CONTENTS

<b>PREFACE</b> . . . . .	xvi
<b>1.0 INTRODUCTION</b> . . . . .	1
1.1 The Framework of Quantum Field Theory . . . . .	2
1.2 The Standard Model . . . . .	3
1.3 Beyond the Standard Model . . . . .	6
1.3.1 SuperSymmetry (SUSY) . . . . .	7
1.3.2 Grand Unified Theories (GUT) . . . . .	8
<b>2.0 INTRODUCTION TO LEPTOQUARKS</b> . . . . .	10
2.1 Leptoquark model . . . . .	12
2.2 Leptoquark production at the LHC . . . . .	14
2.3 Recent searches for leptoquarks . . . . .	16
<b>3.0 THE EXPERIMENTAL SETUP</b> . . . . .	18
3.1 The Accelerator . . . . .	20
3.2 The Detector . . . . .	22
3.2.1 Tracking . . . . .	24
3.2.2 Calorimetry . . . . .	27
3.2.2.1 LAr electromagnetic calorimeter . . . . .	28
3.2.2.2 Hadronic calorimeters . . . . .	31
3.2.3 Muon spectrometer . . . . .	32
3.2.3.1 The toroid magnets . . . . .	35
3.2.3.2 Muon chamber types . . . . .	35
3.2.3.3 Muon chamber alignment and B-field reconstruction . . . . .	36

3.2.4	Trigger, readout, data acquisition, and control systems . . . . .	37
3.2.4.1	Trigger system . . . . .	37
3.2.4.2	Readout architecture and data acquisition . . . . .	38
<b>4.0</b>	<b>PHYSICS SIMULATION AND EVENT RECONSTRUCTION . . . . .</b>	<b>40</b>
4.1	Hard Scattering processes at the LHC . . . . .	40
4.1.1	Factorization Theorem, Parton Showering and Hadronization . . . . .	41
4.2	Detector simulation . . . . .	43
4.3	Event Reconstruction . . . . .	45
4.3.1	ATLAS Software Infrastructure . . . . .	45
4.3.2	Reconstruction of Electrons and Photons . . . . .	47
4.3.3	Muon Reconstruction . . . . .	47
4.3.4	Particle Jet Reconstruction . . . . .	48
<b>5.0</b>	<b>SEARCH FOR LEPTOQUARKS IN DIELECTRON CHANNEL . . . . .</b>	<b>50</b>
5.1	$eejj$ Channel . . . . .	50
5.2	Signal simulation . . . . .	51
5.3	Backgrounds . . . . .	51
5.3.1	Physics backgrounds . . . . .	52
5.3.2	Mismeasurement Backgrounds . . . . .	53
5.4	First selection criteria of events . . . . .	53
5.5	Analysis . . . . .	54
5.6	Trigger . . . . .	58
5.7	Systematic Uncertainties . . . . .	60
5.8	Results . . . . .	64
<b>6.0</b>	<b>RECEIVER/MONITORING SYSTEM OF ATLAS . . . . .</b>	<b>68</b>
6.1	Introduction . . . . .	68
6.1.1	Receiver/Monitor System . . . . .	70
6.1.2	Performance tests . . . . .	76
<b>7.0</b>	<b>CONCLUSIONS . . . . .</b>	<b>88</b>
	<b>BIBLIOGRAPHY . . . . .</b>	<b>90</b>
	<b>APPENDIX A. ELECTRON IDENTIFICATION . . . . .</b>	<b>94</b>

A.1 Selection Criterion for <b>isEM</b> Identification . . . . .	94
<b>APPENDIX B. BACKGROUND CONTRIBUTION FROM SINGLE-TOP PRODUCTION . . . . .</b>	<b>101</b>

## LIST OF TABLES

1.1	The fundamental interactions in the Standard Model . . . . .	4
1.2	The fundamental fermions in the Standard Model . . . . .	4
2.1	Leptoquarks quantum numbers and couplings according to the BRW model . . . . .	14
3.1	Main parameters of the inner detector system. . . . .	26
3.2	Main parameters of the calorimeter system. . . . .	29
3.3	Main parameters of the muon spectrometer. Numbers in brackets for the MDT's and the RPC's refer to the final configuration of the detector in 2009. . . . .	34
5.1	NLO cross sections for scalar leptoquark pair production at the LHC. . . . .	51
5.2	Partial cross sections (pb) that survive the selection criteria for this analysis. The $Z/DY$ cross section is for the region $M_{ee} \geq 60$ GeV. The offline trigger efficiency for the signal events that pass all selection criteria exceeds 97% but is not included in this table. . . . .	62
5.3	Overall trigger efficiencies for the signal events that satisfy all the selection criteria. . . . .	62
5.4	Overview of the systematic uncertainties on the first generation leptoquark for a mass hypothesis of 400 GeV. . . . .	66
5.5	The integrated $pp$ luminosities at 14 TeV center-of-mass energy needed for a $5\sigma$ discovery for leptoquark at different mass hypotheses. . . . .	66

## LIST OF FIGURES

1.1	Leading order Feynman diagram for a process where an electron interacts with a photon. . . . .	3
1.2	Running of the SM gauge couplings as a function of the renormalization scale in MSSM (solid) and SM (dashed) cases. The supersymmetry mass scale is varied from 250 to 1000 GeV. . . . .	9
2.1	Feynman diagram for perturbation theory vertex showing leptoquark, lepton, and quark coupling. . . . .	11
2.2	Feynman diagrams showing a) FCNC via leptoquark coupling to the first and the second generations of leptons, b) (flavor conserving) neutral current mediated by the $Z$ boson in the SM whose prediction is consistent with existing experimental data. . . . .	13
2.3	Feynman diagram of a single leptoquark production. a) t-channel, b) s-channel	15
2.4	Feynman diagram of a pair-production of leptoquarks from a quark anti-quark annihilation. a) t-channel, b) s-channel . . . . .	15
2.5	Feynman diagrams of pair-productions of leptoquarks from gluon-gluon fusions.	16
2.6	Next-to-leading order cross-section for leptoquark pair production as a function of leptoquark mass. The cross-section is calculated for proton-proton collisions at 14 TeV center of mass energy using the parton distribution function set CTEQ6M. . . . .	17
3.1	Standard Model cross sections at the Large Hadron Collider. . . . .	19
3.2	Overview of the CERN accelerator complex . . . . .	20
3.3	Cut-away view of the ATLAS detector illustrating the various sub-detectors .	23

3.4	Plan view of a quarter of the ATLAS's Inner Detector showing each of the major detector components with its active dimensions and envelopes. . . . .	25
3.5	Cut-away view of the ATLAS calorimeter system. . . . .	28
3.6	Sketch of a barrel module where the different layers are clearly visible with their granularity in $\eta$ and $\phi$ . . . . .	30
3.7	Cut-away view of the ATLAS muon system. . . . .	33
4.1	Monte Carlo simulation of a typical event in proton-proton collisions. . . . .	40
4.2	A schematic diagram of a hard scattering process in a proton-proton collision. It shows the leading order production of a $Z$ boson subsequently decaying into hadrons born from a quark anti-quark pair ( $q\bar{q}$ ). Both perturbative and non-perturbative parts of the production and the decay process are represented including the decay of the resulting $q\bar{q}$ pair into the color-neutral final state particles during hadronization. The areas where the soft interaction is dominant, both within the colliding protons and during hadronization, are shaded in grey. . . . .	42
4.3	A sketch of the detector response to the final state particles. Lines in yellow indicate the region where particles primarily interact in the detector, e.g. electrons shown in the second row interact in the tracking chamber and the electromagnetic calorimeter with most of the activity being in the latter. . . . .	44
4.4	Material distribution ( $X_0, \lambda$ ) at the exit of the inner detector of ATLAS. The distribution is shown as a function of $ \eta $ and averaged over $\phi$ . The breakdown indicates the contributions of external services and of individual sub-detectors, including passive material that describes the detector infrastructure also found inside the active volumes. . . . .	45
4.5	Cumulative amount of material, in units of interaction length, as a function of $ \eta $ , in front of the electromagnetic calorimeters, in the electromagnetic calorimeters themselves, in each hadronic layer, and the total amount at the end of the active calorimetry of ATLAS. Also shown for completeness is the total amount of material in front of the first active layer of the muon spectrometer (up to $ \eta  < 3.0$ . . . . .	46

4.6	A graphical display that shows the results of the reconstruction of the final state objects from an MC simulation of an event where the pair-production of leptoquarks took place. Each leptoquark decays into an electron and a hadronic jet. Upper left hand-side region shows the cross-sectional view of ATLAS with the superimposed reconstructed energy clusters (in grey), as a function of $\phi$ , in the calorimeters (shown in green and orange annular rings). The corresponding tracks (cyan lines) are reconstructed in the inner detector (annular rings inside the calorimeters). The lower region of the figure shows the longitudinal view of ATLAS with reconstructed tracks in the inner detector (shown in the central part), as a function of $\eta$ . . . . .	49
5.1	Feynman diagrams for signal and background physics processes resulting in $eejj$ final states. . . . .	52
5.2	$S_T$ distribution from the signal and the background events after baseline selection. The signal is for a leptoquark mass hypothesis of 400 GeV. The distribution is normalized to an integrated pp luminosity of $100 \text{ pb}^{-1}$ . . . . .	55
5.3	$m_{ee}$ distribution from the signal and the background events after baseline selection. The signal is for a leptoquark mass hypothesis of 400 GeV. The distribution is normalized to an integrated pp luminosity of $100 \text{ pb}^{-1}$ . . . . .	56
5.4	Signal over background significance in the $S_T$ - $m_{ee}$ phase space obtained for a leptoquark mass hypothesis of 400 GeV assuming $\beta=1.0$ . . . . .	57
5.5	$M_{lj}$ versus the other $M_{lj}$ distribution for the signal and the background events after baseline selection. The signal is for a leptoquark mass hypothesis of 400 GeV. The distribution is normalized to an integrated pp luminosity of $100 \text{ pb}^{-1}$ . . . . .	58
5.6	$M_{lj}$ versus the other $M_{lj}$ distribution for the signal and the background events after the baseline selection and the optimized selections of $S_T$ and $m_{ee}$ . The signal is for a leptoquark mass hypothesis of 400 GeV. The distribution is normalized to an integrated pp luminosity of $100 \text{ pb}^{-1}$ . . . . .	59

5.7	Electron-jet invariant mass distribution for the signal and the background events after the baseline selection. Two entries per event are plotted corresponding to the two reconstructed leptoquark candidates. The signal is for a leptoquark mass hypothesis of 400 GeV. The distribution is normalized to an integrated pp luminosity of 100 pb <sup>-1</sup> . . . . .	60
5.8	Electron-jet invariant mass distribution for the signal and the background events after the baseline selection and the optimized selections of $S_T$ and $m_{ee}$ . Two entries per event are plotted corresponding to the two reconstructed leptoquark candidates. The signal is for a leptoquark mass hypothesis of 400 GeV. The distribution is normalized to an integrated pp luminosity of 100 pb <sup>-1</sup> . . . . .	61
5.9	5 $\sigma$ discovery potential for the first generation 400 GeV leptoquark versus $\beta^2$ with and without the background systematic uncertainty included. . . . .	67
5.10	Minimum $\beta^2$ of a scalar leptoquark versus leptoquark mass at 100 pb <sup>-1</sup> of integrated $pp$ luminosity at 14 TeV center-of-mass energy at 5 $\sigma$ (background systematic uncertainty included). . . . .	67
6.1	Block diagram depicting the architecture of the ATLAS LAr readout electronics. The lower box represents the calorimeters installed in their respective cryostat. The central box illustrates the schematics of the electronics used to read out the calorimeter. The upper box shows the off-detector electronics which include the trigger and the L1 interface (highlighted in green color box)	69
6.2	Diagram of the analog circuitry for one receiver channel. The (incoming) trigger sum cable is shown at the upper left, and the output to the cable leading to the L1 preprocessor is shown at the lower right. . . . .	71

6.3	Photograph of the receiver and the transition boards in a test setup. The signals enter on the right side at the front panel of the transition module. The elements through which the signals pass can be identified (right to left) as (1) input transformers, (2) backplane connectors, (3) VGA daughterboards, (4) remapping board, (5) voltage limiting circuitry, (6) output drivers, (7) output transformers, (8) output connectors on receiver motherboard, and (9) are drivers for monitoring channels. The SCDB, (10), is a special test bench version with a USB interface, permitting direct control of the receiver module with a computer. The monitoring line drivers are located just to the right of the SCDB. . . . .	73
6.4	Block diagram of the monitoring module. . . . .	75
6.5	VGA daughterboard test bench. . . . .	77
6.6	Left: DC response curves of the 16 channels of one VGA board, with all channels set at DAC=2700. The green horizontal lines represent the maximum signal amplitude received by the R/M system. The slope of each curve yields a value for the gain, which is plotted in the upper right hand graph. The integral nonlinearity is evaluated separately for the positive and negative portions of the response curve, and the values are plotted in the lower right hand graph. The lower set of points (all below 0.1%) are for the negative region and the upper set of points (between 0.2% and 0.3%) are for the positive region. The thick red line at 1% represents the specification for the nonlinearity for the entire electronics chain in the R/M system. . . . .	78
6.7	Gain and integral nonlinearity for each of the 16 channels of a single VGA board shown in LabView VI's front panel. . . . .	79
6.8	DAC linearity for each of the 16 channels of a single VGA board shown in LabView VI's front panel. . . . .	80
6.9	R/M system test bench. . . . .	81

6.10	Pulse linearity test of the 64 channels of a receiver board, with all the channels set at DAC=2047. Upper left: the response data for a bipolar pulse of 38 ns rise time. Lower left: the residuals of the linear fit of the response data. Upper right: gain value for each channel. Lower right: integral nonlinearity (for maximum output pulse height of 2.5 V) for each channel. . . . .	82
6.11	Graphical User Interface of the LabView-based program used to carry out test of receiver response to LAr calorimeter signals. . . . .	83
6.12	Graphical User Interface of the LabView based program used to carry out tests of VGA response to the LAr signals. . . . .	84
6.13	Receiver noise vs gain, as measured with a wideband RMS voltmeter at the receiver output. The solid curve is an evaluation of the noise model provided by the manufacturer of the vga chip for this particular circuit of receiver system. The points are the measurements. . . . .	85
6.14	Graphical User Interface of the LabView based program used to carry out the final QC/QA of the entire receiver crate. . . . .	87
A1	ATLAS calorimeters: longitudinal cross-sectional view. . . . .	95
A2	ATLAS calorimeters: $\eta$ coverage. . . . .	98
A3	The fraction of the electron's transverse energy in the first sampling layer of a hadronic calorimeter. The red contour defines the optimal selection on this discriminating variable. . . . .	98
A4	Ratio of energy deposited in $3 \times 7$ and $7 \times 7$ cells in $\eta \times \phi$ space of a second sampling layer of electromagnetic calorimeter. The red contour defines the optimal selection on this discriminating variable. . . . .	98
A5	RMS of pseudorapidity of cells in energy clusters weighted by cell energies as detected in the second layer of the electromagnetic calorimeter. The contour in red defines the optimal selection. . . . .	99
A6	The difference between the energy of the second "hottest" cell in the first sampling and the energy of the cell with the lowest energy deposit that lies in between the two cells with the largest energy deposits. The contour in red defines the optimal selection. . . . .	99

A7	The ratio of the energy of the second hottest cell in the first sampling of the electromagnetic calorimeter and the $E_T$ dependent threshold. The contour in red defines the optimal selection. . . . .	99
A8	The distribution of the shower shape width in the first sampling layer of the electromagnetic calorimeter. The contour in red defines the optimal selection. . . . .	99
A9	The distribution of the fraction of energy deposited in the core part of clusters from the first sampling layer of the electromagnetic calorimeter. The contour in red defines the optimal selection. . . . .	100
A10	RMS of pseudorapidity of cells in a energy cluster weighted by cell energies detected in the first layer of the electromagnetic calorimeter. The contour in red defines the optimal selection. . . . .	100

## PREFACE

Ever since I came to know about elementary particles, I have been fascinated by them. It was exhilarating to learn that scientists can actually probe the nature of matter at such microscopic length scales. This work is the effort to learn more about this exciting world and it has been made possible with the help and support of many people that I have been fortunate to have as colleagues and friends.

First and foremost I would like to thank my PhD adviser Prof. Vladimir Savinov. He has been an exceptional mentor. I have learnt more than just physics from him. He has been encouraging all along this course. I could always approach him with any question I had. He entertained all my questions with so much interest that I was never afraid of asking a question that I feared might be perceived as too trivial.

During the course of this work, I find myself fortunate to have worked first-hand on ATLAS calorimeter electronics, both at the University of Pittsburgh and at CERN, Geneva, where I spent almost half of my time as a graduate student. My learning experience on electronics was enhanced with the help I received from Prof. Savinov and Prof. Cleland at Pittsburgh, and later, while I was working at CERN, from Dr. Boulahouache (Rice University), Dr. Wilkens (CERN), Dr. Simion (LAL, Paris) and Dr. Dannheim (MPI, Germany).

My stay at CERN was fruitful. It was my pleasure to meet and to work with so many people at CERN from whom I have learnt so much about physics, the LHC, the ATLAS apparatus and the software infrastructure. I am especially grateful for the help I received from Akira Shibata (New York University), Amir Farbin (University of Arlington, Texas) and Kyle Cranmer (New York University). I am also thankful to Denis Damazio (BNL), Attila Krasznahorkay (CERN), and Teresa Fonseca Martin (Royal Holloway, London) for their help and useful discussions of the ATLAS trigger.

I cannot end this note without thanking Julia Hoffman (Southern Methodist University (SMU), Texas), who has been always there to answer my questions related to electrons and physics analysis in general. Ketevi Assamagan (BNL), David Joffe (SMU), Renat Ishmukhametov (SMU), Ning Zhou (Columbia University, New York), Moustapha Thioye (Yale University), and Vakhtang Tsulaia (Pittsburgh) have also been very helpful.

I am also grateful to my friends, Sugata Bhattacharya and Niraj Welikala, for proofreading this work.

Finally, I would like to thank my parents who have supported and encouraged me all along.

## 1.0 INTRODUCTION

Our quest to understand Nature goes back to times immemorial. A major quantum leap occurred in 17th century when Sir Issac Newton formulated Newton's laws of motion and Newton's law of universal gravitation. Since then we have seen many developments that have made us all the more interested in unfolding the mysteries of Nature and today, we believe, we stand at the verge to finally understand how the universe came about. The fundamental questions we are seeking answers to include what are the tiniest constituents of matter and what is the origin of their mass.

A revolutionary experiment in this context was performed by Rutherford in the 1900s when he scattered alpha particles off gold atoms. It became evident that atoms were made of a tiny nucleus which is 5 orders of magnitude smaller in size than an already tiny atom. Since then we have continued to learn that the nucleus itself is a composite particle made of protons and neutrons and which themselves are made of quarks and gluons. In fact, a sub-field of physics better known as the High-Energy Physics (HEP) has evolved to specifically probe these particles in the minutest of details. In the past century a theoretical framework has been realized to explain all the elementary particles, such as electron and quarks, that we observe in Nature. It is known as the Standard Model of particle physics or simply the Standard Model. It describes how the fundamental building blocks of matter, the elementary particles, come together to form the material world of which we ourselves are a part. It does so by describing the fundamental forces that bind them together. As far as we know there are four fundamental forces, the most familiar to us is gravity. The other three forces are the strong force (it holds the protons and the neutrons in atomic nuclei and the quarks in the protons and the neutrons together), the electromagnetic force (it holds atoms together), and the weak force (it gives rise to radioactive decays).

The following section briefly describes the framework of Quantum Field Theory which forms the basis of the Standard Model.

## 1.1 THE FRAMEWORK OF QUANTUM FIELD THEORY

While classical mechanical systems are completely described by their Lagrangians, quantum systems with variable number of particles (*i.e.* when creation and annihilation of particles are taken into account) are described using Lagrangian density. Formulating the theory as a Lagrangian density instead of a total Lagrangian ensures the *locality* of the theory.

In addition it is required that

- The Lagrangian must be invariant under Lorentz transformations and translations (Poincaré invariance).
- The theory fulfills *microcausality* (which is closely linked to *locality*) which states that physically observable quantities at space-like separated points must commute.
- Physical quantities at space-like separated points must be independent.
- The spectrum of the Hamiltonian (*i.e.* the energy) is bounded from below.

The following equations shows the Lagrangian density of a free massless spin one-half field denoted by  $\psi$

$$\mathcal{L} = i\bar{\psi}(x)\gamma^\mu\partial_\mu\psi(x). \quad (1.1)$$

Here  $\psi$  is the column matrix representing a spin-half particle field as a function of variable  $x$  and  $\gamma^\mu$  stands for the gamma matrices ( $\gamma^0, \gamma^1, \gamma^2, \gamma^3$ ).

A Lagrangian typically contains terms that correspond to free fields and terms that describe their interactions with each other. Perturbation theory can be used to describe these interactions to all orders in the strength of the respective coupling parameter provided the strength is small. Individual contributions to the perturbative expansion are elegantly represented by Feynman diagrams. Fig. 1.1 shows a leading order Feynman diagram for a process in quantum electrodynamics, a quantum field theory that describes electrically

charged particles and photons, where an electron interacts with a photon. A thorough introduction to quantum field theory can be found elsewhere [1].

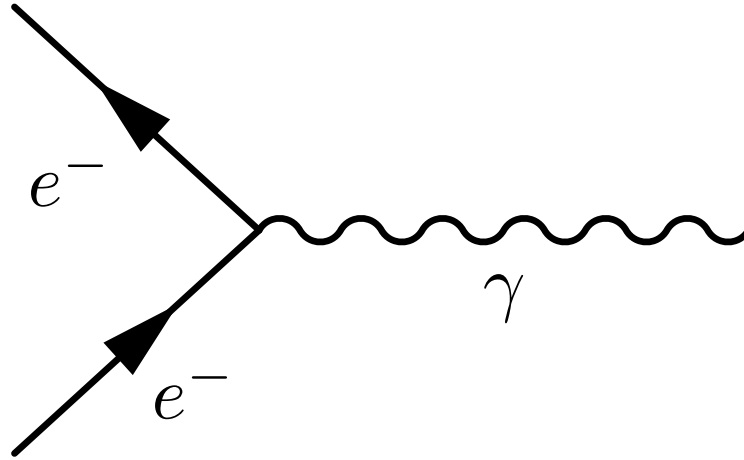


Figure 1.1 Leading order Feynman diagram for a process where an electron interacts with a photon.

## 1.2 THE STANDARD MODEL

The Standard Model (SM) of particle physics describes the behavior of the subatomic world that is controlled by three of the four fundamental forces (except gravity) in the framework of renormalizable gauge theories. In the SM the forces between the fundamental particles (fermions) are mediated by the exchange of (virtual) gauge vector bosons, which are related to the gauge symmetries of the SM. The fundamental gauge bosons and the forces described by the SM are listed in Table 1.1 and the SM fermions in Table 1.2. For each particle there exists a corresponding anti-particle with the same mass and spin but opposite electric charge (and color, in case of the QCD). For example, a positron is the anti-particle of an electron.

The group structure of the SM is

$$SU(3)_C \times SU(2)_L \times U(1)_Y, \tag{1.2}$$

where  $U(n)$  denotes the group of all unitary  $n \times n$  matrices and  $SU(n)$  is the group of all unitary  $n \times n$  matrices with the determinant 1. The weak and electromagnetic interaction (called electroweak interactions) are unified in the gauge group  $SU(2)_L \times U(1)_Y$ . Through

Interaction	boson	$Q_{\text{EM}}$	related group
electromagnetic	$\gamma$	0	$SU(2)_L \times U(1)_Y$
weak	$Z^0$	0	$SU(2)_L \times U(1)_Y$
	$W^\pm$	$\pm 1$	
strong	8 gluons g	0	$SU(3)_C$

Table 1.1 The fundamental interactions in the Standard Model. The value of the electromagnetic charge,  $Q_{\text{EM}}$ , is given in multiples of the elementary charge unit.

	Generations			$Q_{\text{EM}}$	Interactions		
					el.magn.	weak	strong
Quarks	$\begin{pmatrix} u \\ d \end{pmatrix}$	$\begin{pmatrix} c \\ s \end{pmatrix}$	$\begin{pmatrix} t \\ b \end{pmatrix}$	+2/3	yes	yes	yes
				-1/3	yes	yes	yes
Leptons	$\begin{pmatrix} \nu_e \\ e \end{pmatrix}$	$\begin{pmatrix} \nu_\mu \\ \mu \end{pmatrix}$	$\begin{pmatrix} \nu_\tau \\ \tau \end{pmatrix}$	0	no	yes	no
				-1	yes	yes	no

Table 1.2 The generations of fundamental fermions in the Standard Model. The value of the electromagnetic charge,  $Q_{\text{EM}}$ , is given in multiples of the elementary charge unit.

a process called spontaneous symmetry breaking, the bosons of the weak interactions ( $Z^0$ ,  $W^\pm$ ) acquire masses ( $M_W = 80.41$  GeV,  $M_Z = 91.187$  GeV), whereas the photon remains massless.

Quantum chromodynamics (QCD) describes strong interactions as an exact  $SU(3)_C$  gauge symmetry. The fundamental charge of QCD is called “color”. The force carriers of the color interactions are the massless gluons that form a color octet. Three colors are assigned to each quark, making it a fundamental triplet representation of  $SU(3)_C$ . Free gluons have not been observed experimentally and quarks seem to be primarily confined in colorless packages of two (mesons) and three (baryons) units. Leptons do not carry color charge and are hence singlet representations of  $SU(3)_C$ . All quarks and leptons are subject to the weak force. The electrically charged fermions participate in electromagnetic interactions, described by the theory of quantum electrodynamics (QED).

The SM has been probed down to length scales of  $10^{-18}$  m. No deviations from its

predictions have been found so far. There are, however, many open questions and problems, some of which are listed below:

- *Higgs Boson.* The massive scalar Higgs boson has been introduced in the SM to explain the electroweak symmetry breaking ( $SU(2)_L \times U(1)_Y \rightarrow U(1)_{em}$ ) and origin of particle masses. Gauge bosons and fermions are assumed to obtain their masses through interaction with the Higgs field. So far the Higgs boson has not been observed. The LEP II experiments (Aleph, Delphi, L3 and Opal) excluded the SM Higgs with masses up to  $M_H = 114$  GeV [2]. Recently Tevatron experiments (DØ and CDF) ruled out a Higgs mass around 170 GeV [3].
- *Fine-tuning problem.* Radiative corrections to the Higgs boson mass have quadratic divergences. At large scales, the corrections to the Higgs mass are many orders of magnitude larger than the Higgs mass itself.
- *Particle masses.* The masses of the quarks and the leptons are among the 19 free parameters, which are not predicted by the SM and have to be determined experimentally. In particular the wide spread in the masses of the leptons (from  $\approx 10^{-2}$  eV for the neutrinos up to 1.78 GeV for the tau lepton) and the quarks (from a few MeV for the  $u$ -quark up to 175 GeV for the top quark) is puzzling.
- *Neutrino Masses.* In the SM neutrinos are massless. However, recent data from solar, atmospheric and reactor neutrino experiments provided solid evidence for neutrino oscillations, which could occur for non-zero neutrino masses only.
- *Generation problem.* The existence of three families of quarks and leptons is not explained by the SM.
- *Gravity.* The SM does not include the gravitational force and it is not understood why the strength of gravity is 36 orders of magnitude weaker than that of the electromagnetic force.

It is widely believed that the SM is only a low energy approximation of a more complete theory. A popular hypothesis for such theory is SuperSymmetry (SUSY) which answers some of the questions posed above, in particular, the fine-tuning problem (see next section). Our current understanding of the fundamental forces implies that the running coupling constants

of the three SM forces might converge to the same value at higher energies that would indicate that the known three SM forces are just different incarnations of the same unified force. Theoretical ideas developed to address this and related issues belong to the class of Grand Unified Theories(GUTs). Any search for deviations from the SM is often also a search for Grand Unification.

### 1.3 BEYOND THE STANDARD MODEL

The Standard Model has been remarkably successful in describing the observed data so far but it is now known to be incomplete, *e.g.* recent discovery of neutrino oscillations remains to be explained. There are also other reasons that are outlined in the previous section to search for a more complete, unified theory of fundamental interactions. Let me elaborate on one of the open questions, namely, the fine-tuning problem. The SM needs scalar particles (Higgs bosons) to spontaneously break gauge symmetry of the SM which gives rise to masses of fundamental fermions and vector bosons. However, the mass of scalar Higgs boson is subject to quadratic divergence in the perturbation theory based on the principles of quantum mechanics. In lowest order of the perturbation theory

$$m_H^2 = m_0^2 + \delta m_H^2 \approx m_0^2 - g^2 \Lambda^2, \quad (1.3)$$

where  $m_H$  is Higgs boson's mass,  $m_0$  is bare mass parameter for the Higgs boson,  $g$  is a dimensionless coupling constant, and  $\Lambda$  is the energy scale. The mass of the Higgs boson is predicted to be comparable to the empirical electroweak scale ( $\approx 250$  GeV). So if  $g^2 \approx 1$  and  $\Lambda$  is as large as  $M_{GUT}$  ( $10^{16}$  GeV) or  $M_{Planck}$  ( $10^{19}$  GeV) then  $m_0^2$  must be fine tuned so that the two terms in equation 1.3, each of which is of the order of  $10^{30}$  GeV<sup>2</sup>, cancel each other so precisely that  $m_H$  is  $\approx 250$  GeV. Though it is not impossible, such fine tuning of the values of the input parameters is usually assumed to be rather unnatural. SUSY helps to solve this problem.

### 1.3.1 SuperSymmetry (SUSY)

SUSY [4] is a symmetry relating fermions to bosons and vice-versa. It introduces a supersymmetric partner called the sparticle for every particle in the SM, with its spin differing by  $\frac{1}{2}$  unit. All other quantum numbers between particle and its corresponding sparticle are the same. A fundamental difference between fermions and bosons is their spin quantum number. Fermions have half-integer spins and hence obey Fermi-Dirac statistics whereas bosons have integer spin and hence obey Bose-Einstein statistics. Therefore, changing the spin of a fermion by  $\frac{1}{2}$  unit makes it a boson and changing the spin of a boson by the same amount makes it a fermion. In the language of SUSY, *e.g.* the electron's supersymmetric partner is called the selectron and a photon's partner of half-integer spin is the photino.

The simplest supersymmetric extension of the SM is the “Minimal Supersymmetric Standard Model (MSSM)”. “Minimal” means that it introduces only a minimal necessary number of new particles. The salient feature of this model is that the  $(\text{mass})^2$  of scalar bosons is no longer quadratically divergent. For each scalar boson particle loop, there is a fermionic partner loop. Contributions from the two loops cancel each other in perturbative calculations therefore eliminating the need for fine-tuning.

The MSSM introduces a new quantum number called  $R$ -parity. It is similar to the parity quantum number but is obtained from product of three other quantum numbers. It distinguishes the SM particles from their super partners. SM particles have  $R = +1$ , while their SUSY partners carry  $R = -1$ .  $R$  parity is defined, *e.g.*, as

$$R = (-1)^{3B+L+2S}, \tag{1.4}$$

where  $B$  is the particle's baryon number,  $L$  is its lepton number and  $S$  is its spin. For example, an electron has  $B = 0$ ,  $L = 1$  and,  $S = 1/2$ , therefore it has  $R = -1^2 = +1$ , and a selectron has  $B = 0$ ,  $L = 1$ , and  $S = 0$ , therefore it has  $R = -1^1 = -1$ . In the MSSM model,  $R$ -parity is conserved which implies that sparticles are produced in pairs (as  $R$ -parity is a multiplicative quantum number just like parity  $P$ ). Hence MSSM predicts that an extremely long-lived lightest supersymmetric particle, usually referred to as the LSP, should exist. LSPs are also one of the candidates for the dark matter.

### 1.3.2 Grand Unified Theories (GUT)

GUT-inspired models unify the strong, the weak, and the electromagnetic interactions into one interaction. Group-theoretically speaking this means that the gauge structure of the SM is just the result of some symmetry breaking that has split a higher-order gauge symmetry group (that had only one gauge coupling constant, *i.e.* one force associated with it) into three smaller groups of the SM. This unification is predicted to occur at an energy scale of ( $10^{16}$  GeV) at which all the three interactions would have the same coupling strength. This unification is called Grand Unification. Fig. 1.2 shows the SM coupling of the three gauge groups ( $\alpha_i^{-1}$ ) according to the renormalization group equations as a function of the renormalization group scale for the SM (dashed) and for the MSSM (solid). In the case of the SM, the three running coupling constants do not intersect. This means that the SM alone can not predict possible Grand Unification. To explain Grand Unification some new quantum fields are necessary to be introduced in the intermediate energy scale. The solid lines on the figure show the same couplings but with the inclusion of the MSSM corrections that are implemented above a certain scale (where SUSY breaks down to the SM). Below that scale, the couplings are those we know in the SM, above that scale, the couplings gradually converge to the same value at higher energies. The gauge couplings are then one universal coupling above the GUT scale while below it they break down into the three known SM gauge couplings.

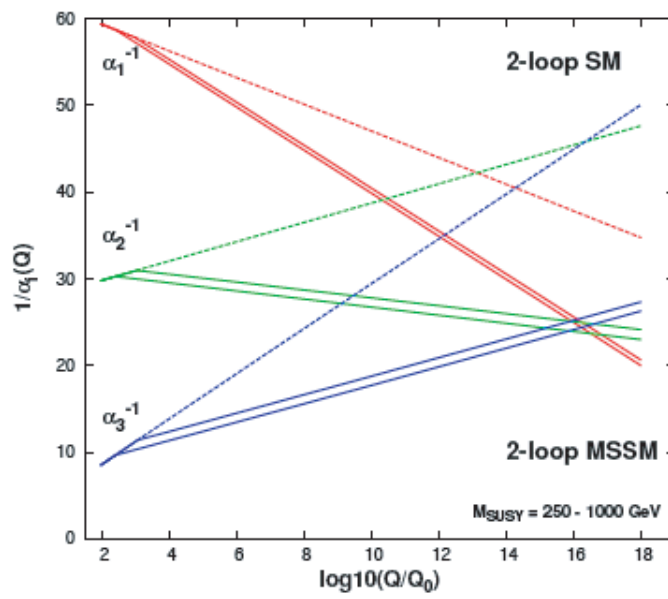


Figure 1.2 Running of the SM gauge couplings as a function of the renormalization scale in MSSM (solid) and SM (dashed) cases. The supersymmetry mass scale is varied from 250 to 1000 GeV.

## 2.0 INTRODUCTION TO LEPTOQUARKS

There is a remarkable symmetry in the generation structure between the quark and the lepton families, c.f. 1.2. This symmetry leads to cancellation of triangle anomalies that makes the standard model a renormalizable theory. This may indicate that quarks and leptons are interrelated at a more fundamental level. There are many GUT-inspired models that unify leptons and quarks into a single multiplet and hence require them to interact with each other via gauge bosons that are naturally called leptoquarks. In all such models, leptoquarks carry both lepton and baryon numbers, have fractional electric charges, and are color triplets under  $SU(3)_C$ . In models where the baryon and the lepton numbers are separately conserved, leptoquarks do not couple to diquarks which prevents the proton from decaying promptly. In such models, leptoquarks could have a relatively small mass (of the order of the electroweak scale). Notice that if leptoquarks coupled to diquarks, to prevent rapid proton decay, their masses would have to be at the GUT scale.

This chapter briefly describes some models predicting the existence of leptoquark-like particles.

Leptoquarks were originally introduced in the  $SU(4)$  Pati-Salam GUT-inspired model [5], where quarks are assumed to carry four “colors”: three of these are the conventional “color” quantum numbers, and the fourth represents the lepton number  $L$ . This unified picture of baryonic and leptonic matter arises by extending the  $SU(3)$  gauge symmetry to  $SU(4)$ . As a result, the transition between the “fourth color” and the “conventional color” is mediated by gauge bosons carrying both baryonic and leptonic quantum numbers, *i.e.* by leptoquarks.

The strong-coupling standard model (SCSM) predicts leptoquarks as bound states of quarks and leptons [6]. In this model, the electroweak part of the SM (*i.e.*  $SU(2)_L \times U(1)_Y$ ) is reconsidered in the context of the strong coupling. The salient feature is that SCSM

predicts the SM-like world below the electroweak symmetry breaking energy scale, but above it the bound states of quarks and leptons could exist, where the interaction between them would be communicated by leptoquarks.

In the strongly-interacting model of Technicolor, in a close analogy to the role of pions in low-energy strong interactions, the role of leptoquarks is played by technipions [7].

Leptoquark-like couplings appear in some SUSY models, c.f. 1.3.1. Squarks in  $R$ -parity violating models could experience leptoquark-like decays through Yukawa couplings. The  $\tilde{u}$  and  $\tilde{d}$  squarks (which are bosons with spin 0) can have leptoquark couplings. For instance, the  $\tilde{u}_L$  (the super-partner of the left-handed up-type quark) couples to  $\nu_e + u$  or  $e^- + d$  pairs, just like leptoquarks of electric charge  $-1/3$ . As a general consequence, it is possible to translate the constraints on the Yukawa coupling ( $\lambda_{lq}$ ) of the  $lq - l - q$  vertex, see figure 2.1, obtained from leptoquark searches into the constraints on the couplings of squarks in  $R$ -parity violating SUSY models.

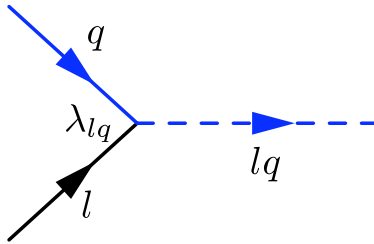


Figure 2.1 Feynman diagram for perturbation theory vertex showing leptoquark, lepton, and quark coupling.

$SU(5)$  is the smallest group that can contain the standard model and accommodate gauge bosons that “transform” quarks into leptons and vice versa. These  $SU(5)$ -based unified models, e.g. [8], also predict that these gauge bosons, also known as  $X$  and  $Y$  bosons, couple to diquarks and hence are required to be very massive ( $10^{10} - 10^{15}$  GeV) to avoid the rapid proton decay which is ruled out by experiments. However, if additional constraints are applied to  $SU(5)$ -based models, e.g. [9], then the proton lifetime problem can be solved. In this case gauge bosons  $X$  and  $Y$  do not have diquark couplings and are simply known as leptoquarks. In such a scenario baryon and lepton numbers are also conserved which is consistent with all the experiments conducted so far.

There are also models such as the superstrings-inspired  $E_6$  [10] that are based on a sequence of spontaneously broken groups  $E_6 \rightarrow SO(10) \rightarrow SU(5)$ . These models introduce a

large number of new particles in addition to those present in the standard model: superpartners of the known fermions and gauge bosons, leptoquarks, extended gauge and Higgs bosons and the new “exotic” quarks and leptons. However, most of these particles are introduced to be very heavy and the upper bounds on leptoquarks masses strongly depend on the pattern (*i.e.* Higgs sectors) of gauge symmetry breaking in such models.

## 2.1 LEPTOQUARK MODEL

Direct searches for leptoquarks at collider experiments are usually conducted in the context of effective models. Parameters of these effective models are constrained by established limits from searches for leptoquarks performed at the collider experiments. The most important constraints require that

- leptoquarks interaction terms in the Lagrangian are renormalizable,
- leptoquarks interaction terms respect invariance under the SM gauge group,
- leptoquarks couple to the SM fermions and gauge bosons only,
- leptoquarks conserve lepton number and baryon number separately (to prevent rapid proton decay),
- each leptoquark type couples to one and only one lepton and one quark generations (to satisfy the existing limits on processes mediated by flavor changing neutral currents (FCNC)) and
- each leptoquark has pure chiral couplings to the SM fermions,

where the last requirement in the above list restricts the pion decay into an electron and its neutrino, as this decay is suppressed in the SM w.r.t. the decay to the muon and the muon antineutrino. Leptoquark coupling to two or more generations of fermions would give rise to processes depicted by a Feynman diagram shown in figure 2.2a. Final states resulting from such types of diagrams are highly constrained in the standard model. Therefore leptoquarks are hypothesized to come in three generations as well, with their generation identified with leptons, e.g., a first generation leptoquark couples to a quark and an  $e$  or a quark and a  $\nu_e$ .

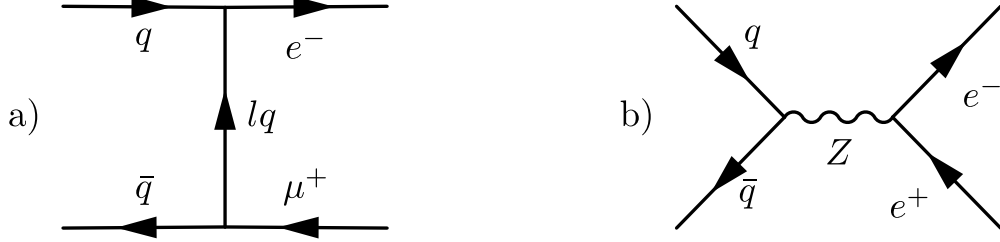


Figure 2.2 Feynman diagrams showing a) FCNC via leptoquark coupling to the first and the second generations of leptons, b) (flavor conserving) neutral current mediated by the  $Z$  boson in the SM whose prediction is consistent with existing experimental data.

A popular model of leptoquarks that incorporates the above constraints is the BRW model (named so after its authors' names: Buchmüller, Rückl and Wyler [11]). This model considers the most general dimensionless,  $SU(3) \times SU(2) \times U(1)$  invariant couplings of scalar and vector leptoquarks to leptons and quarks. But as leptoquarks are colored particles, they also couple to gluons [12]. So the most general interaction is described by the following Lagrangian (density)

$$\mathcal{L} = \mathcal{L}_{|F|=0}^f + \mathcal{L}_{|F|=2}^f + \mathcal{L}^g, \quad (2.1)$$

where the Lagrangian  $\mathcal{L}_{|F|=0,2}^f$  describes Yukawa type interactions of leptoquarks with leptons and quarks ( $lq - l - q$ ), changing the fermion number  $F$  by 0 or 2, respectively, where  $F = 3B + L$ ,  $B$  is the baryon number and  $L$  is the lepton number.  $\mathcal{L}_{|F|=0,2}^f$  conserves the baryon and lepton numbers and has a flavor diagonal form:

$$\begin{aligned} \mathcal{L}_{|F|=0}^f &= (h_{2L}\bar{u}_R\ell_L + h_{2R}\bar{q}_L i\tau_2 e_R)R_2 + \tilde{h}_{2L}\bar{d}_R\ell_L\tilde{R}_2 \\ &+ (h_{1L}\bar{q}_L\gamma^\mu\ell_L + h_{1R}\bar{d}_R\gamma^\mu e_R)U_{1\mu} \\ &+ \tilde{h}_{1R}\bar{u}_R\gamma^\mu e_R\tilde{U}_{1\mu} + h_{3L}\bar{q}_L\vec{\tau}\gamma^\mu\ell_L\vec{U}_{3\mu} + h.c., \end{aligned} \quad (2.2)$$

$$\begin{aligned} \mathcal{L}_{|F|=2}^f &= (g_{1L}\bar{q}_L^c i\tau_2\ell_L + g_{1R}\bar{u}_R^c e_R)S_1 \\ &+ \tilde{g}_{1R}\bar{d}_R^c e_R\tilde{S}_1 + g_{3L}\bar{q}_L^c i\tau_2\vec{\tau}\ell_L\vec{S}_3 \\ &+ (g_{2L}\bar{d}_R^c\gamma^\mu\ell_L + g_{2R}\bar{q}_L^c\gamma^\mu e_R)V_{2\mu} \\ &+ \tilde{g}_{2L}\bar{u}_R^c\gamma^\mu\ell_L\tilde{V}_{2\mu} + h.c., \end{aligned} \quad (2.3)$$

where  $\tau_i$  are the Pauli matrices,  $q_L$  and  $\ell_L$  are the  $SU(2)_L$  quark and lepton doublets, respectively, and  $u_R$ ,  $d_R$ , and  $e_R$  are the corresponding singlet fields; charged conjugated fields

are denoted by  $f^c = C\bar{f}^T$ .  $S_1, \tilde{S}_1, \vec{S}_3, R_2, \tilde{R}_2$ , and  $V_2^\mu, \tilde{V}_2^\mu, U_1^\mu, \tilde{U}_1^\mu, \vec{U}_3$ , denote the scalar (spin=0) and vector (spin=1) leptoquark fields, respectively. Leptoquarks have Yukawa-type couplings to quarks and leptons and are denoted by  $(g_{1(L,R)}, \tilde{g}_{1R}, g_{3L}, h_{2(L,R)}, \tilde{h}_{2L})$  and  $(g_{2(L,R)}, \tilde{g}_{2R}, h_{1(L,R)}, \tilde{h}_{1R}, h_{3L})$  for scalar and vector leptoquarks, respectively, in Eq. (2.2)-(2.3). Table 2.1 shows the quantum numbers associated with the leptoquark fields along with the fermion fields they couple to.

$\mathcal{L}^g$  in 2.1 describes leptoquark-gluon interactions that obey the  $SU(3)_C \times SU(2)_L \times U(1)_Y$  symmetry of the standard model.

$F = 3B + L$	$S$	$SU(3)_C$	$SU(2)_L$	$U(1)_Y$	Coupling	leptoquark
-2	0	$\bar{3}$	1	1/3	$\bar{q}_L^c l_L$	$S_{1L}$
-2	0	$\bar{3}$	1	1/3	$\bar{u}_R^c e_R$	$S_{1R}$
-2	0	$\bar{3}$	1	4/3	$\bar{d}_R^c e_R$	$\tilde{S}_{1R}$
-2	0	$\bar{3}$	3	1/3	$\bar{q}_L^c l_L$	$S_{3L}$
-2	1	$\bar{3}$	2	5/6	$\bar{q}_L^c \gamma^\mu e_R$	$V_{2R}$
-2	1	$\bar{3}$	2	5/6	$\bar{d}_R^c \gamma^\mu l_L$	$V_{2L}$
-2	1	$\bar{3}$	2	-1/6	$\bar{u}_R^c \gamma^\mu l_L$	$\tilde{V}_{2L}$
0	0	3	2	7/6	$\bar{q}_L e_R$	$R_{2R}$
0	0	3	2	7/6	$\bar{u}_R l_L$	$R_{2L}$
0	0	3	2	1/6	$\bar{d}_R l_L$	$\tilde{R}_{2L}$
0	1	3	1	2/3	$\bar{q}_L \gamma^\mu l_L$	$U_{1L}$
0	1	3	1	2/3	$\bar{d}_R \gamma^\mu e_R$	$U_{1R}$
0	1	3	1	5/3	$\bar{u}_R \gamma^\mu e_R$	$\tilde{U}_{1R}$
0	1	3	3	2/3	$\bar{q}_L \gamma^\mu l_L$	$U_{3L}$

Table 2.1 Leptoquarks quantum numbers and couplings according to the BRW model

## 2.2 LEPTOQUARK PRODUCTION AT THE LHC

In proton-proton collisions, leptoquarks can be produced either singly or in pairs. The cross-section for single production, however, depends on the unknown Yukawa coupling  $\lambda_{lq}$  of

the leptoquark and is therefore model-dependent (see Feynman diagrams in Fig. 2.3). Pair production, on the other hand, proceeds through QCD interactions and thus depends only on the leptoquark spin and on the fact that it is a color-triplet field. The lowest-order Feynman diagrams for leptoquark pair-production are shown in the figures 2.5 and 2.4. Unless the Yukawa couplings, which are governed by the electroweak interactions, are rather large (e.g. of the order of the electromagnetic strength), the pair production mechanism would be dominant [13]. The important result is that the pair production of both scalar and vector leptoquarks in hadron collisions is practically independent on the electroweak properties of the leptoquark itself, as opposed to the production in lepton-proton colliders such as HERA.

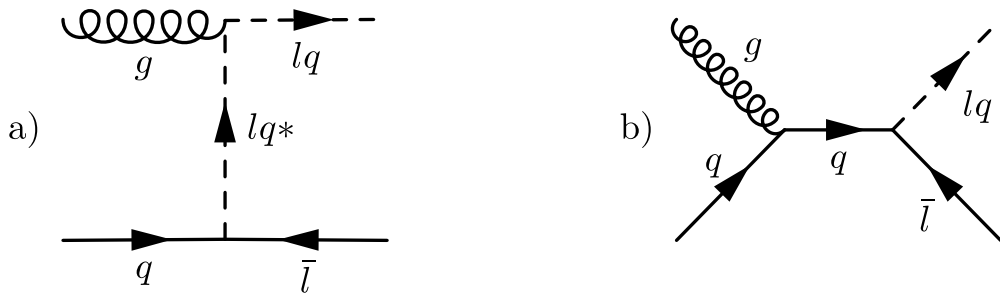


Figure 2.3 Feynman diagram of a single leptoquark production. a) t-channel, b) s-channel

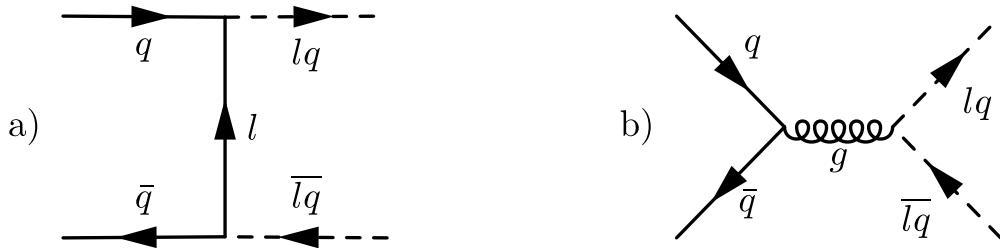


Figure 2.4 Feynman diagram of a pair-production of leptoquarks from a quark anti-quark annihilation. a) t-channel, b) s-channel

Pair production cross-section of leptoquarks up to next-to-leading order has been calculated as a function of the leptoquark mass [14] for the LHC center-of-mass energies using parton distribution function, c.f. 4.1, *CTEQ6* [15]. Fig. 2.6 shows the cross-section for leptoquark pair production.

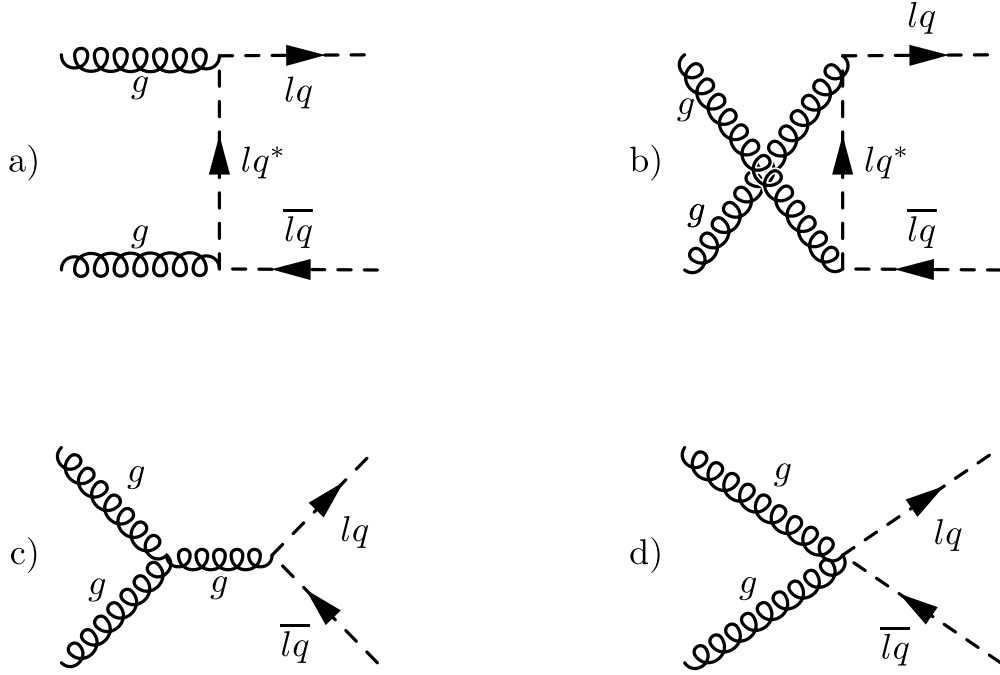


Figure 2.5 Feynman diagrams of pair-productions of leptoquarks from gluon-gluon fusions.

### 2.3 RECENT SEARCHES FOR LEPTOQUARKS

This section describes the recent searches and lower mass limits placed at 95% C.L. on leptoquark masses. A comprehensive summary of the recent results is available elsewhere [16]. As mentioned in section 2.1, leptoquarks come in three generations, and this work focuses on the first generation of leptoquarks that decay into electrons and quarks.  $\beta$  is used to define the branching ratio of the first generation leptoquark decaying into a charged lepton (electron) and a quark. For a leptoquark with  $Q_{em}=-1/3$ , the branching ratio is

$$\beta = \frac{\Gamma(l_{q_1} \rightarrow e^- \bar{u})}{\Gamma(l_{q_1} \rightarrow e^- \bar{u}) + \Gamma(l_{q_1} \rightarrow \nu_e \bar{u})} \quad (2.4)$$

where  $\Gamma$  is the life time of first generation leptoquark ( $l_{q_1}$ ).

Tevatron experiments, currently the best source for leptoquark mass exclusion limits, have searched for the first (decaying to  $eq$ ), the second (decaying to  $\mu q$ ), and the third (decaying to  $\tau q$ ) generation scalar leptoquarks in pair production processes. For  $\beta = 1$ , DØ [17] and CDF [18] collaborations' 95%CL limits for first generation scalar leptoquarks are  $m_{LQ_1} > 256$  GeV and  $m_{LQ_1} > 236$  GeV, respectively. These limits are based on the

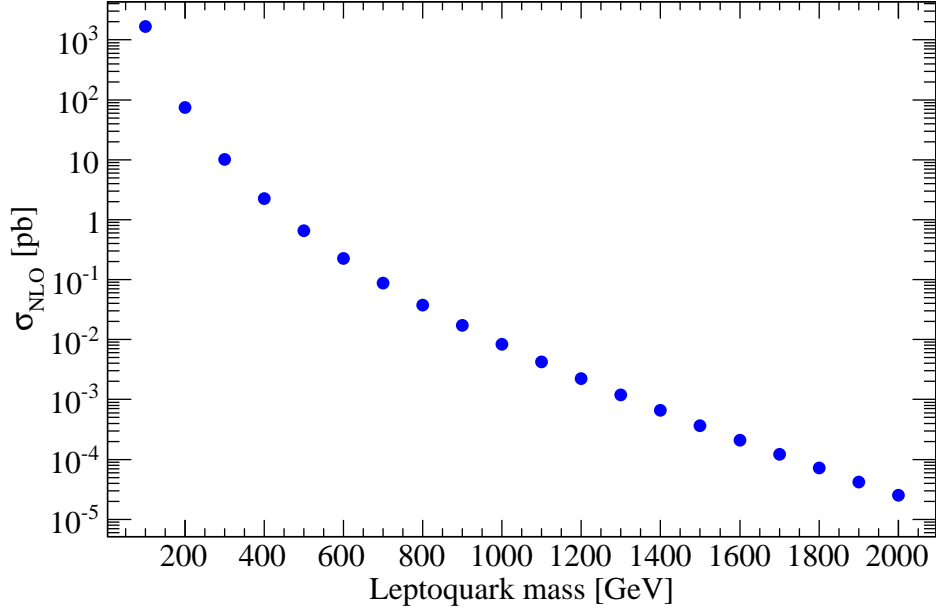


Figure 2.6 Next-to-leading order cross-section for leptoquark pair production as a function of leptoquark mass. The cross-section is calculated for proton-proton collisions at 14 TeV center of mass energy using the parton distribution function set CTEQ6M.

integrated  $p\bar{p}$  luminosities of approximately  $250 \text{ pb}^{-1}$  and  $200 \text{ pb}^{-1}$ . Tevatron results for the second generation leptoquarks,  $m_{LQ_2} > 251 \text{ GeV}$  and  $m_{LQ_2} > 226 \text{ GeV}$ , were obtained with  $300 \text{ pb}^{-1}$  and  $200 \text{ pb}^{-1}$  by the DØ [19] and CDF [20] experiments, respectively.

The leptoquark pair production cross section decreases approximately by a factor of 2 for each additional 20 GeV of leptoquark mass. Therefore, Tevatron exclusion limits are expected to reach 300-350 GeV in the near future.

### 3.0 THE EXPERIMENTAL SETUP

The Large Hadron Collider (LHC) [21, 22] is the next generation particle accelerator being built at CERN, Geneva. Six detectors have been constructed for the LHC. These detectors are located in large underground caverns where the beams collide. Two of the detectors, the ATLAS apparatus and the Compact Muon Solenoid (CMS), are large, general purpose particle detectors. A Large Ion Collider Experiment (ALICE) and LHCb have been built to study the properties of high-density matter at extreme temperatures and bottom mesons, respectively. TOTEM and LHCf detectors have been designed for beam luminosity measurements. The LHC will operate at the center-of-mass energy of 14 TeV. The machine will be running primarily in a proton-proton collision mode designed to provide an instantaneous luminosity of  $10^{34} \text{cm}^{-2} \text{s}^{-1}$ . This would correspond to  $10 \text{fb}^{-1}$  of the integrated  $pp$  luminosity per year. Fig. 3.1 shows the predictions [23] for some important Standard Model cross sections at  $p\bar{p}$  and  $pp$  colliders. This figure also shows the expected numbers of events per second for the respective SM processes at an instantaneous luminosity of  $10^{33} \text{cm}^{-2} \text{s}^{-1}$ .

Probing fundamental forces at a subatomic length scale requires enormous energies. This could be achieved by colliding high-energy beams of protons with each other. At the LHC each proton beam carries 7 TeV of energy. The LHC is described in more detail in section 3.1. Equally important is the role of the detectors used to study the outcome of colliding matter in these accelerators and the LHC hosts the biggest ever apparatuses built for this purpose. Our experimental apparatus is discussed in the section 3.2.

proton - (anti)proton cross sections

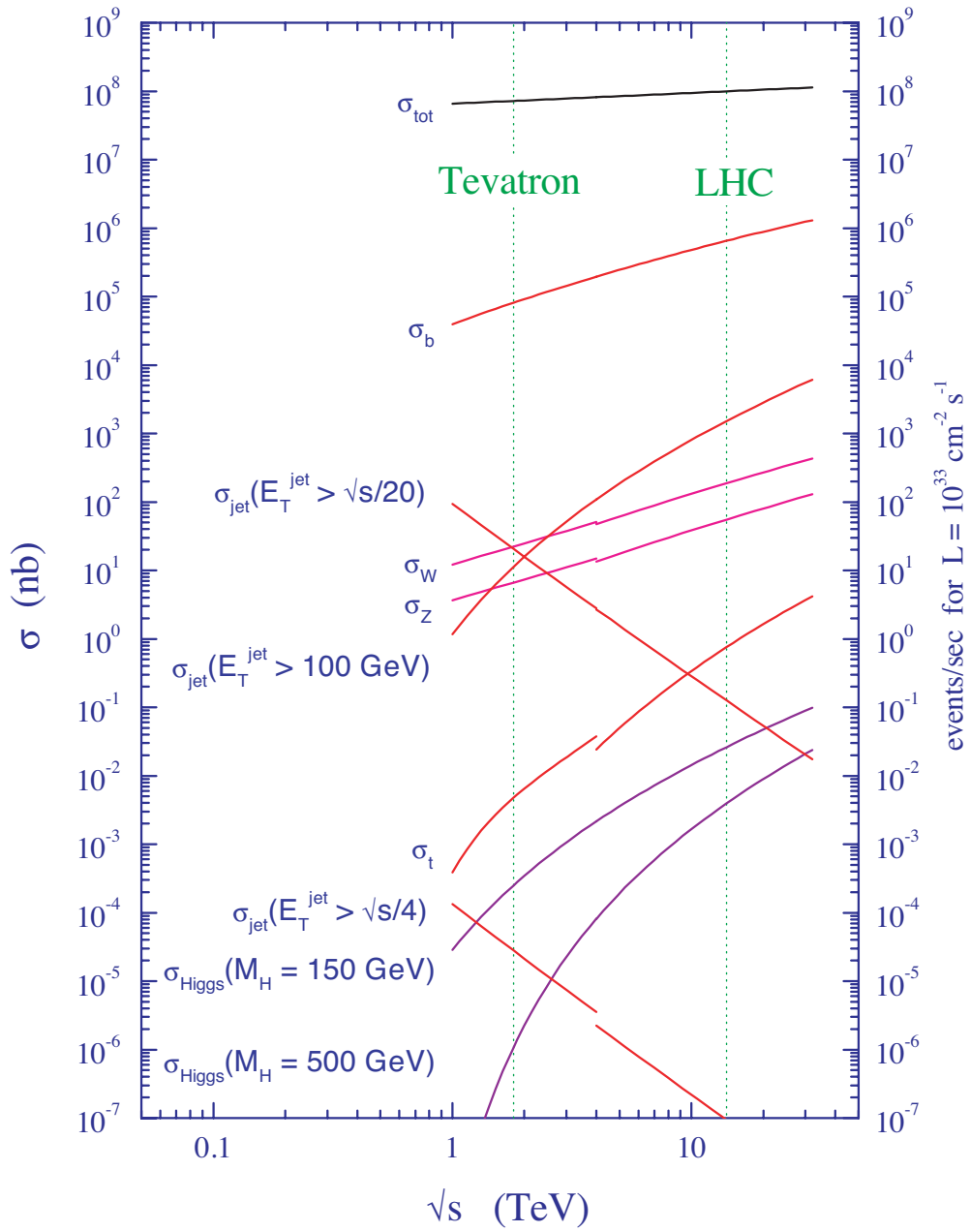


Figure 3.1 Standard Model cross sections at the Large Hadron Collider.

### 3.1 THE ACCELERATOR

The LHC is located at the European Center for Nuclear Research (CERN) in Geneva, Switzerland. It is the world's largest accelerator both in terms of size and the center-of-mass energy. The primary goal of the LHC is to understand the origin of matter in the universe. An overview of the accelerator highlighting its most important features is presented in figure 3.2; for a more detailed description see [21, 22].

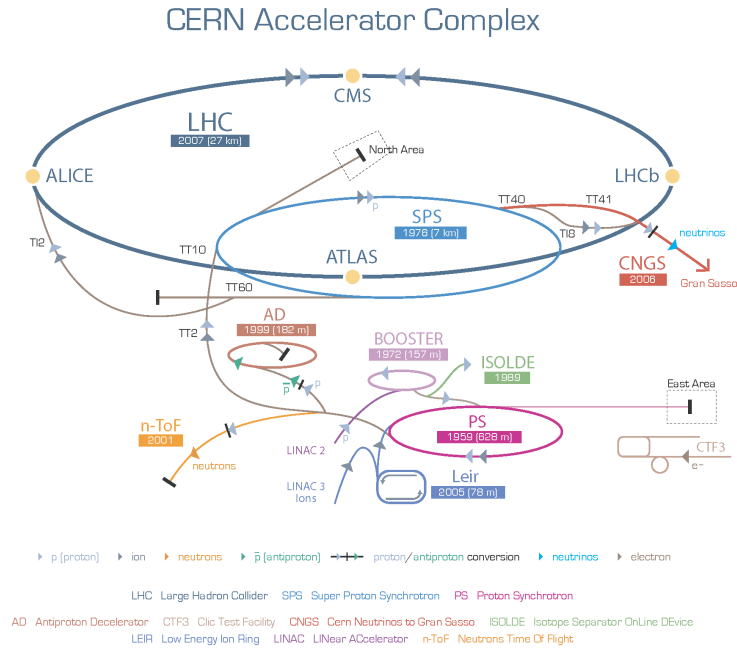


Figure 3.2 Overview of the CERN accelerator complex

The accelerator complex consists of a chain of accelerators which boosts the energy of proton beams in phases. The protons start their accelerating phase in linear accelerators (LINAC). Then they spend intermediate acceleration phases in two synchrotrons, the proton synchrotron (PS) and the super proton synchrotron (SPS), before being finally accelerated in the LHC. The entire accelerating process can be conceptually divided into four steps: proton production, pre-acceleration, acceleration to desired collision energies, and proton storage.

The production source for protons is  $H^+$  ions that are produced in a plasma in a device called the Duoplasmatron. Before being fed into the LINAC for the first acceleration step, the ions are formed into a beam by radio frequency quadrupole magnets. They are then fed

into the PS via the proton synchrotron booster, where protons reach the energy of 1.4 GeV. The PS is the last synchrotron that is responsible for providing the protons bunch spacing in the beam pipe. The beam is then passed to the SPS, where it reaches energies of 450 GeV and is then injected into the LHC. The LHC is the final synchrotron that accelerates protons up to 7 TeV. With a circumference of 27 km, 1232 dipole and 386 quadrupole magnets, the LHC is the world's largest and highest energy particle accelerator. One beam of protons is accelerated in one direction and another beam of protons is accelerated in the opposite direction. Each beam consists of proton bunches separated by 25 ns. Each proton bunch contains about  $10^{11}$  protons. These bunches collide at four interaction points along the LHC ring. ATLAS is located at one of them. The choice of 7 TeV beam energy is determined by the maximum achievable magnetic fields provided by superconducting dipole magnets. The relation between beam momentum and magnetic field is described by

$$p[\text{GeV}/c] = 0.3 \cdot B[\text{T}] \cdot \rho[\text{m}], \quad (3.1)$$

where  $B$  is magnetic field of the dipoles in units of Tesla,  $\rho$  is radius of the LHC ring in units of meters and  $p$  is the proton beam momentum in units of GeV/c. For the LHC radius  $\rho=4.3$  km, and a beam momentum of  $p = 7$  TeV, a magnetic field of  $B = 5.4\text{T}$  is necessary. As a comparison, the terrestrial magnetic field is about 5 orders of magnitude smaller.

Beam luminosity,  $\mathcal{L}$ , is one of the most important parameters that characterizes the performance of a collider. It is completely determined by the properties of the colliding beams, and for the LHC it is expressed as [24]

$$\mathcal{L} = F \frac{\nu n_b N_1 N_2}{4\pi \sigma_x \sigma_y}, \quad (3.2)$$

where  $\nu$  is the revolution frequency of the  $n_b$  bunches,  $F = 0.9$  is a correction factor due to non-zero crossing angle (lower than  $300 \mu\text{rad}$ ) of the two beams at the interaction point,  $N_1$  and  $N_2$  are the numbers of protons in the two colliding bunches, and  $\sigma_x$  and  $\sigma_y$  are the beam profiles in the horizontal (bend) and the vertical directions, respectively, at the interaction point.

The number of events  $N_k$  due to a physical process “ $k$ ” with cross-section  $\sigma_k$  can be written as

$$N_k = \sigma_k \int \mathcal{L}(t) dt, \quad (3.3)$$

where the integration is performed upon the running time of the LHC with instantaneous luminosity  $\mathcal{L}(t)$ . The integral is referred to as the integrated luminosity, and it is measured in *inverse barn* ( $\text{b}^{-1}$ ),  $1 \text{ b} = 10^{-24} \text{ cm}^2$ . The LHC is designed to deliver  $10^{34} \text{ cm}^{-2} \text{ s}^{-1}$  of instantaneous luminosity, thereby allowing  $200 \text{ pb}^{-1}$  of data to be collected in a week’s time (when running at design luminosity). The start-up luminosity of the LHC is expected to be significantly lower. We expect to collect the first  $200 \text{ pb}^{-1}$  of the analysis-quality data within the first year of operation.

### 3.2 THE DETECTOR

The LHC is designed to be a discovery machine where, along with a search for the Higgs boson, physics phenomena outside the scope of the standard model (SM) of particle physics will be investigated. Supersymmetry is one example of such Beyond-the-Standard Model (BSM) physics. To search for the Higgs boson, BSM physics and new particles it is of paramount importance that the detectors can efficiently trigger on, record and reconstruct elementary particles produced in pp collisions.

Hence a detector should have

- a hermetic electromagnetic calorimeter to detect electrons and photons,
- a hermetic hadronic calorimeter to identify jets and missing transverse momentum (presumably) carried away by the neutrinos,
- a muon spectrometer with excellent momentum resolution up to few TeV,
- a device to measure the trajectories of charged particles produced in both primary and secondary decay vertices with a good resolution,
- an ability to identify the species of produced particles,
- a highly-efficient trigger based on electrons, photons, jets, and muons,

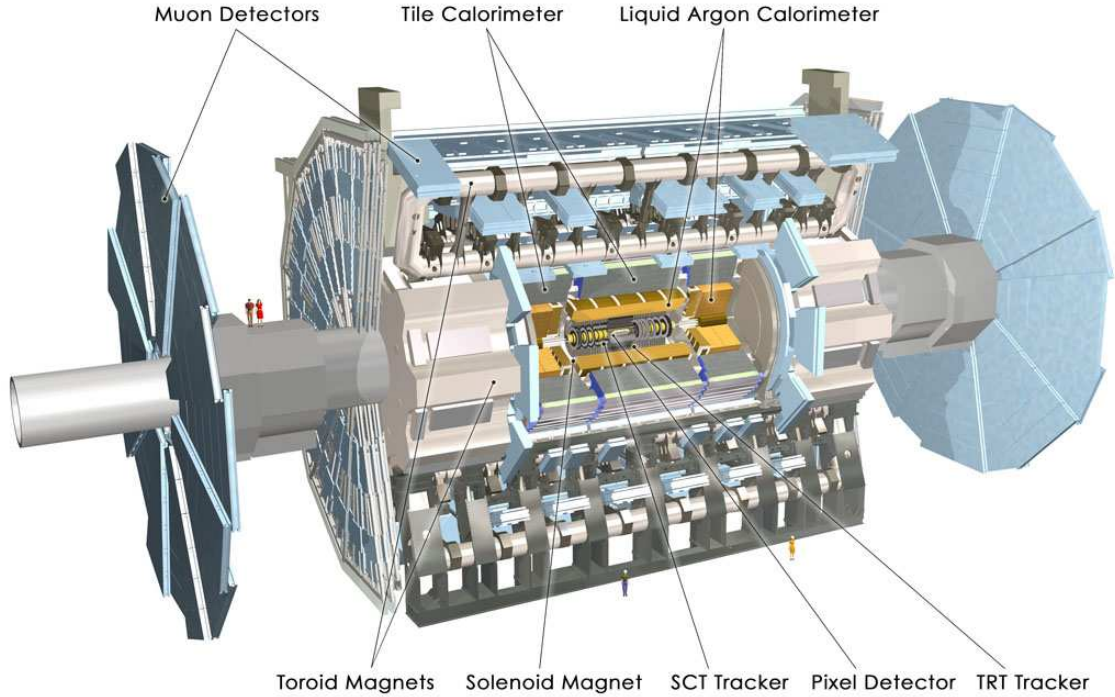


Figure 3.3 Cut-away view of the ATLAS detector illustrating the various sub-detectors

- radiation resistant electronics.

ATLAS [25], **A Toroidal LHC ApparatuS**, shown in figure 3.3 was built to meet such requirements. The ATLAS is 44 meters long, 25 meters high and weighs about 7000 tons. It is built in a cylindrical geometry along the beam pipe (the  $z$ -axis). The  $x$ -axis points towards the center of the LHC storage ring, and the  $y$ -axis points upwards. In polar coordinates, two useful quantities are the azimuthal angle  $\phi$  and the pseudorapidity  $\eta = -\ln \tan \frac{\theta}{2}$ , where  $\theta$  is the polar angle.  $x$ - $y$  plane defines the plane perpendicular to the collision axis.

ATLAS consists of the following major sub-detectors

- **Tracking detectors** for charged particles identification,
- **Calorimeters** for reconstructing energy deposited by electrons, photons and jets,
- **Muon spectrometer** for standalone reconstruction of muons.

### 3.2.1 Tracking

Approximately 1000 particles will emerge from the collision point, with every bunch crossing within the detector region confined by  $|\eta| < 2.5$ , creating a very large track density in the detector. To achieve the momentum and the vertex resolution requirements imposed by the physics goal, high-precision measurements must be made with a fine detector granularity. This requires a tracking sub-detector, known as the Inner Detector (ID), to be constructed using pixel and silicon microstrip trackers (SCT) that are used in conjunction with the straw tubes of the Transition Radiation Tracker (TRT).

The layout of the ID is illustrated in Fig. 3.4. Its basic parameters are summarized in Table 3.1. The ID is immersed in a 2 T magnetic field generated by the central solenoidal magnet which extends over a length of 5.3 m with a diameter of 2.5 m. The precision tracking detectors (pixels and SCT) cover the region  $|\eta| < 2.5$ . In the barrel region, they are arranged on concentric cylinders around the beam axis while in the end-cap regions they are located on disks perpendicular to the beam axis. The highest granularity is achieved around the vertex region using silicon pixel detectors. The pixel layers are segmented in  $R - \phi$  and  $z$  with typically three pixel layers crossed by each track. All pixel sensors are identical and have a minimum pixel size in  $R - \phi \times z$  of  $50 \times 400 \mu\text{m}^2$ . The intrinsic accuracies are  $10 \mu\text{m}$  ( $R - \phi$ ) and  $115 \mu\text{m}$  ( $z$ ), and  $10 \mu\text{m}$  ( $R - \phi$ ) and  $115 \mu\text{m}$  ( $R$ ) in the barrel and the disks, respectively. The pixel detector has approximately 80.4 million readout channels. For the SCT, eight strip layers (four space points) are crossed by each track. In the barrel region, this detector uses small-angle (40 mrad) stereo strips to measure both coordinates, with one set of strips in each layer parallel to the beam direction, measuring  $R - \phi$ . They consist of two 6.4 cm long daisy-chained sensors with a strip pitch of  $80 \mu\text{m}$ . In the end-cap region the detectors have a set of strips running radially and a set of stereo strips at an angle of 40 mrad. The mean pitch of the strips is also approximately  $80 \mu\text{m}$ . The intrinsic accuracy per module in the barrel is  $17 \mu\text{m}$  ( $R - \phi$ ) and  $580 \mu\text{m}$  ( $z$ ) and in the disks is  $17 \mu\text{m}$  ( $R - \phi$ ) and  $580 \mu\text{m}$  ( $R$ ). The total number of readout channels in the SCT is approximately 6.3 million.

A large number of hits (typically, 36 hits per track) is provided by the 4 mm diameter straw tubes of the TRT, which enables track-following up to  $|\eta| = 2.0$ . The TRT only

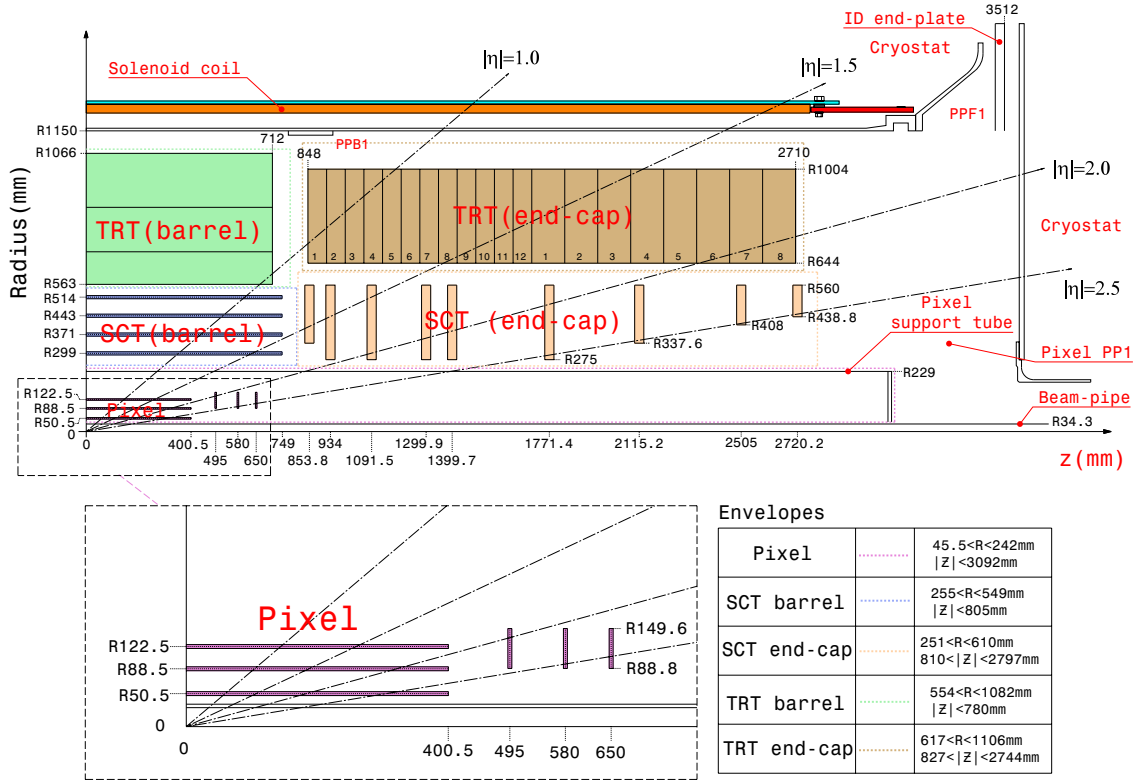


Figure 3.4 Plan view of a quarter of the ATLAS's Inner Detector showing each of the major detector components with its active dimensions and envelopes.

provides  $R - \phi$  information, for which it has an intrinsic accuracy of  $130 \mu\text{m}$  per straw. In the barrel region, the straws are parallel to the beam axis and are 144 cm long, with their wires divided into two halves, approximately at  $\eta = 0$ . In the end-cap region, the 37 cm long straws are arranged radially in wheels. The total number of TRT readout channels is approximately 351,000.

The combination of precision trackers at small radii with the TRT at a larger radius gives a very robust pattern recognition and a high precision in both  $R - \phi$  and  $z$  coordinates. The straw hits at the outer radius contribute significantly to the momentum measurement, since the lower precision per point compared to the silicon is compensated by the large number of measurements and a longer measured track length.

The inner detector system provides tracking measurements in a range matched by the precision measurements of the electromagnetic calorimeter. The electron identification capabilities are enhanced by the detection of transition-radiation photons in the xenon-based

Item		Radial extension (mm)	Length (mm)
<b>Overall ID envelope</b>		$0 < R < 1150$	$0 <  z  < 3512$
<b>Beam-pipe</b>		$29 < R < 36$	
<b>Pixel</b>	Overall envelope	$45.5 < R < 242$	$0 <  z  < 3092$
3 cylindrical layers	Sensitive barrel	$50.5 < R < 122.5$	$0 <  z  < 400.5$
$2 \times 3$ disks	Sensitive end-cap	$88.8 < R < 149.6$	$495 <  z  < 650$
<b>SCT</b>	Overall envelope	$255 < R < 549$ (barrel)	$0 <  z  < 805$
		$251 < R < 610$ (end-cap)	$810 <  z  < 2797$
4 cylindrical layers	Sensitive barrel	$299 < R < 514$	$0 <  z  < 749$
$2 \times 9$ disks	Sensitive end-cap	$275 < R < 560$	$839 <  z  < 2735$
<b>TRT</b>	Overall envelope	$554 < R < 1082$ (barrel)	$0 <  z  < 780$
		$617 < R < 1106$ (end-cap)	$827 <  z  < 2744$
73 straw planes	Sensitive barrel	$563 < R < 1066$	$0 <  z  < 712$
160 straw planes	Sensitive end-cap	$644 < R < 1004$	$848 <  z  < 2710$

Table 3.1 Main parameters of the inner detector system.

gas mixture of the straw tubes. The semiconductor trackers also allow impact parameter measurements and vertexing for heavy-flavor and  $\tau$ -lepton identification. The secondary vertex measurement performance is enhanced by the innermost layer of pixels, at a radius of about 5 cm.

### 3.2.2 Calorimetry

The ATLAS calorimeters shown in figure 3.5 consist of a number of sampling detectors with full  $\phi$ -symmetry and coverage around the beam axis. The calorimeters closest to the beam-line are housed in three cryostats, one barrel and two end-caps. The barrel cryostat contains the electromagnetic barrel calorimeter, whereas each of the two end-cap cryostats contains an electromagnetic end-cap calorimeter (EMEC), a hadronic end-cap calorimeter (HEC), located behind the EMEC, and a forward calorimeter (FCal) to cover the region closest to the beam. All these calorimeters use liquid argon as the active detector medium; liquid argon has been chosen for its intrinsic linear behavior, its stability of response over time and its intrinsic radiation tolerance.

The precision electromagnetic calorimeters are lead-liquid argon detectors with accordion-shape absorbers and electrodes. This geometry allows the calorimeters to have several active layers in depth, three in the precision-measurement region ( $0 < |\eta| < 2.5$ ) and two in the higher- $\eta$  region ( $2.5 < |\eta| < 3.2$ ) and in the overlap region between the barrel and the EMEC. In the precision-measurement region, an accurate position measurement is obtained by finely segmenting the first layer in  $\eta$ . The  $\eta$ -direction of photons is determined by the position of the photon cluster in the first and the second layers. The calorimeter system also has an electromagnetic coverage at higher  $\eta$  ( $3.1 < |\eta| < 4.9$ ) provided by the FCal. Furthermore in the region ( $0 < |\eta| < 1.8$ ) the electromagnetic calorimeters are complemented by presamplers, an instrumented argon layer, which provides a measurement of the energy lost in front of the electromagnetic calorimeters. Table 3.2 summarizes the pseudorapidity coverage, the granularity, and the segmentation in depth of the calorimeters.

The calorimeters must provide a good containment for the electromagnetic and the hadronic showers, and must also limit punch-through into the encompassing muon system.

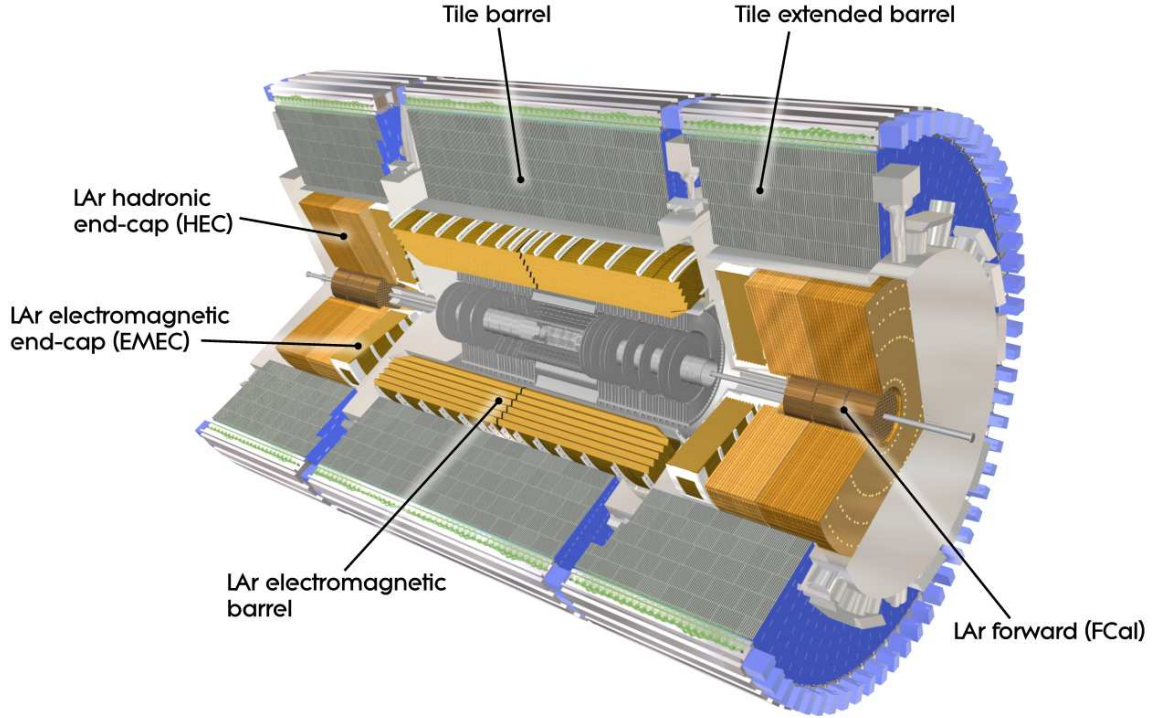


Figure 3.5 Cut-away view of the ATLAS calorimeter system.

The total thickness of the EM calorimeter is  $> 22$  radiation lengths ( $X_0$ ) in the barrel and  $> 24 X_0$  in the end-caps. The approximate 9.7 interaction length ( $\lambda$ ) of the active calorimeter in the barrel ( $10 \lambda$  in the end-caps) is adequate to provide a good resolution for high-energy jets. Together with the large  $\eta$ -coverage, this thickness also ensures a good  $E_T^{miss}$  measurement, which is important for many physics signatures and in particular for SUSY searches.

**3.2.2.1 LAr electromagnetic calorimeter** The EM calorimeter is divided into a barrel part ( $|\eta| < 1.475$ ) and two end-cap components ( $1.375 < |\eta| < 3.2$ ), each housed in their own cryostat. The position of the central solenoid in front of the EM calorimeter demands optimization of the material in order to achieve the desired calorimeter performance. As a consequence, the central solenoid and the LAr calorimeter share a common vacuum vessel, thereby eliminating two vacuum walls. The barrel calorimeter consists of two identical half-barrels, separated by a small gap (4 mm) at  $z = 0$ . Each end-cap calorimeter is mechanically

	Barrel		End-cap	
<b>EM calorimeter</b>				
Number of layers and $ \eta $ coverage				
Presampler	1	$ \eta  < 1.52$	1	$1.5 <  \eta  < 1.8$
Calorimeter	3	$ \eta  < 1.35$	2	$1.375 <  \eta  < 1.5$
	2	$1.35 <  \eta  < 1.475$	3	$1.5 <  \eta  < 2.5$
			2	$2.5 <  \eta  < 3.2$
Granularity $\Delta\eta \times \Delta\phi$ versus $ \eta $				
Presampler	$0.025 \times 0.1$	$ \eta  < 1.52$	$0.025 \times 0.1$	$1.5 <  \eta  < 1.8$
Calorimeter 1st layer	$0.025/8 \times 0.1$	$ \eta  < 1.40$	$0.050 \times 0.1$	$1.375 <  \eta  < 1.425$
	$0.025 \times 0.025$	$1.40 <  \eta  < 1.475$	$0.025 \times 0.1$	$1.425 <  \eta  < 1.5$
			$0.025/8 \times 0.1$	$1.5 <  \eta  < 1.8$
			$0.025/6 \times 0.1$	$1.8 <  \eta  < 2.0$
			$0.025/4 \times 0.1$	$2.0 <  \eta  < 2.4$
			$0.025 \times 0.1$	$2.4 <  \eta  < 2.5$
		$0.1 \times 0.1$	$2.5 <  \eta  < 3.2$	
Calorimeter 2nd layer	$0.025 \times 0.025$	$ \eta  < 1.40$	$0.050 \times 0.025$	$1.375 <  \eta  < 1.425$
	$0.075 \times 0.025$	$1.40 <  \eta  < 1.475$	$0.025 \times 0.025$	$1.425 <  \eta  < 2.5$
			$0.1 \times 0.1$	$2.5 <  \eta  < 3.2$
Calorimeter 3rd layer	$0.050 \times 0.025$	$ \eta  < 1.35$	$0.050 \times 0.025$	$1.5 <  \eta  < 2.5$
Number of readout channels				
Presampler	7808		1536 (both sides)	
Calorimeter	101760		62208 (both sides)	
<b>LAr hadronic end-cap</b>				
$ \eta $ coverage			$1.5 <  \eta  < 3.2$	
Number of layers			4	
Granularity $\Delta\eta \times \Delta\phi$			$0.1 \times 0.1$	$1.5 <  \eta  < 2.5$
			$0.2 \times 0.2$	$2.5 <  \eta  < 3.2$
Readout channels			5632 (both sides)	
<b>LAr forward calorimeter</b>				
$ \eta $ coverage			$3.1 <  \eta  < 4.9$	
Number of layers			3	
Granularity $\Delta x \times \Delta y$ (cm)			FCal1: $3.0 \times 2.6$	$3.15 <  \eta  < 4.30$
			FCal1: $\sim$ four times finer	$3.10 <  \eta  < 3.15,$ $4.30 <  \eta  < 4.83$
			FCal2: $3.3 \times 4.2$	$3.24 <  \eta  < 4.50$
			FCal2: $\sim$ four times finer	$3.20 <  \eta  < 3.24,$ $4.50 <  \eta  < 4.81$
			FCal3: $5.4 \times 4.7$	$3.32 <  \eta  < 4.60$
			FCal3: $\sim$ four times finer	$3.29 <  \eta  < 3.32,$ $4.60 <  \eta  < 4.75$
Readout channels			3524 (both sides)	
<b>Scintillator tile calorimeter</b>				
	Barrel		Extended barrel	
$ \eta $ coverage	$ \eta  < 1.0$		$0.8 <  \eta  < 1.7$	
Number of layers	3		3	
Granularity $\Delta\eta \times \Delta\phi$	$0.1 \times 0.1$		$0.1 \times 0.1$	
	Last layer $0.2 \times 0.1$		$0.2 \times 0.1$	
Readout channels	5760		4092 (both sides)	

Table 3.2 Main parameters of the calorimeter system.

divided into two coaxial wheels: an outer wheel covering the region  $1.375 < |\eta| < 2.5$ , and an inner wheel covering the region  $2.5 < |\eta| < 3.2$ . The EM calorimeter is a lead-LAr detector with accordion-shaped kapton electrodes and lead absorber plates over its full coverage. The accordion geometry provides complete  $\phi$  symmetry without azimuthal cracks. The lead thickness in the absorber plates has been optimized as a function of  $\eta$  in terms of EM calorimeter performance in energy resolution. Over the region devoted to precision physics ( $|\eta| < 2.5$ ), the EM calorimeter is segmented in three sections in depth, see figure 3.6. For the end-cap inner wheel, the calorimeter is segmented in two sections in depth and has a coarser lateral granularity than for the rest of the acceptance.

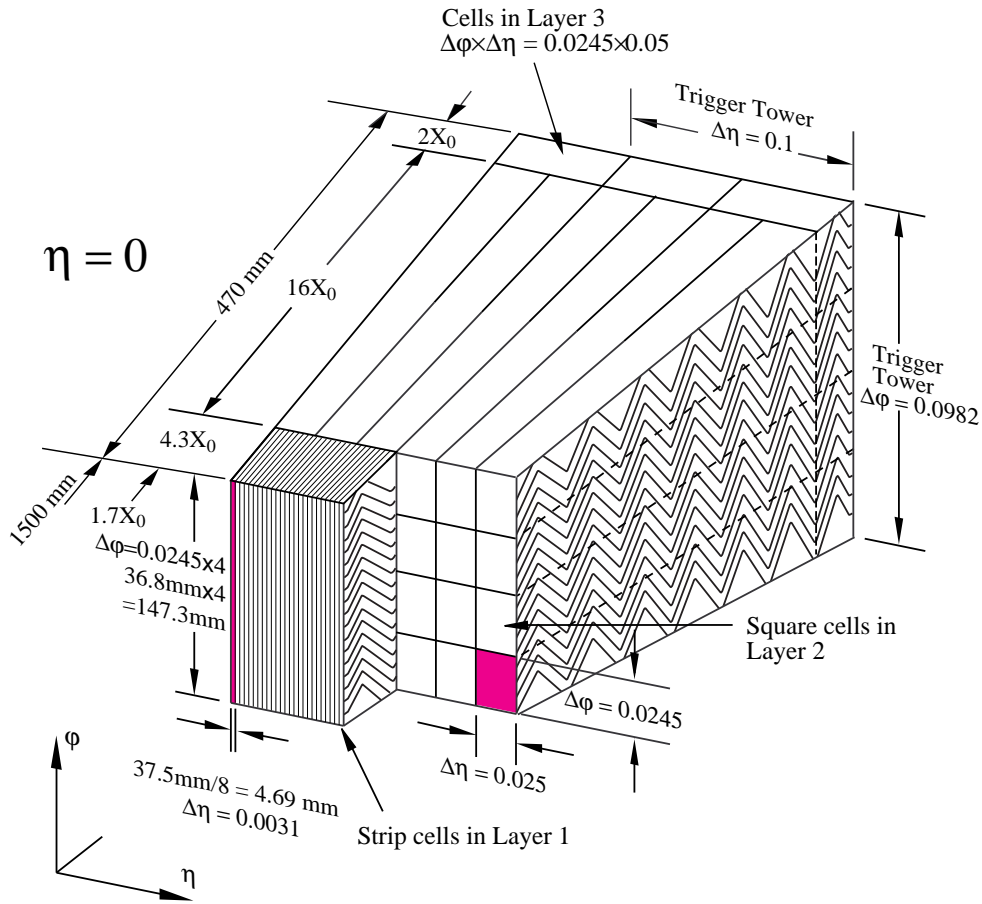


Figure 3.6 Sketch of a barrel module where the different layers are clearly visible with their granularity in  $\eta$  and  $\phi$ .

In the region of  $|\eta| < 1.8$ , a presampler detector is used to correct for the energy lost by electrons and photons upstream of the calorimeter. The presampler consists of an active LAr layer of thickness 1.1 cm (0.5 cm) in the barrel (end-cap) region.

**3.2.2.2 Hadronic calorimeters** The tile calorimeter is placed directly outside the EM calorimeter's envelope. Its barrel covers the region  $|\eta| < 1.0$ , and its two extended barrels the range  $0.8 < |\eta| < 1.7$ . It is a sampling calorimeter which uses steel as the absorber and scintillating tiles as the active material. The barrel and the extended barrels are divided azimuthally into 64 modules. Radially, the tile calorimeter extends from an inner radius of 2.28 m to an outer radius of 4.25 m. It is segmented in depth in three layers of thickness, approximately 1.5, 4.1 and 1.8 interaction lengths ( $\lambda$ ) for the barrel and 1.5, 2.6, and 3.3  $\lambda$  for the extended barrel. The total detector thickness at the outer edge of the tile-instrumented region is 9.7  $\lambda$  at  $\eta = 0$ . Two sides of the scintillating tiles are read out independently by the wavelength-shifting fibers using two photomultiplier tubes. In  $\eta$ , the readout cells built by grouping fibers into the readout photomultipliers are pseudo-projective towards the interaction region.

The Hadronic End-cap Calorimeter (HEC) consists of two independent wheels per end-cap, located directly behind the end-cap electromagnetic calorimeter and sharing the same LAr cryostats. To reduce the drop in material density at the transition between the end-cap and the forward calorimeter (around  $|\eta| = 3.1$ ), the HEC extends out to  $|\eta| = 3.2$ , thereby overlapping with the forward calorimeter. Similarly, the HEC  $\eta$  range also slightly overlaps that of the tile calorimeter ( $|\eta| < 1.7$ ) by extending to  $|\eta| = 1.5$ . Each wheel is built from 32 identical wedge-shaped modules, assembled with fixtures at the periphery and at the central bore. Each wheel is divided into two segments in depth, for a total of four layers per end-cap. The wheels closest to the interaction point are built from 25 mm parallel copper plates, while those further away use 50 mm copper plates (for all wheels the first plate is half-thickness). The outer radius of the copper plates is 2.03 m, while the inner radius is 0.475 m (except in the overlap region with the forward calorimeter where this radius becomes 0.372 m). The copper plates are interleaved with 8.5 mm LAr gaps, providing the active medium for this sampling calorimeter.

The Forward Calorimeter (FCal) is integrated into the end-cap cryostats, as this provides clear benefits in terms of uniformity of the calorimetric coverage as well as reduced radiation background levels in the muon spectrometer. In order to reduce the amount of neutron albedo in the inner detector cavity, the front face of the FCal is recessed by about 1.2 m with

respect to the EM calorimeter front face. This severely limits the depth of the calorimeter to about 10 interaction lengths, and therefore calls for a high-density design. The FCal is approximately 10 interaction lengths deep, and consists of three modules in each end-cap: the first, made of copper, is optimized for electromagnetic measurements, while the other two, made of tungsten, measure predominantly the energy of hadronic interactions. Each module consists of a metal matrix, with regularly spaced longitudinal channels filled with the electrode structure consisting of concentric rods and tubes parallel to the beam axis. The LAr in the gap between the rod and the tube is the sensitive medium. This geometry allows for excellent control of the gaps, which are as small as 0.25 mm in the first section, in order to avoid problems due to ion buildup.

### 3.2.3 Muon spectrometer

The conceptual layout of the muon spectrometer is shown in Fig. 3.7 and the main parameters of the muon chambers are listed in Table 3.3. It is based on the magnetic deflection of muon tracks in the large superconducting air-core toroid magnets, instrumented with separate trigger and high-precision tracking chambers. Over the range  $|\eta| < 1.4$ , magnetic bending is provided by the large barrel toroid. For  $1.6 < |\eta| < 2.7$ , muon tracks are bent by two smaller end-cap magnets inserted into both ends of the barrel toroid. Over  $1.4 < |\eta| < 1.6$ , usually referred to as the transition region, magnetic deflection is provided by a combination of barrel and end-cap fields. This magnet configuration provides a field which is mostly orthogonal to the muon trajectories, while minimizing the degradation of resolution due to multiple scattering. The anticipated high level of particle flux has had a major impact on the choice and design of the spectrometer instrumentation, affecting performance parameters such as rate capability, granularity, aging properties, and radiation hardness.

In the barrel region, tracks are measured in chambers arranged in three cylindrical layers around the beam axis; in the transition and end-cap regions, the chambers are installed in planes perpendicular to the beam, also in three layers.

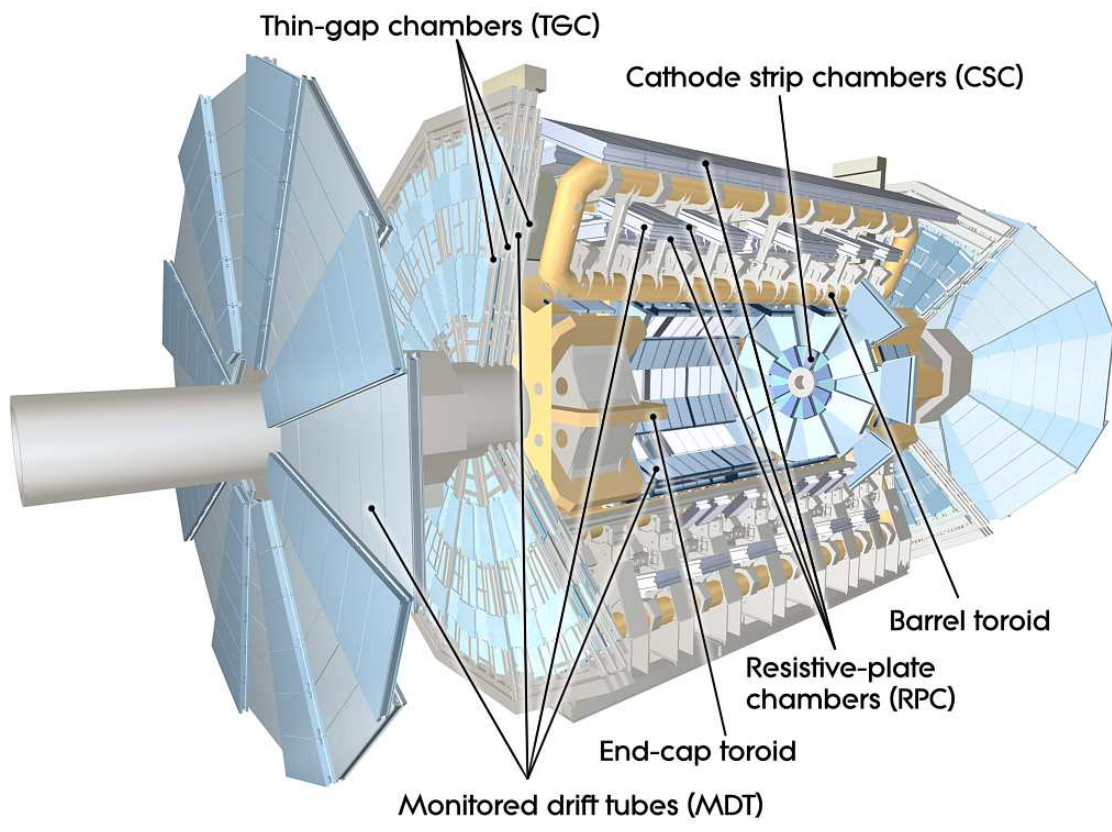


Figure 3.7 Cut-away view of the ATLAS muon system.

<b>Monitored drift tubes</b>	<b>MDT</b>
- Coverage	$ \eta  < 2.7$ (innermost layer: $ \eta  < 2.0$ )
- Number of chambers	1088 (1150)
- Number of channels	339 000 (354 000)
- Function	Precision tracking
<b>Cathode strip chambers</b>	<b>CSC</b>
- Coverage	$2.0 <  \eta  < 2.7$
- Number of chambers	32
- Number of channels	31 000
- Function	Precision tracking
<b>Resistive plate chambers</b>	<b>RPC</b>
- Coverage	$ \eta  < 1.05$
- Number of chambers	544 (606)
- Number of channels	359 000 (373 000)
- Function	Triggering, second coordinate
<b>Thin gap chambers</b>	<b>TGC</b>
- Coverage	$1.05 <  \eta  < 2.7$ (2.4 for triggering)
- Number of chambers	3588
- Number of channels	318 000
- Function	Triggering, second coordinate

Table 3.3 Main parameters of the muon spectrometer. Numbers in brackets for the MDT's and the RPC's refer to the final configuration of the detector in 2009.

**3.2.3.1 The toroid magnets** A system of three large air-core toroids generates the magnetic field for the muon spectrometer. The two end-cap toroids are inserted in the barrel toroid at each end and line up with the central solenoid. Each of the three toroids consists of eight coils assembled radially and symmetrically around the beam axis. The end-cap toroid coil system is rotated by  $22.5^\circ$  with respect to the barrel toroid coil system in order to provide radial overlap and to optimize the bending power at the interface between the two coil systems.

The barrel toroid coils are housed in eight individual cryostats, with the linking elements between them providing the overall mechanical stability. Each end-cap toroid consists of eight racetrack-like coils in an aluminum alloy housing. Each coil has two double-pancake type windings. They are cold-linked and assembled as a single cold mass, housed in one large cryostat. Therefore the internal forces in the end-cap toroids are taken by the cold supporting structure between the coils, a different design solution than in the barrel toroid.

The performance in terms of bending power is characterized by the field integral  $\int B dl$ , where  $B$  is the field component normal to the muon direction and the integral is computed along an infinite-momentum muon trajectory, between the innermost and outermost muon-chamber planes. The barrel toroid provides 1.5 to 5.5 Tm of bending power in the pseudorapidity range  $0 < |\eta| < 1.4$ , and the end-cap toroids approximately 1 to 7.5 Tm in the region  $1.6 < |\eta| < 2.7$ . The bending power is lower in the transition regions where the two magnets overlap ( $1.4 < |\eta| < 1.6$ ).

**3.2.3.2 Muon chamber types** Over most of the  $\eta$ -range, a precision measurement of the track coordinates in the principal bending direction of the magnetic field is provided by Monitored Drift Tubes (MDT's). The mechanical isolation in the drift tubes of each sense wire from its neighbors guarantees a robust and reliable operation. At large pseudorapidities, Cathode Strip Chambers (CSC's, which are multi-wire proportional chambers with cathodes segmented into strips) with higher granularity are used in the innermost plane over  $2 < |\eta| < 2.7$ , to withstand the demanding rate and background conditions. The stringent requirements on the relative alignment of the muon chamber layers are met by the combination of precision mechanical-assembly techniques and optical alignment systems both within and between

muon chambers.

The trigger system covers the pseudorapidity range  $|\eta| < 2.4$ . Resistive Plate Chambers (RPC's) are used in the barrel and Thin Gap Chambers (TGC's) in the end-cap regions. The trigger chambers for the muon spectrometer serve a threefold purpose: provide bunch-crossing identification, provide well-defined  $p_T$  thresholds, and measure the muon coordinate in the direction orthogonal to that determined by the precision-tracking chambers.

**3.2.3.3 Muon chamber alignment and B-field reconstruction** The overall performance over the large areas involved, particularly at the highest momenta, depends on the alignment of the muon chambers with respect to each other and with respect to the overall detector.

The accuracy of the stand-alone muon momentum measurement necessitates a precision of 30  $\mu\text{m}$  on the relative alignment of the chambers both within each projective tower and between consecutive layers in immediately adjacent towers. The internal deformations and relative positions of the MDT chambers are monitored by approximately 12000 precision-mounted alignment sensors, all based on the optical monitoring of deviations from straight lines. Because of geometrical constraints, the muon reconstruction algorithms and monitoring of the chamber positions rely on somewhat different strategies and sensor types in the end-cap and the barrel regions.

The accuracy required for the relative positioning of non-adjacent towers to obtain adequate mass resolution for multi-muon final states lies in the few millimeter range. This initial positioning accuracy was established approximately during the installation of the chambers. Ultimately, the relative alignment of the barrel and the forward regions of the muon spectrometer, of the calorimeters and of the inner detector will rely on high-momentum muon trajectories.

For magnetic field reconstruction, the goal is to determine the bending power along the muon trajectory to a few parts in a thousand. The field is continuously monitored by a total of approximately 1800 Hall sensors distributed throughout the spectrometer volume. Their readings are compared with magnetic-field simulations and used for reconstructing the position of the toroid coils in space, as well as to account for magnetic perturbations induced

by the tile calorimeter and other nearby metallic structures.

### 3.2.4 Trigger, readout, data acquisition, and control systems

The Trigger and Data Acquisition (collectively TDAQ) systems, the timing- and trigger-control logic, and the Detector Control System (DCS) are partitioned into sub-systems, typically associated with sub-detectors, which have the same logical components and building blocks.

It is not possible to process and select events within the 25 ns available between successive bunch crossings. Furthermore, the size of the detectors and the underground caverns imposes a minimum transit time between the detector electronics and trigger electronics, and the first level trigger calculations themselves need to be sophisticated enough to identify clear signatures of new physics among an overwhelming rate of less interesting events, reducing the rate by a factor of about 500. During the transit and processing time, around  $2.5 \mu\text{s}$ , the detector data must be time stamped and held in the buffers of the radiation-hard front-end circuits.

The trigger system has three distinct levels: L1, L2, and the event filter. Each trigger level refines the decisions made at the previous level and, where necessary, applies additional selection criteria. The data acquisition system receives and buffers the event data from the detector-specific readout electronics, at the L1 trigger accept rate of over 1600 point-to-point readout links. The first level uses a limited amount of the total detector information to make a decision in less than  $2.5 \mu\text{s}$ , reducing the rate to about 75 kHz. The two higher levels access more detector information for a final rate of up to 200 Hz with an event size of approximately 1.3 Mbyte.

**3.2.4.1 Trigger system** The L1 trigger searches for high transverse-momentum muons, electrons, photons, jets, and  $\tau$ -leptons decaying into hadrons, as well as the large missing total transverse energy. Its selection is based on information from a subset of detectors. High transverse-momentum muons are identified using trigger chambers in the barrel and end-cap regions of the spectrometer. Calorimeter selections are based on reduced-granularity

information from all the calorimeters. Results from the L1 muon and calorimeter triggers are processed by the central trigger processor, which implements a trigger ‘menu’ made up of combinations of trigger selections. Pre-scaling of the trigger menu items is also available, allowing optimal use of the bandwidth as luminosity and background conditions change. Events passing the L1 trigger selection are transferred to the next stages of the detector-specific electronics and subsequently to the data acquisition via point-to-point links.

In each event, the L1 trigger also defines one or more Regions-of-Interest (RoI’s), i.e. the geographical coordinates in  $\eta$  and  $\phi$ , of those regions within the detector where its selection process has identified interesting features. The RoI data include information on the type of the feature identified and the criteria passed, e.g. a threshold. This information is subsequently used by the high-level trigger.

The L2 selection is seeded by the RoI information provided by the L1 trigger over a dedicated data path. The L2 selections use, at full granularity and precision, all the available detector data within the RoI’s (approximately 2% of the total event data). The L2 menus are designed to reduce the trigger rate to approximately 3.5 kHz, with an event processing time of about 40 ms, averaged over all events. The final stage of the event selection is carried out by the event filter, which reduces the event rate to roughly 200 Hz. Its selections are implemented using offline analysis procedures within an average event processing time of the order of four seconds.

**3.2.4.2 Readout architecture and data acquisition** The Readout Drivers (ROD’s) are detector-specific functional elements of the front-end systems, which achieve a higher level of data concentration and multiplexing by gathering information from several front-end data streams. Although each sub-detector uses specific front-end electronics and ROD’s, these components are built from standardized blocks and are subject to common requirements. The front-end electronics sub-system includes different functional components:

- the front-end analogue or analogue-to-digital processing;
- the L1 buffer in which the (analogue or digital) information is retained for a time long enough to accommodate the L1 trigger latency;
- the derandomizing buffer in which the data corresponding to a L1 trigger accept are

stored before being sent to the following level. This element is necessary to accommodate the maximum instantaneous L1 rate without introducing significant deadtime (maximum 1%);

- the dedicated links or buses which are used to transmit the front-end data stream to the next stage.

After an event is accepted by the L1 trigger, the data from the pipe-lines are transferred off the detector to the ROD's. Digitized signals are formatted as raw data prior to being transferred to the DAQ system. The ROD's follow some general ATLAS rules, including the definition of the data format of the event, the error detection/recovery mechanisms to be implemented, and the physical interface for the data transmission to the DAQ system.

The first stage of the DAQ, the readout system, receives and temporarily stores the data in local buffers. It is subsequently solicited by the L2 trigger for the event data associated to RoI's. Those events selected by the L2 trigger are then transferred to the event-building system and subsequently to the event filter for final selection. Events selected by the event filter are moved to permanent storage at the CERN computer centre. In addition to the movement of data, the data acquisition also provides for the configuration, control and monitoring of the hardware and software components which together provide the data-taking functionality.

The DCS permits the coherent and safe operation of the ATLAS detector hardware, and serves as a homogeneous interface to all sub-detectors and to the technical infrastructure of the experiment. It controls, continuously monitors and archives the operational parameters, signals any abnormal behavior to the operator, and allows automatic or manual corrective actions to be taken. Typical examples are high- and low-voltage systems for detector and electronics, gas and cooling systems, magnetic field, temperatures, and humidity. The DCS also enables bi-directional communication with the data acquisition system in order to synchronize the state of the detector with data-taking. It also handles the communication between the sub-detectors and other systems which are controlled independently, such as the LHC accelerator, the CERN technical services, the ATLAS magnets, and the detector safety system.

## 4.0 PHYSICS SIMULATION AND EVENT RECONSTRUCTION

This chapter briefly describes MC-based simulation of physical processes and reconstruction of the final state particles resulting from these processes. Fig. 4.1 demonstrates the complexity of the outcome of proton-proton collisions at the LHC that has to be simulated using Monte Carlo techniques.

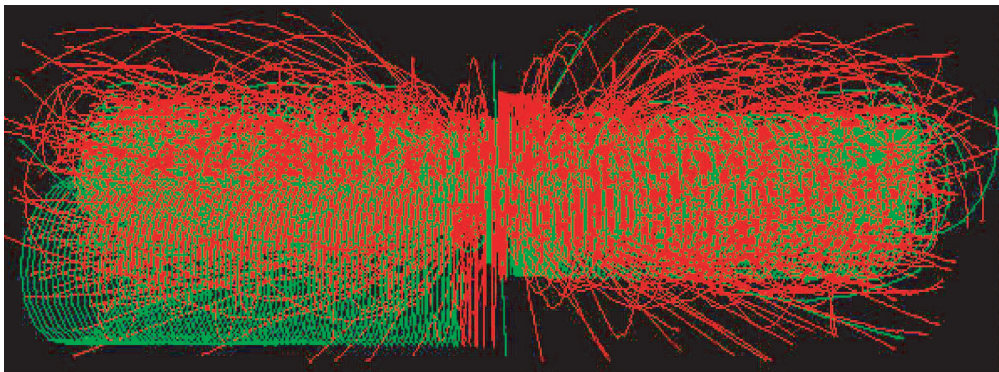


Figure 4.1 Monte Carlo simulation of a typical event in proton-proton collisions.

Equally challenging is the reconstruction (as described in Section 4.3) of these processes and particle identification.

### 4.1 HARD SCATTERING PROCESSES AT THE LHC

This section briefly discusses the theoretical techniques that are used to make predictions of the outcome of hadron-hadron collisions such as that at the LHC. The momentum transfer<sup>1</sup>  $Q^2$ , that takes place between the hard scattering partons in high energy proton-proton

---

<sup>1</sup>“Momentum transfer” is the term used for the Lorentz-invariant quantity, the square of the transferred four-momentum.

collisions, can be used to classify an interaction as either a hard or a soft process. The event properties and rates of the primary hard scattering processes (e.g.  $Z$  boson production) involving the constituent partons (*i.e.* quarks and gluons) of the colliding protons can be accurately predicted using perturbative QCD. However, the properties of the partons inside the colliding protons cannot be described using perturbation theory because of  $\alpha_s \sim 1$ , therefore such calculations are performed by utilizing the Factorization Theorem [26] and by parameterizing the internal structure of the proton using parton distribution functions (PDFs). Calculations of hard scattering processes are very difficult due to the nature of the strong force, therefore such calculations are usually performed to leading order, and then the corrections are evaluated using parton showering [27] techniques and MC simulation. The hard scattering processes are followed by low  $Q^2$  (*i.e.* soft) processes because of the nature of the strong force. Such soft processes occur when colored quarks and gluons, originating both from the hard scatter and the remnants of the dissociated protons, form colorless final state hadrons – a process known as hadronization. Perturbative treatment of QCD processes at low  $Q^2$  gives unstable solutions, therefore predictions for these soft processes must be obtained using different, often less accurate, theoretical methods. An overview of the various steps that must be made to fully describe the physics processes that occur in proton-proton collisions is shown schematically in Fig. 4.2. In this figure the areas where soft interactions are dominant, both within the colliding protons and during the hadronization process, are shaded in grey.

A detailed description of the theoretical models of soft physics can be found elsewhere [28].

#### 4.1.1 Factorization Theorem, Parton Showering and Hadronization

In order to use the MC method to simulate hard processes in proton-proton collisions correctly, the substructure of the proton needs to be accounted for. The factorization theorem is used to decouple hard scattering between partons and their evolution into final state particles in hadron-hadron interactions. For relatively simple processes, such as the production of single  $Z$ , vector boson pairs and other similar reactions, where no jets are produced directly

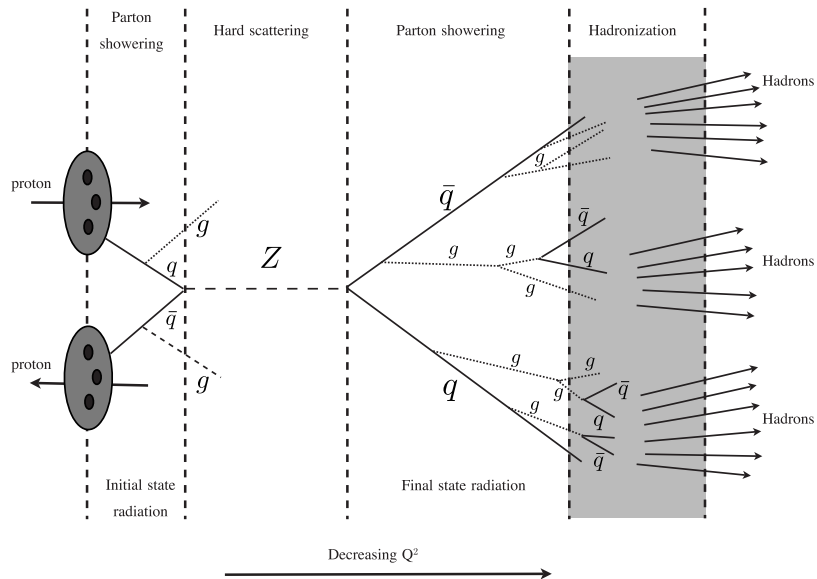


Figure 4.2 A schematic diagram of a hard scattering process in a proton-proton collision. It shows the leading order production of a  $Z$  boson subsequently decaying into hadrons born from a quark anti-quark pair ( $q\bar{q}$ ). Both perturbative and non-perturbative parts of the production and the decay process are represented including the decay of the resulting  $q\bar{q}$  pair into the color-neutral final state particles during hadronization. The areas where the soft interaction is dominant, both within the colliding protons and during hadronization, are shaded in grey.

in hard scattering, this theorem is elegantly described by the following equation

$$\sigma_{AB \rightarrow X} = \int dx_a dx_b f_{a/A}(x_a, Q^2) f_{b/B}(x_b, Q^2) \hat{\sigma}_{ab \rightarrow X}, \quad (4.1)$$

where  $a$  and  $b$  are the two partons interacting in the hard scattering process,  $f_{a/A}$  and  $f_{b/B}$  are the parton distribution functions (PDFs) that parameterize the properties of the partons within the colliding hadrons ( $A$  or  $B$ ) and are functions of  $x$ , the fraction of the hadron's longitudinal momentum, and  $Q^2$  is the square of the momentum transferred during hard scattering. The cross section  $\hat{\sigma}_{ab \rightarrow X}$  is the parton-level cross-section for  $a$  and  $b$  to produce  $X$ . This cross section can be calculated using perturbation theory. For more complex processes, where jets are produced directly in hard scattering,  $\hat{\sigma}_{ab \rightarrow X}$  includes the effects of parton showering, which are implemented in a model-dependent way in MC simulation.

Unfortunately, even these parton-level calculations for the cross-section cannot be computed to all orders in perturbation theory. The standard procedure for dealing with the higher orders that are not included in a given perturbative calculation is to add the initial

and the final state parton showers – parton showering – to the discussed process (see the first and the third column in Fig. 4.2). This works in the following way: since the partons carry electromagnetic and/or color charge, the higher order contributions that are missing will take the form of emissions of gluons and photons. These missing terms can be approximated by adding additional radiative processes, whereby a parton is allowed to branch into a parton with lower energy plus, for example, an emitted gluon, i.e.  $q \rightarrow qg$ . This branching is usually modeled using the Altarelli-Parisi splitting function [27]. The showering continues until the branching quarks and gluons reach some predefined energy which is above the confinement regime.

There is no evidence that color-charged objects exist in nature, hence the final state radiation, as shown in third column of Fig. 4.2 describes an unphysical state. In addition, there are interactions from the other partons (that did not participate in the hard scattering) which give rise to color-charged partons. Hadronization is the final step of simulation where conservation of color and color-neutrality of the final state particles is achieved. As hadronization involves soft processes, it cannot be described analytically using perturbation theory, instead, it is modeled using phenomenology as a guide.

The two most common Monte Carlo simulation packages for generating events from hadron-hadron collisions are PYTHIA [29] and HERWIG [30].

## 4.2 DETECTOR SIMULATION

Events we detect and measure the properties of at the LHC consist of the final state particles born in processes such as, *e.g.*, the  $Z$  boson production. These events could only be reconstructed using particle detectors as described in Section 3.2. Detectors are often very complex devices that can be described, conceptually, as the matrix of measuring devices' responses to subatomic particles that traverse them. This section describes the detector response while simulation methods are described in the preceding section.

Detector response can be studied either using the actual data or using MC simulation of the detector with a dedicated software package called GEANT4 [31].

Fig. 4.3 shows a simplified schematic of the detector response to a typical event with many final state particles. As particles traverse the detectors, they lose energy primarily by

- radiation such as Bremsstrahlung, Cerenkov light, and transition radiation,
- ionization, and
- multiple scattering.

The resulting energy losses are described by two parameters, radiation length  $X_0$  and interaction length  $\lambda$ . A more detailed description of energy losses can be found elsewhere [32].

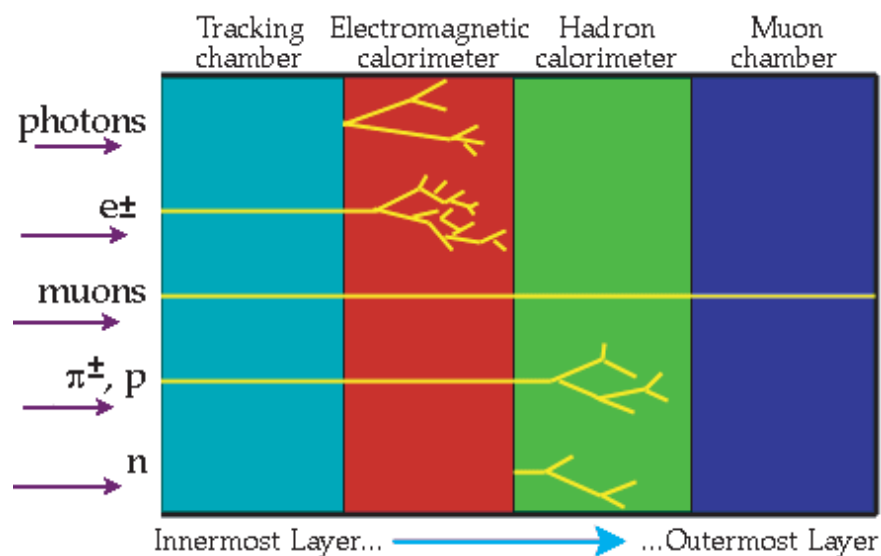


Figure 4.3 A sketch of the detector response to the final state particles. Lines in yellow indicate the region where particles primarily interact in the detector, e.g. electrons shown in the second row interact in the tracking chamber and the electromagnetic calorimeter with most of the activity being in the latter.

In order to correctly simulate the detector response, it is crucial to understand the properties of the detectors. Figures 4.4 and 4.5 show the amount of material in units of radiation length  $X_0$  and interaction length  $\lambda$  in the inner detector 3.2.1 and the calorimeter 3.2.2 of the ATLAS, respectively. All this information about the amounts of passive and active materials has to be accounted for in the detector simulation.

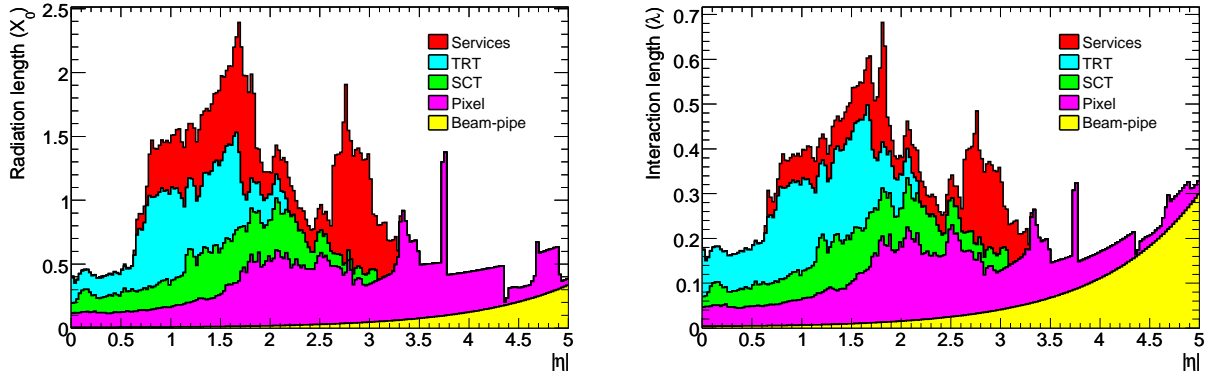


Figure 4.4 Material distribution ( $X_0$ ,  $\lambda$ ) at the exit of the inner detector of ATLAS. The distribution is shown as a function of  $|\eta|$  and averaged over  $\phi$ . The breakdown indicates the contributions of external services and of individual sub-detectors, including passive material that describes the detector infrastructure also found inside the active volumes.

### 4.3 EVENT RECONSTRUCTION

Detector response is digitized as the pattern of energy deposits in detector sub-systems. This information can be used to reconstruct the final state particles. The reconstruction is unfolding the detector response by taking an inverse of the detector matrix. This step is performed for simulated and actual detector responses, the latter being the reconstruction of recorded raw binary data from proton-proton collisions at the LHC.

Event reconstruction requires applying various particle identification algorithms to raw (digitized) data. In what follows the event reconstruction is described in the context of ATLAS, however the treatment is fairly generic, as would be applied to any general-purpose apparatus at a particle collider.

#### 4.3.1 ATLAS Software Infrastructure

This section briefly discusses the software environment of ATLAS. Besides event generation, all other steps such as detector simulation, reconstruction of simulated or recorded data and the analysis of data are performed within the **Athena** framework [33].

**Athena** is a modular object-oriented framework written primarily in the programming language **C++**. It utilizes a convenient scripting interface written in **python** used to configure the user-defined software environment during run-time. The entire software takes about

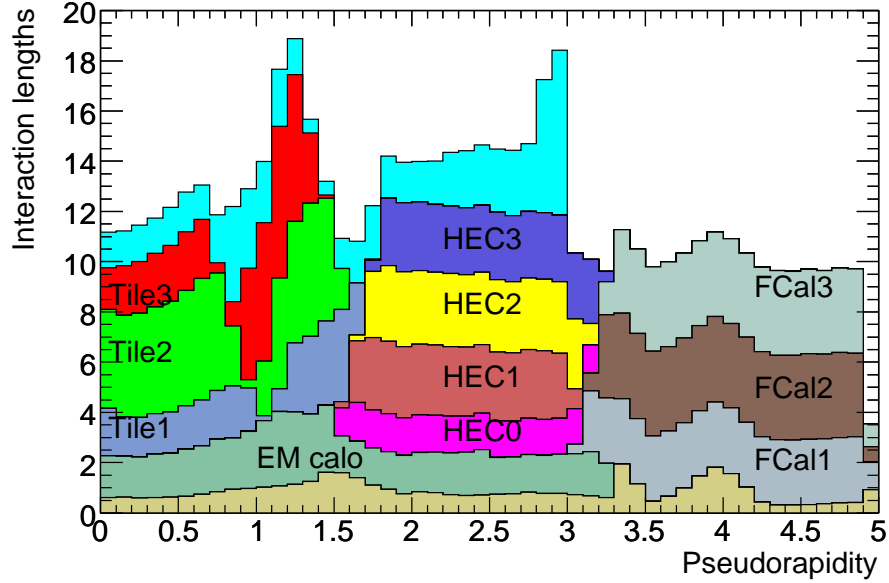


Figure 4.5 Cumulative amount of material, in units of interaction length, as a function of  $|\eta|$ , in front of the electromagnetic calorimeters, in the electromagnetic calorimeters themselves, in each hadronic layer, and the total amount at the end of the active calorimetry of ATLAS. Also shown for completeness is the total amount of material in front of the first active layer of the muon spectrometer (up to  $|\eta| < 3.0$ )

15 gigabytes of disk space. In the data-taking phase, **Athena** accepts data in the Raw Data Object (RDO) format which is used in ATLAS hardware and firmware as input for the reconstruction algorithms. This step produces event summary data (ESD) that typically takes 750 kilobytes per event. ESD files are further condensed into Analysis Object Data (AOD) and derived physics data (DPD) to make them smaller in size (170 kilobytes per event) and are optimized for particular physics analyses. A user can run her **Athena**-based code on reconstructed AODs to further reconstruct objects of interest from final state candidates, e.g., each AOD event typically contains many energy clusters which are supposed to be analyzed by the user to identify electron candidates best suited for her analysis, e.g., such as a search for leptoquarks decaying into electrons and particle-jets.

It must also be mentioned that to facilitate timely access to the LHC data, a worldwide LHC computing grid has been developed.

### 4.3.2 Reconstruction of Electrons and Photons

Electrons and photons develop electromagnetic showers in the calorimeters and thereby lose their energy and eventually get absorbed. They are hence reconstructed from clusters of energy deposited in the electromagnetic calorimeters. For instance, the energy in the barrel electromagnetic calorimeter for electrons is collected over an area corresponding to  $3 \times 7$  cells in the middle sampling layer, equivalent to  $\Delta\eta \times \Delta\phi = 0.075 \times 0.175$ . Furthermore, in the case of electrons, a proximity match in  $\eta - \phi$  space is also required with a track reconstructed in the inner detector. At the next step in reconstruction the calibration constants are applied to the electromagnetic clusters. At this stage the raw binary signal from each calorimeter cell is converted to the amount of deposited energy. Energies from the various cells from all the sampling layers of clusters are then summed together, and an energy-weighted cluster position in  $\eta - \phi$  is calculated for each layer. Finally, the electron and the photon candidates are identified by applying selection criteria to various quantities measured for the reconstructed clusters. Further details of the electron identification algorithms used on ATLAS can be found in Appendix [A.1](#).

### 4.3.3 Muon Reconstruction

Being electrically charged particles, muons leave energy deposits in the inner detector, the calorimeters, and in the muon spectrometer. Muon tracks are reconstructed using “hits” (*i.e.* digitized detector responses) left in the muon chambers. The reconstructed trajectories are then extrapolated back to the (presumed) primary vertex in the interaction region on the beam line. Independent information about the muon tracks is also available from the inner detector. Whenever possible, the two sets of measurements are combined to give the best reconstruction of the muon candidates’ momenta.

The tracking system of ATLAS, the Inner Detector, is designed to reconstruct the trajectories of charged particles with a hermetic coverage up to  $|\eta| < 2.5$ . The 2 Tesla solenoidal magnet installed just outside the inner detector allows the provision of an independent measurement of the momentum of muons for transverse momentum ( $p_T$ ) range between 30 GeV and 200 GeV. The inner detector and the muon spectrometer momentum measurements are

combined to give a precise measurement which is better than that from either sub-detector alone. To reconstruct muons of momenta below 30 GeV (above 200 GeV) the information is primarily obtained from the inner detector (the muon spectrometer).

#### 4.3.4 Particle Jet Reconstruction

Hadronization of quarks and gluons produces streams of hadrons, commonly referred to as hadronic jets, that are detected in the LAr and the Tile calorimeters. Atlas calorimeters contain about 270,000 cells and, when traversing the calorimeters, jets lose their energy over multiple cells. To meaningfully reconstruct a particle jet, it becomes necessary to combine calorimeter cells into larger objects. The two most commonly employed approaches are to combine calorimeter cells into calorimeter towers or topological clusters.

Calorimeter towers are built by collecting cells into bins of  $\Delta\eta \times \Delta\phi = 0.1 \times 0.1$  within the entire acceptance region of the calorimeters ( $|\eta| < 5.0$ ). Calorimeter cells that project completely inside the tower contribute their total energy to the tower signal, while non-projective cells and projective cells larger than the tower size contribute only a fraction of their signal to the tower, where this fraction is estimated using the fraction of the cell area within the towers. Such calorimeter towers form the seeds for the jet finding algorithms.

Topological clustering starts with a seed cell that has a signal-to-noise ratio, a.k.a. signal significance, above certain threshold, i.e.,  $E_{cell} < 4 \sigma_{noise,cell}$  followed by iteratively adding neighboring cells to the cluster, as long as the signal in the cell is significant as compared to the noise.

Reconstructed towers and clusters are used as input objects to the standard jet finding algorithms such as, *e.g.*, cone-jet algorithm and  $K_T$  algorithm [34]. These algorithms are designed to avoid infrared and collinear singularities arising due to overlapping jets or collinear jets, respectively. Cone-jet algorithm requires its objects to be above a certain  $p_T$  threshold and combines objects in a cone of a fixed radius defined in the space of  $\eta - \phi$ . The details of the jet reconstruction algorithms are discussed elsewhere [35]. Fig. 4.6 shows reconstructed objects from a Monte Carlo simulation of one event for leptoquark pair production. This figure was prepared using the ATLAS event display software package **ATLANTIS** [36].

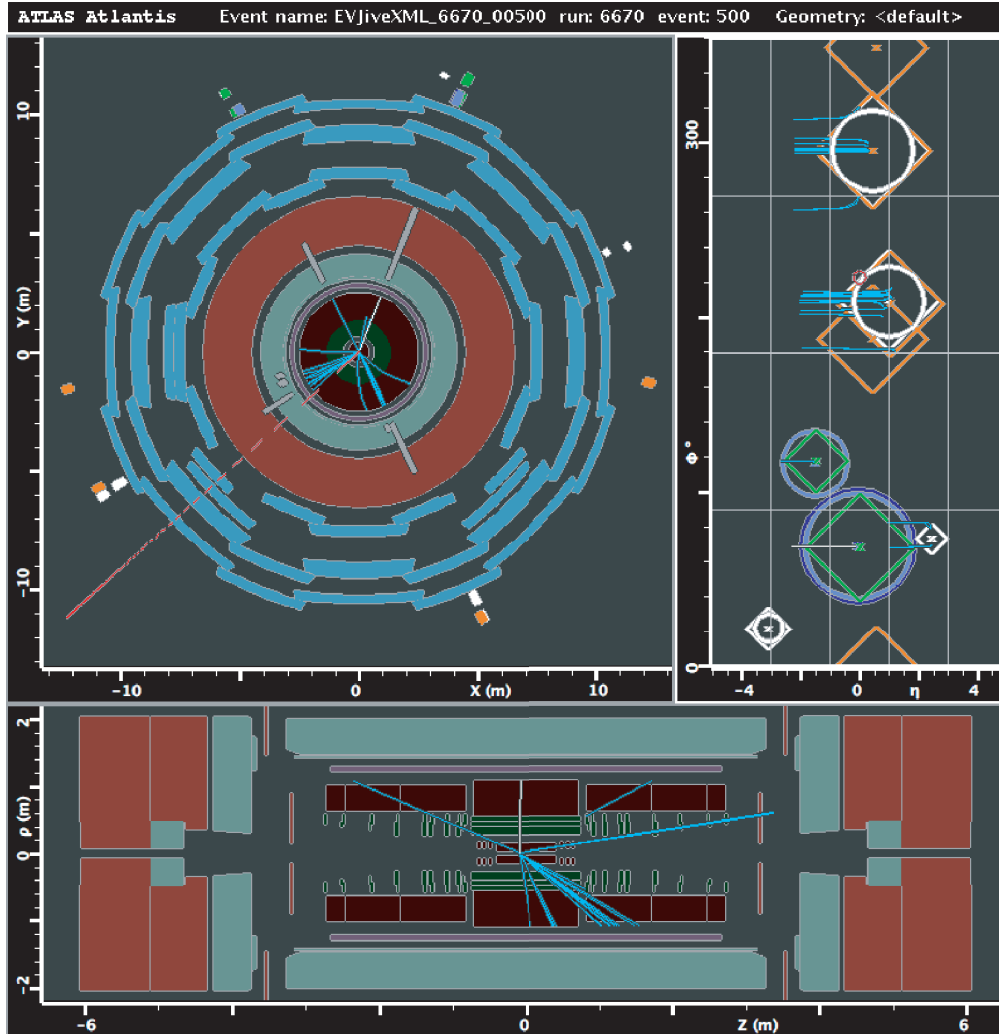


Figure 4.6 A graphical display that shows the results of the reconstruction of the final state objects from an MC simulation of an event where the pair-production of leptoquarks took place. Each leptoquark decays into an electron and a hadronic jet. Upper left hand-side region shows the cross-sectional view of ATLAS with the superimposed reconstructed energy clusters (in grey), as a function of  $\phi$ , in the calorimeters (shown in green and orange annular rings). The corresponding tracks (cyan lines) are reconstructed in the inner detector (annular rings inside the calorimeters). The lower region of the figure shows the longitudinal view of ATLAS with reconstructed tracks in the inner detector (shown in the central part), as a function of  $\eta$ .

## 5.0 SEARCH FOR LEPTOQUARKS IN DIELECTRON CHANNEL

This chapter lays out the analysis carried out to search for the first generation leptoquarks where each leptoquark decays into an electron and a quark. A quark quickly forms a stream of hadrons, and is reconstructed as a “jet”. Therefore the analyzed final state signal objects are two electron candidates and two hadronic jets.

### 5.1 $EEJJ$ CHANNEL

There are several physics processes in the SM that produce the final state  $eejj$ , similar to the pair-production of first generation leptoquarks. These processes are referred to as *physics backgrounds* and are also known as irreducible backgrounds. Another source of background to the leptoquark final states is due to mismeasurements or the instrumental background. These backgrounds are further discussed in the following section 5.3.

The analysis strategy is to identify selection criteria which distinguish the signal from the backgrounds. In reality, one cannot identify each event as a signal event or a background event due to their statistical nature – the probability for the event to be of a signal type or a background type is determined by Poisson statistics. So a signal sample without background contamination cannot be selected. However, one can optimize the selection criteria so as to keep as many signal events as possible while rejecting most of the background events. These optimized selections can be obtained by comparing the kinematics of the signal and the background events in a kinematic phase space. To study the kinematics of leptoquark signal events and various background events, MC simulations (see chapter 4) of the respective events are used. In this study only MC simulated events were analyzed hence the signal

$m_{LQ}$ in GeV	$\sigma(pp \rightarrow LQ\bar{L}Q)$ (NLO) in pb
300	$10.1 \pm 1.5$
400	$2.24 \pm 0.376$
600	$0.225 \pm 0.048$
800	$0.0378 \pm 0.0105$

Table 5.1 NLO cross sections for scalar leptoquark pair production at the LHC.

events refer to signal MC events and the background events refer to the background MC events.

## 5.2 SIGNAL SIMULATION

The signals have been studied using MC samples for first generation (1st gen.) scalar leptoquarks simulated at four masses of 300 GeV, 400 GeV, 600 GeV, and 800 GeV with the MC generator PYTHIA. The next to leading order (NLO) cross sections for leptoquark pair production at 14 TeV  $pp$  center-of-mass energy are shown in Table 5.1 for different leptoquark masses.

## 5.3 BACKGROUNDS

As described above, the backgrounds for the  $eejj$  channel include both the physics background and the background due to mismeasurements. The latter comes from the multi-jet production that can be theoretically described in the framework of Quantum Chromodynamics (QCD).

### 5.3.1 Physics backgrounds

Physics backgrounds result in final states with at least two actual electrons and two quarks/gluons that are reconstructed as jets. The most important physics backgrounds are:  $Z/\gamma^* \rightarrow ee$ , a.k.a Drell-Yan, production in conjunction with jets ( $Z + \text{jets}$ ),  $t\bar{t}$  production with both  $W$  bosons decaying into an  $e$  and a  $\nu_e$ , diboson ( $WW, WZ, ZZ$ ) production in conjunction with jets from the underlying event; with the  $W$  decaying into an  $e$  and a  $\nu_e$  and a  $Z$  decaying into an  $e^+e^-$  or a  $q\bar{q}$ , and a single top quark production in association with a  $W$  boson where top decays into a  $W$  boson and each  $W$  boson decays into an  $e$  and a  $\nu_e$ . Fig. 5.1 shows the Feynman diagrams for the signal and the background processes.

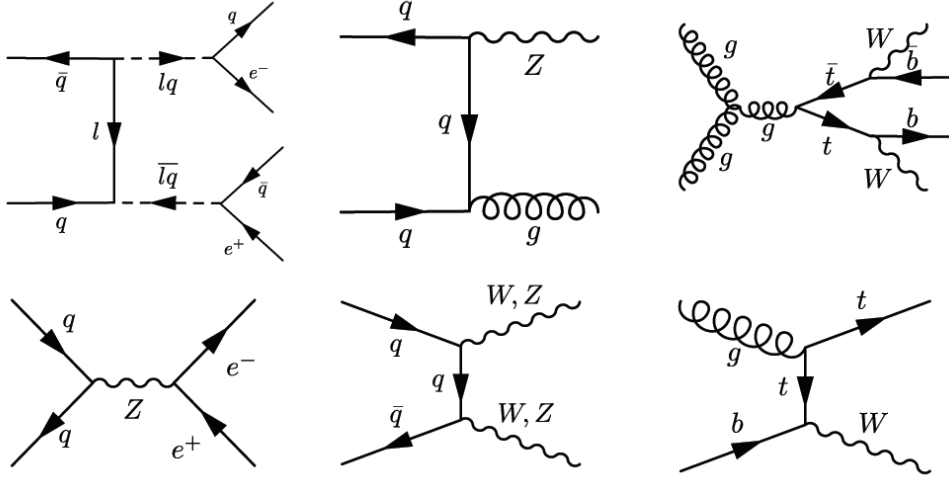


Figure 5.1 Feynman diagrams for signal and background physics processes resulting in  $eejj$  final states.

- Drell-Yan (DY) background is studied using a combination of two MC samples with a generator-level dielectron invariant mass preselection of  $m_{ee} > 60$  GeV and  $m_{ee} > 150$  GeV, the latter sample corresponding to a much larger integrated  $pp$  luminosity than the former. The samples were normalized to the given  $pp$  luminosity using their partial cross sections and the NLO estimate  $\sigma(pp \rightarrow Z) \times \mathcal{B}(Z \rightarrow \ell^+\ell^-) = 2032$  pb, was obtained with the MC generator FEWZ [37].

For logistical reasons, the sample with the lower mass preselection was generated using the MC generator PYTHIA, and the sample with the higher mass preselection is generated using HERWIG. In both cases, the CTEQ6L1 [15] parton distribution functions are used.

The consistency between the two samples is verified at high dilepton masses, where they are found to be in a good agreement with each other.

- $t\bar{t}$  background is simulated using the MC generator MC@NLO [38] using the CTEQ6M [15] parton distribution functions. It is normalized to the given integrated  $pp$  luminosity using a production cross section of 833 pb estimated to the next-to-leading order including corrections (NLO+NLL) [39].
- The diboson samples are generated using HERWIG with a generator-level preselection on the invariant mass of  $Z/DY > 20$  GeV. With this requirement, the NLO partial cross sections for  $WW$ ,  $WZ$  and  $ZZ$  production processes are numerically estimated (using MC@NLO) to be 117.6 pb, 56.4 pb, 17.8 pb, respectively. The CTEQ6L1 parton distribution functions are used for event generation.
- Single top contribution is found to be negligible. More details on the estimation of this background is presented in appendix B

### 5.3.2 Mismeasurement Backgrounds

QCD multi-jet production is the main source of background arising from mismeasurements. For QCD events with four or more jets, if two jets are misidentified as electrons, the event mimics the  $eejj$  final state. The multijet background is simulated using PYTHIA with the CTEQ6L1 structure functions. The normalization is based on the PYTHIA cross section estimates.

## 5.4 FIRST SELECTION CRITERIA OF EVENTS

First level of background suppression is achieved by making quality selections on the reconstructed objects corresponding to the final state under study. This mostly helps in reducing the combinatorial backgrounds due to instrumental and mismeasured objects.

This first or baseline event selection, requires two quality electron candidates and two jets. Electron candidates are identified as

- energy clusters reconstructed in the liquid argon electromagnetic calorimeter that
- match tracks reconstructed in the inner detector and
- satisfy electron identification requirements [40] with
- $p_T \geq 20$  GeV and
- $|\eta| \leq 2.5$ .

Jets are identified as

- energy clusters reconstructed in the calorimeters using a  $\Delta R^1=0.4$  cone algorithm [40] with
- $p_T \geq 20$  GeV and
- $|\eta| \leq 4.5$  with
- $\Delta R$  between a jet and any electron candidate (as defined above) of 0.1 or more.

The latter veto  $\Delta R < 0.1$  is imposed to avoid electrons being misidentified as jets.

To suppress contributions from Drell-Yan backgrounds, the dielectron invariant mass is required to be at least 70 GeV.

Finally, an electron-based trigger is used to select events. More details on it are presented in section 5.6

## 5.5 ANALYSIS

The two highest-Pt electrons and the two highest-Pt jets are selected using the criteria described above to form the  $eejj$  final state combinations. Events are also required to pass the trigger requirements (see 5.6). These events are further analyzed to separate the signal from the backgrounds.

Due to the large leptoquark mass, electrons and jets from signal events have larger transverse momenta than in background events. A good quantity to measure this is the scalar sum of the transverse momenta of the two selected jets and the two signal electron

---

<sup>1</sup> $\Delta R$  is defined as  $\sqrt{\Delta\eta^2 + \Delta\phi^2}$

candidates ( $S_T = \sum |\vec{p}_T|_{jet} + \sum |\vec{p}_T|_e$ ). Fig. 5.2 shows this distribution for the background and the signal events.

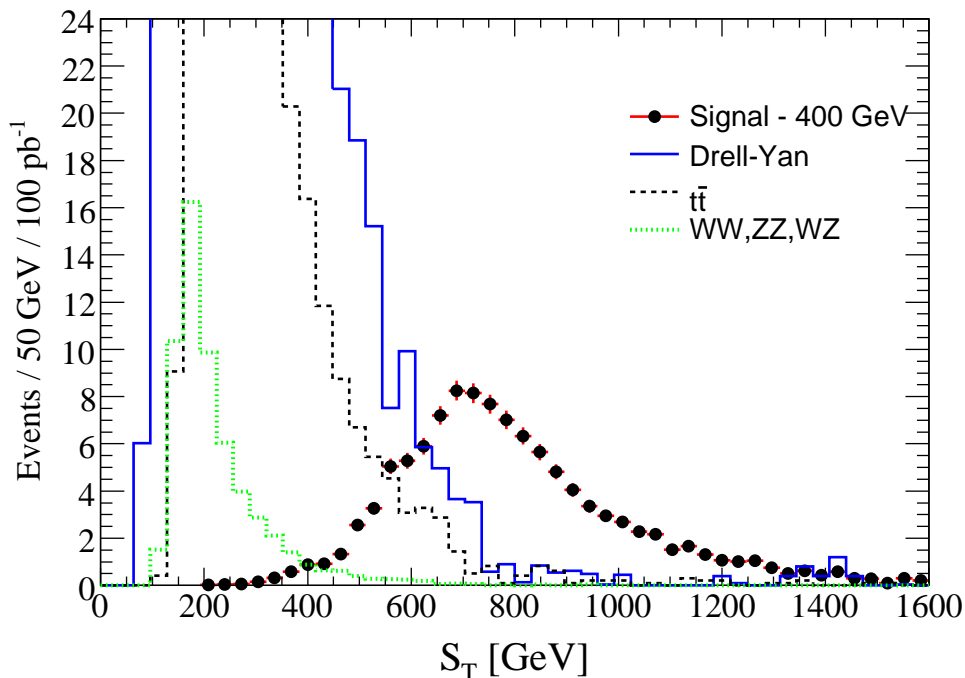


Figure 5.2  $S_T$  distribution from the signal and the background events after baseline selection. The signal is for a leptoquark mass hypothesis of 400 GeV. The distribution is normalized to an integrated pp luminosity of  $100 \text{ pb}^{-1}$ .

There is also substantial contribution from the Drell-Yan process and in particular due to the  $Z$  mass resonance. The distribution of the dielectron invariant mass ( $m_{ee}$ ) is shown in Fig. 5.3

$t\bar{t}$  can be further separated from the signal using the missing transverse energy<sup>2</sup>. However this variable is not considered because its resolving power (as compared to  $S_T$ ) is found to be very limited while the systematic uncertainty associated with its measurement is expected to be large during the first year of data taking.

In the presented analysis the variables  $S_T$  and  $m_{ee}$  are used to suppress the SM backgrounds. The values of the selection criteria on these variables are chosen by achieving the  $5\sigma$  discovery significance for the lowest integrated luminosity. The significance calculator  $S_{cp}$  [41] based on the Poisson statistics is used for this purpose. The lowest luminosity for which the  $5\sigma$  significance is achieved, assuming  $\beta=1.0$ , is found to be  $1.5 \text{ pb}^{-1}$ . Fig. 5.4

<sup>2</sup> Energy in the transverse direction that is carried away by the undetected  $\nu_e$  from the  $W$  boson's decay. This imbalance in energy in the transverse plane is reconstructed as the missing transverse energy.

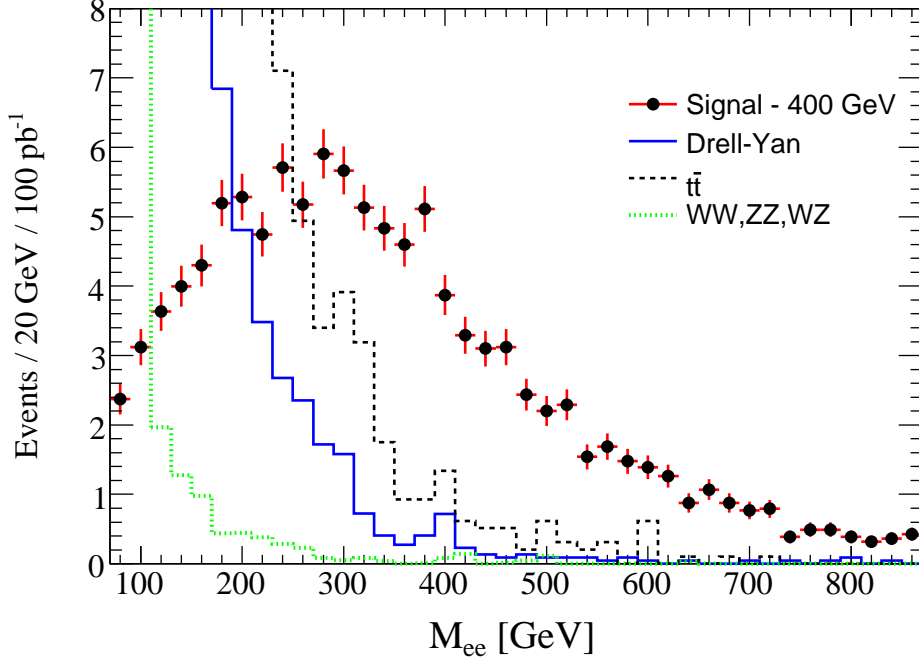


Figure 5.3  $m_{ee}$  distribution from the signal and the background events after baseline selection. The signal is for a leptoquark mass hypothesis of 400 GeV. The distribution is normalized to an integrated pp luminosity of  $100 \text{ pb}^{-1}$ .

shows the significance in the phase space of  $S_T$  and  $m_{ee}$  in the vicinity of optimal values estimated for a leptoquark mass hypothesis of 400 GeV. The optimal values are found around 490 GeV and 120 GeV for  $S_T$  and  $m_{ee}$ , respectively. While optimal values are slightly larger for heavier leptoquarks, following a conservative approach, the same values are used for all leptoquark mass points, therefore events satisfying  $S_T > 490 \text{ GeV}$  and  $m_{ee} > 120 \text{ GeV}$  are further analyzed.

This analysis reconstructs a pair of leptoquark candidates from the  $eejj$  final state. All possible combinations of electrons and jets are studied. This leads to the calculation of four combinations of the  $ej$  invariant mass ( $M_{e_1j_1}$ ,  $M_{e_1j_2}$ ,  $M_{e_2j_1}$ , and  $M_{e_2j_2}$ ), thereby giving rise to two possible pairing scenarios –  $(M_{e_1j_1}, M_{e_2j_2})$ ,  $(M_{e_1j_2}, M_{e_2j_1})$  – for the reconstruction of a pair of leptoquark candidates. The pair yielding the best significance is found to be the one that has the smaller mass difference between the two leptoquark candidates of the pair. The two leptoquark candidates hence reconstructed are shown in Figures 5.5 and 5.6 after baseline selection and after baseline and  $S_T$  and  $m_{ee}$  selections, respectively. The invariant

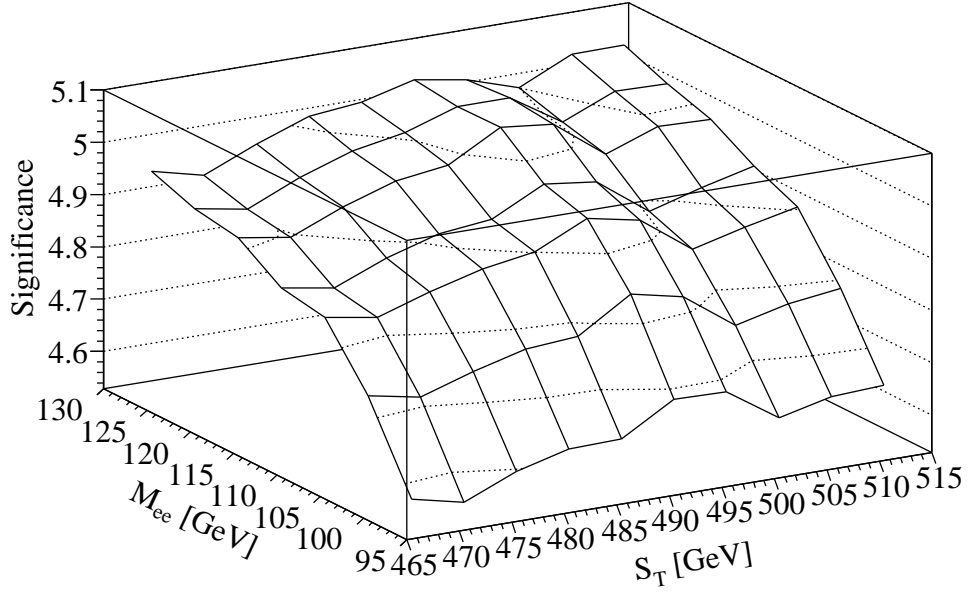


Figure 5.4 Signal over background significance in the  $S_T$ - $m_{ee}$  phase space obtained for a leptoquark mass hypothesis of 400 GeV assuming  $\beta=1.0$ .

mass of an electron and the jet peaks near the actual leptoquark mass, with the broadening of the peak mostly due to the jet energy resolution, the initial and the final state gluon radiation and the random picking of the underlying event jets, instead of the actual signal jets, that could remain undetected when produced at small angles w.r.t. the beam. See Figures 5.7 and 5.8 for the invariant mass distributions of electron-jet (*i.e.* leptoquark) candidates before and after  $S_T$  and  $m_{ee}$  selections. Two entries are plotted corresponding to the two reconstructed leptoquark candidates per event. It must also be mentioned that the jet energy scale calibration is performed using the full MC simulation and requires that the average reconstructed jet energy agrees with the average predicted jet energy. This prediction is made using the MC truth four-momenta of simulated long-lived particles. The same jet reconstruction algorithm, with a cone size  $\Delta R = 0.4$ , is used for both the reconstruction and the calibration. Due to gluon radiation, quarks produced in the decays of heavy particles are not equivalent to the jets reconstructed from the long-lived particles. This shifts the peak of the jet energy resolution function towards a smaller energy and results in a shoulder at low invariant masses for the reconstructed heavy particles.

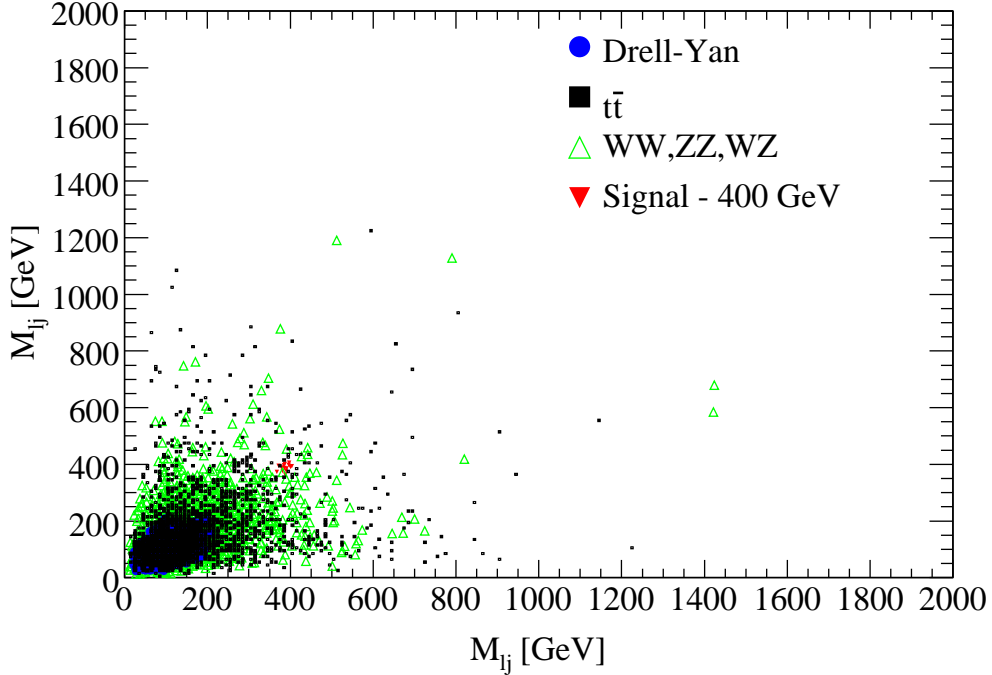


Figure 5.5  $M_{lj}$  versus the other  $M_{lj}$  distribution for the signal and the background events after baseline selection. The signal is for a leptoquark mass hypothesis of 400 GeV. The distribution is normalized to an integrated pp luminosity of  $100 \text{ pb}^{-1}$ .

To estimate the ATLAS sensitivity to a leptoquark discovery, only events with the reconstructed invariant mass of leptoquark candidates close to the actual mass of the simulated leptoquark are selected. The probability for the *two* jets to be misidentified as electrons and, as a result, the probability to reconstruct *two* leptoquark candidates such that they have nearly the same mass is found to be negligibly small. Table 5.2 shows the partial cross sections for the signal and the background processes that survive the discussed selection criteria.

## 5.6 TRIGGER

The trigger system 3.2.4.1 of the ATLAS experiment allows for a flexible programmable selection of inclusive trigger conditions, called the trigger menu, each item in this menu sufficient for triggering on interesting events. The trigger system has three tiers, the L1,

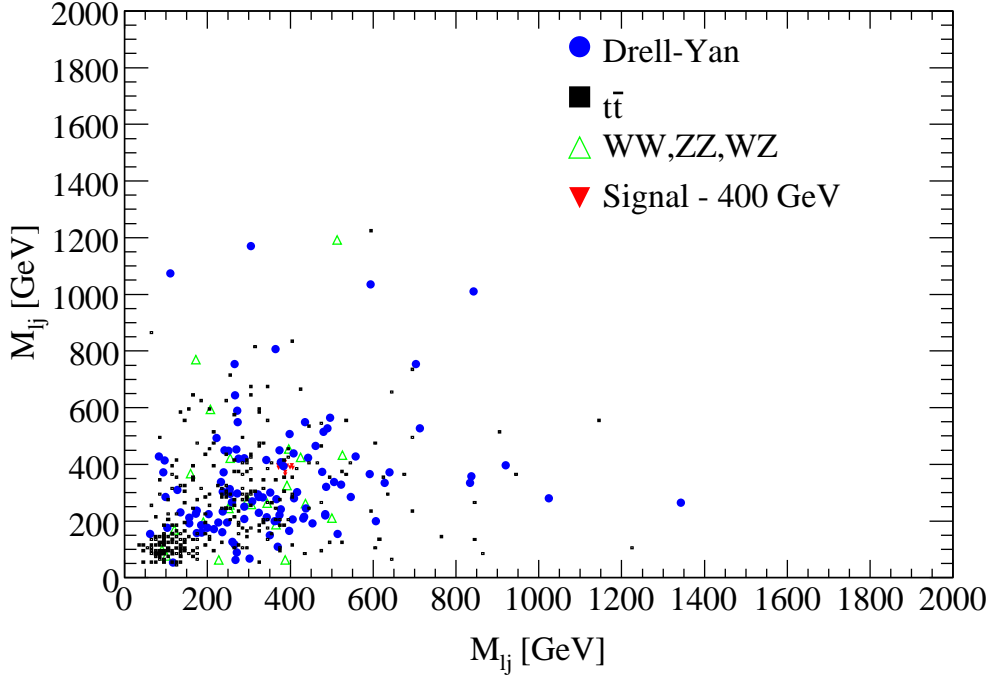


Figure 5.6  $M_{lj}$  versus the other  $M_{lj}$  distribution for the signal and the background events after the baseline selection and the optimized selections of  $S_T$  and  $m_{ee}$ . The signal is for a leptoquark mass hypothesis of 400 GeV. The distribution is normalized to an integrated pp luminosity of  $100 \text{ pb}^{-1}$ .

the L2 and the Event Filter (EF). Individual items for each tier are uncorrelated with each other. However, to consider the event as a candidate to trigger on at a higher-tier trigger, the lower-tier trigger conditions in the same stream must be satisfied.

To ensure the high overall trigger efficiencies, this analysis relies on a single electron trigger stream with a 60 GeV threshold. The 60 GeV-threshold single electron trigger does not require isolation and is almost 100%-efficient for high- $p_T$  electrons at the L1 tier, even when electromagnetic showers created by the electrons have wide profiles. The L2 and the EF apply tighter requirements to the trigger-level electron objects, the efficiencies of these are approx. 95% (86%) at L2 and 97% (94%) at EF in the barrel (endcap) parts of the detector. Overall the electron-based trigger efficiencies are 92% and 81% per electron in the barrel and endcap calorimeters, respectively. When selected events fail this trigger, the analysis relies on a lower-threshold (25 GeV) single electron trigger which is 93%-efficient per electron, when the latter is well-isolated (*i.e.* when the shower has a compact lateral shape).

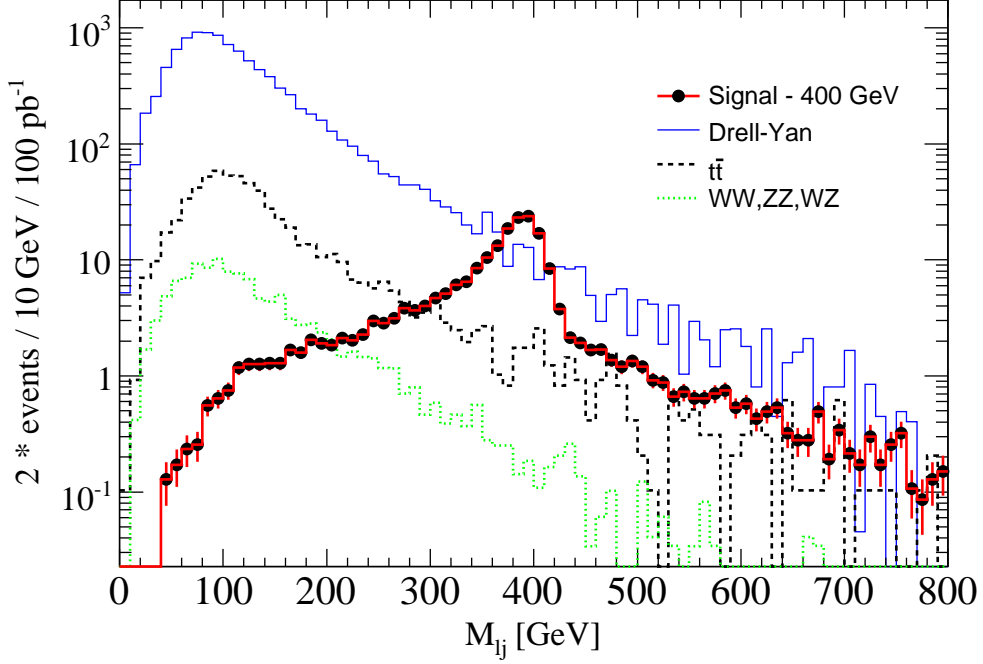


Figure 5.7 Electron-jet invariant mass distribution for the signal and the background events after the baseline selection. Two entries per event are plotted corresponding to the two reconstructed leptoquark candidates. The signal is for a leptoquark mass hypothesis of 400 GeV. The distribution is normalized to an integrated pp luminosity of  $100 \text{ pb}^{-1}$ .

Final states studied in this analysis always contain two high- $p_T$  electrons. While the baseline selection requires two electrons with  $p_T > 20 \text{ GeV}$ , most signal events contain at least one electron with a significantly higher  $p_T$ . As a result, the overall trigger efficiency for events that satisfy all selection criteria exceeds 95%. These offline trigger efficiencies for the signal MC events that satisfy all selection criteria are shown in Table 5.3.

## 5.7 SYSTEMATIC UNCERTAINTIES

All measurements have systematic uncertainties (also called systematic errors) associated with them. In inferring any conclusions from the results of experimental measurements, the sources of systematics need to be understood and the uncertainties have to be properly taken into account.

The largest systematic uncertainty is due to imprecise knowledge of the integrated lumi-

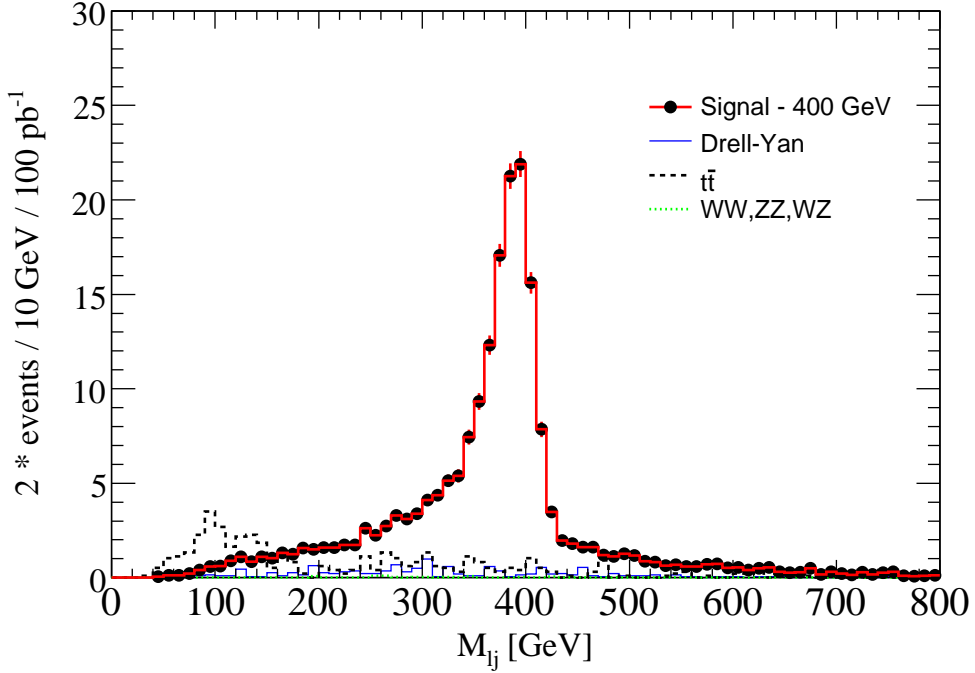


Figure 5.8 Electron-jet invariant mass distribution for the signal and the background events after the baseline selection and the optimized selections of  $S_T$  and  $m_{ee}$ . Two entries per event are plotted corresponding to the two reconstructed leptoquark candidates. The signal is for a leptoquark mass hypothesis of 400 GeV. The distribution is normalized to an integrated pp luminosity of  $100 \text{ pb}^{-1}$ .

osity of early LHC data. There are three ways to measure the integrated luminosity at the LHC:

- by using the beam parameters directly (see section 3.1),
- by measuring the elastic scattering of proton-proton collisions with dedicated detectors,
- by analyzing well-known physics processes, such as  $Z$  boson production, whose cross-section is known accurately.

For the last method, it is also required to know the reconstruction and trigger efficiencies, the geometric acceptance of the detector, the dead-time of the detector and the data acquisition system. The systematic uncertainty on luminosity is expected to be approx. 20% for early LHC data, which is due to the accuracy of dedicated detectors developed to measure instantaneous luminosity.

Evaluating ATLAS sensitivity to leptoquark discovery requires to estimate the contribution from SM backgrounds. However, their cross sections depend on assumptions made

Physics sample	Before selection	Baseline selection	$S_T$ $\geq 490$ GeV	$M_{ee}$ $\geq 120$ GeV	$M_{l_j}^1 - M_{l_j}^2$ mass window [ 320-480 ] - [ 320-480 ] [GeV]
LQ (400 GeV)	2.24	1.12	1.07	1.00	0.534
$Z/DY \geq 60$ GeV	1808.	49.77	0.722	0.0664	0.0036
$t\bar{t}$	450.	3.23	0.298	0.215	0.0144
VB pairs	60.94	0.583	0.0154	0.0036	0.00048
Multijet	$10^8$	20.51	0.229	0.184	0.0

Table 5.2 Partial cross sections (pb) that survive the selection criteria for this analysis. The  $Z/DY$  cross section is for the region  $M_{ee} \geq 60$  GeV. The offline trigger efficiency for the signal events that pass all selection criteria exceeds 97% but is not included in this table.

Process	L1	L2	EF	L1*L2*EF
leptoquarks $m_{LQ} = 400$ GeV	100.0%	99.4%	97.6%	97.0%

Table 5.3 Overall trigger efficiencies for the signal events that satisfy all the selection criteria.

about PDFs that are measured with finite precision. In addition, systematics arise from using different PDF sets (CTEQ6.1 and MRST2001E) [42]. The systematic uncertainties on the cross sections of  $t\bar{t}$ , and Drell-Yan processes are estimated to be 12% and 10%, respectively. These uncertainties are evaluated using the largest error from the subsets of the two PDF sets, and by varying the renormalization and the factorization scales.

The systematic uncertainty on the leptoquark production cross section was estimated by taking the 40 PDF CTEQ6M sets (two per eigenvector of PDF variations), and recalculating the leptoquark cross section with each of these sets, and taking the largest difference of the two variations for each of the 20 eigenvectors to the cross section calculated with the standard CTEQ6M set. The estimate is the quadratic sum of these 20 differences and the relative difference in cross section obtained by varying renormalization and factorization scales by a factor of 2. The systematic uncertainty is 15% for the tested leptoquark mass of 400 GeV.

The number of reconstructed leptoquark candidates depends on how accurately final state objects' four-momenta are measured. There are uncertainties associated with the jet and electron energy scales, where the jet contribution is dominant. Also, the uncertainties

in expected energy resolutions have to be taken into account.

The uncertainties on the jet energy scale for early ATLAS data are estimated to be  $\pm 10\%$  and  $\pm 20\%$ , for  $|\eta_{jet}| \leq 3.2$  and  $|\eta_{jet}| > 3.2$ , respectively. These uncertainties are estimated using jet cluster energy calibration techniques [40] applied to the misaligned and the ideal geometries of the apparatus. Estimates were performed using misaligned geometry because in the initial period of the data taking the exact geometry of the various sub-detectors relative to each other will not be known with sufficient accuracy yet.

There is also systematic uncertainty associated with the (relative) jet energy resolution. Jet energy resolution depends on intrinsic resolution of calorimeter cells, the energy reconstruction algorithm (e.g. towers or clusters), the jet reconstruction algorithm, the underlying event and pile-up activity, and the general particle density and energy flow in the physics environment. This systematic error is estimated using a Gaussian smearing of the jet energies in such a way that the relative jet energy resolution<sup>3</sup> widens from  $0.60/\sqrt{E} \oplus 0.05$  to  $0.75/\sqrt{E} \oplus 0.07$  for  $|\eta_{jet}| \leq 3.2$ , and from  $0.90/\sqrt{E} \oplus 0.07$  to  $1.10/\sqrt{E} \oplus 0.10$  for  $|\eta_{jet}| > 3.2$ , where  $E$  is in GeV. Here the sampling term values of 0.60 and 0.90 for  $|\eta_{jet}|$  less than 3.2 and greater than 3.2, respectively, are the typical stochastic terms for the hadronic calorimeters determined by using QCD dijets MC [40]. These terms deteriorate to 0.90 and 1.10, respectively, when determined using misaligned apparatus' geometry and this difference is a measure of systematic uncertainty due to jet energy resolution. The same estimates apply to the constant terms in the jet resolution function.

For the electron identification and reconstruction efficiency, an uncertainty of 1% per electron is estimated [40]. To study uncertainties on electron identification and reconstruction, two electromagnetic shower shape variables (see section 4.3.2) are studied as a function of the amount of material in front of the EM calorimeter after adding some additional material. Additional material results in broadening of shower thereby reducing the efficiency to reconstruct and identify electrons. This change is estimated to be about 1%.

Uncertainties in the electron energy scale and  $p_T$  resolution are estimated using MC for Higgs boson decaying into four electrons [40] for both the ideal and the misaligned

---

<sup>3</sup> energy resolution of a sampling calorimeter is given by  $\sqrt{(\frac{a}{\sqrt{E}})^2 + b^2}$ , where 'a' is called the sampling term and 'b' is called the constant term; it is also conveniently represented by  $a/\sqrt{E} \oplus b$

geometries of the apparatus. Uncertainty on electron energy scale is estimated to be  $\pm 1\%$  and on electron  $p_T$  resolution to be (relative) 20%. This 20% uncertainty in electron  $p_T$  resolution is included by introducing an additional 20% Gaussian smearing of the nominal relative  $p_T$  resolution of  $0.66 * (0.10/\sqrt{p_T} \oplus 0.007)$  ( $p_T$  is in GeV/c), where the two widths are combined in quadrature.

1% is used for the uncertainty in the overall trigger efficiency. The signal electrons in this analysis are high  $p_T$  and therefore L1 trigger is almost 100% efficient. Electron trigger efficiency measurements using “*tag-and-probe*” techniques [40] are estimated to be less than 0.1%. Therefore any uncertainty is dictated by uncertainty in the reconstruction of the electrons in the trigger chain. This is similar to that in the offline reconstruction and identification of the electrons. Hence 1% is used for the uncertainty in the trigger efficiency in this analysis.

Statistical uncertainties on the number of the signal and the background MC events are treated as systematic uncertainties on the number of events.

Systematic uncertainties affect both the signal and the background events. The size of the effects, in many cases, depends on the selection criteria. The relative uncertainty on the number of the selected signal and background events are listed in Table 5.4.

## 5.8 RESULTS

The program  $S_{cp}$  is used to calculate the significances of the possible observations of the signals studied in this analysis. The significance is defined in units of Gaussian standard deviations, corresponding to the (one-sided) probability of observing a certain number of events exceeding the MC-predicted background  $N_b$  at a given integrated  $pp$  luminosity. This probability is usually referred to as  $CL_b(N)$ , where  $N$  is the number of observed events. The  $5\sigma$  discovery corresponds to  $CL_b(N_s + N_b)$ , where  $N_s$  is the expected number of signal events. Systematic uncertainties in the number of background events are also included in the significance calculations. For a given luminosity, the signal selection is optimized to minimize the cross section times branching ratio needed to reach a  $5\sigma$  discovery.

The overall reconstruction and trigger efficiencies discussed in Section 5.5 are used to estimate the ATLAS sensitivity and discovery potential for the studied final state. To produce these plots the expected numbers of signal and background events in the signal region, as discussed in Section 5.5, are reduced by the trigger inefficiencies estimated according to the information shown in Table 5.3.

The integrated  $pp$  luminosity at 14 TeV center-of-mass energy needed for a  $5\sigma$  discovery of the leptoquark signals are shown in Table 5.5 as function of the leptoquark mass, assuming  $\beta = 1$ . Also, Fig. 5.9 predicts the integrated  $pp$  luminosities (14 TeV center-of-mass energy) needed for a 400 GeV leptoquark mass hypothesis, with the various values of  $\beta^2$ , at a  $5\sigma$  level.

Finally, Fig. 5.10 shows the minimum  $\beta^2$  that can be probed with the ATLAS with  $100 \text{ pb}^{-1}$  of integrated  $pp$  luminosity at 14 TeV center-of-mass energy as a function of the leptoquark mass. Lighter leptoquark mass can be probed with a smaller  $\beta$  because of their larger cross-section. It is evident from this figure that ATLAS is sensitive to leptoquark masses of about 565 GeV at the given integrated  $pp$  luminosity at 14 TeV center-of-mass energy, provided they always decay into charged leptons and quarks. An estimate for 10 TeV center-of-mass energy of proton-proton collisions at the LHC was also performed. ATLAS is sensitive up to masses of 450 GeV for  $100 \text{ pb}^{-1}$  of the integrated  $pp$  luminosity at 10 TeV center-of-mass energy.

systematic uncertainty	effect on number of signal events	effect on number of background events
Integrated luminosity	20%	20%
LQ cross-section	15%	-
high-mass DY cross-section	-	1.2%
$t\bar{t}$ cross-section	-	7.2%
electron identification and trigger	4%	4%
electron resolution	0.3%	4%
electron energy scale	1%	11%
jet energy scale	4%	13%
jet resolution	0.5%	2%
statistical uncertainty of MC	3%	12%
quadratic sum of all uncertainties	26%	30%

Table 5.4 Overview of the systematic uncertainties on the first generation leptoquark for a mass hypothesis of 400 GeV.

Tested leptoquark mass	Expected luminosity needed for a $5\sigma$ discovery
300 GeV	2.8 pb <sup>-1</sup>
400 GeV	11.8 pb <sup>-1</sup>
600 GeV	123 pb <sup>-1</sup>
800 GeV	1094 pb <sup>-1</sup>

Table 5.5 The integrated  $pp$  luminosities at 14 TeV center-of-mass energy needed for a  $5\sigma$  discovery for leptoquark at different mass hypotheses.

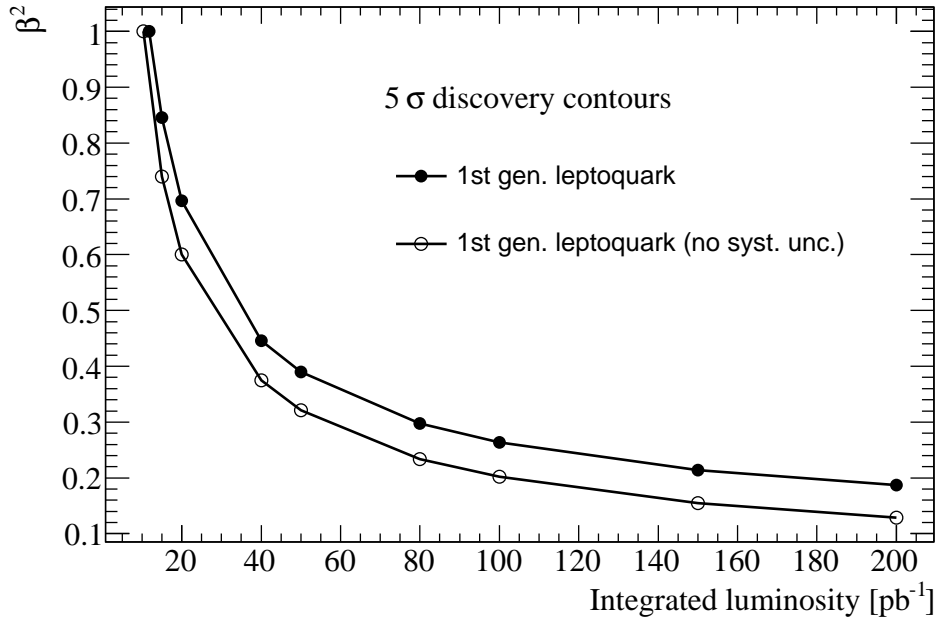


Figure 5.9  $5\sigma$  discovery potential for the first generation 400 GeV leptoquark versus  $\beta^2$  with and without the background systematic uncertainty included.

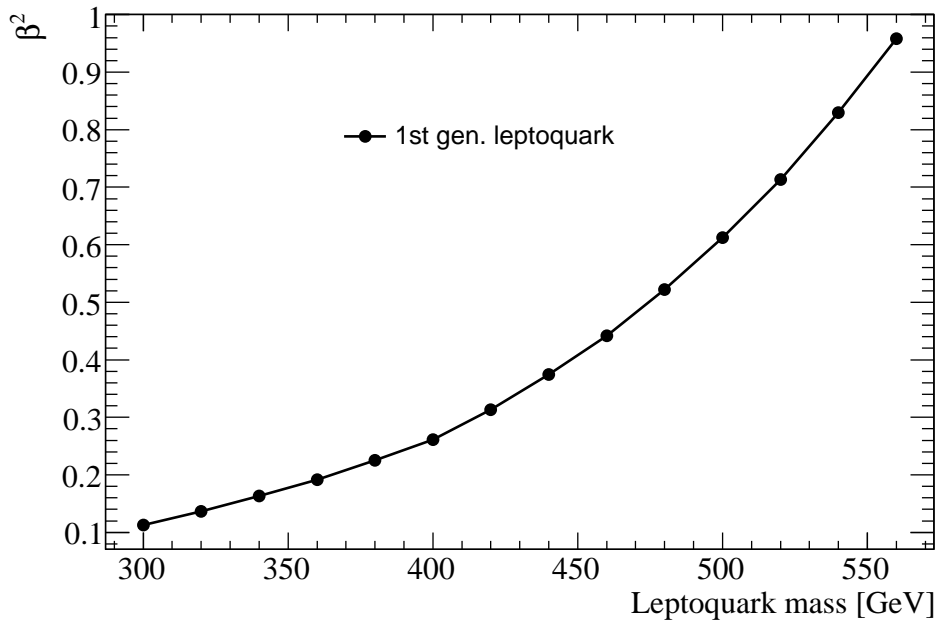


Figure 5.10 Minimum  $\beta^2$  of a scalar leptoquark versus leptoquark mass at  $100 \text{ pb}^{-1}$  of integrated  $pp$  luminosity at 14 TeV center-of-mass energy at  $5\sigma$  (background systematic uncertainty included).

## 6.0 RECEIVER/MONITORING SYSTEM OF ATLAS

ATLAS group at the University of Pittsburgh designed, built, installed and commissioned the L1 trigger interface for the Liquid Argon (LAr) and Tile calorimeters of the ATLAS detector. This part of the detector system is referred to as the Receiver/Monitoring (R/M) system. Its design and testing were done at the University of Pittsburgh, the installation and commissioning took place at the apparatus site at CERN, Geneva. During the course of this work I played the leading role in the development of quality control (QC) and quality assurance (QA) procedures for R/M electronics at the University of Pittsburgh and later worked on the installation, commissioning and integration of our system with the rest of ATLAS at CERN. QC/QA work required developing test procedures, writing algorithms, supervising undergraduate students, troubleshooting the problems, finding the solutions and improving the design of the system. This chapter describes the R/M system and my contributions in its building, installation, and commissioning.

### 6.1 INTRODUCTION

ATLAS, as discussed in chapter 3, is a large general-purpose detector designed for operation at the Large Hadron Collider (LHC) at CERN. LAr calorimeters represent one of the major ATLAS detector subsystems 3.2.2. Given the fine segmentation of the ATLAS LAr calorimeters, a total of 0.2 million active channels have to be read out to be able to reconstruct the energy deposited in the calorimeters by particles such as electrons. Figure 6.1 shows the electronic readout for the system. The R/M system [43,44] in the figure is the block labelled “L1 interface”. R/M system forms the boundary between the LAr electronics and the Level

1 trigger electronics. It delivers analog output signals whose amplitudes are proportional to the transverse energy deposited in the towers of the LAr calorimeters to the first level of ATLAS trigger system (Level 1 trigger). In addition, the R/M system permits monitoring of the analog signals from the calorimeters and can be used to diagnose potential trigger problems.

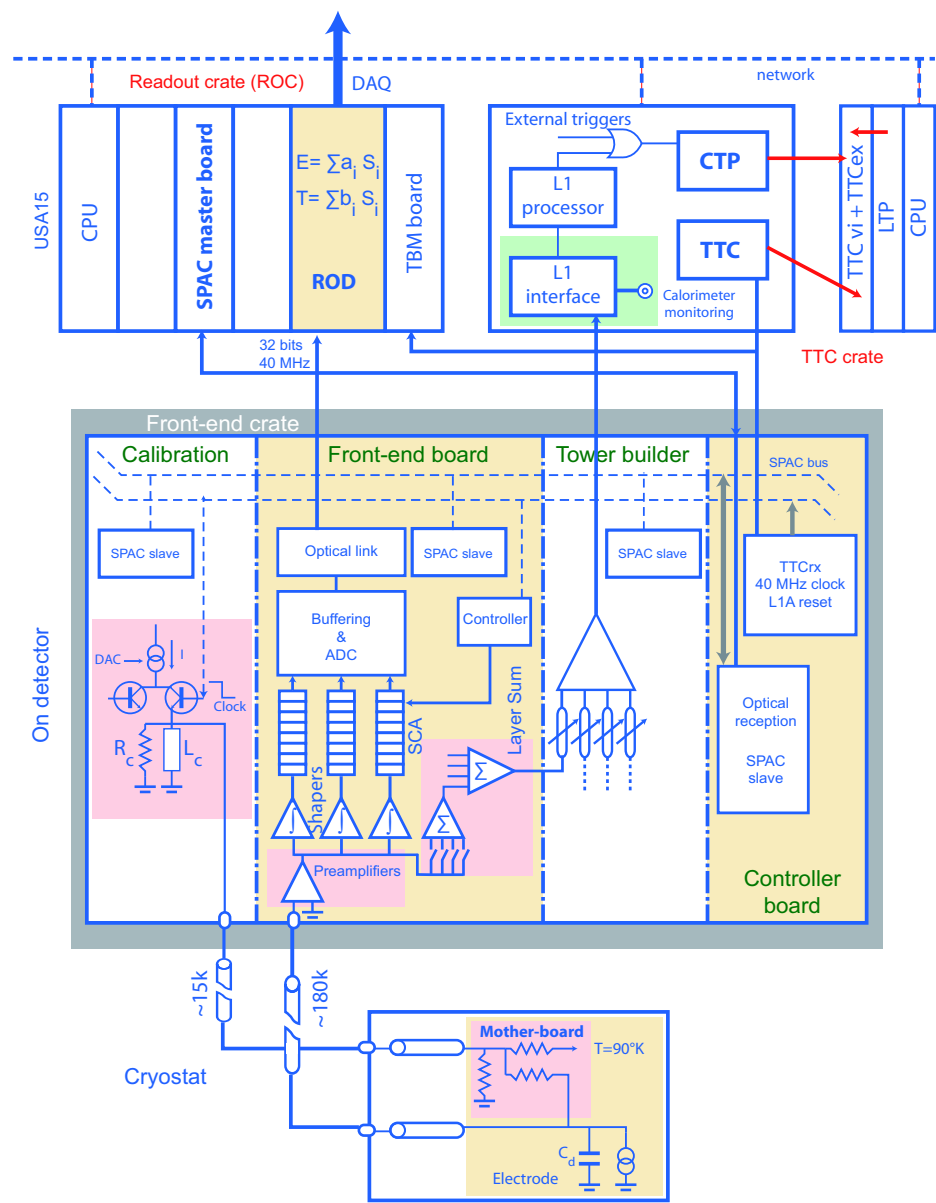


Figure 6.1 Block diagram depicting the architecture of the ATLAS LAr readout electronics. The lower box represents the calorimeters installed in their respective cryostat. The central box illustrates the schematics of the electronics used to read out the calorimeter. The upper box shows the off-detector electronics which include the trigger and the L1 interface (highlighted in green color box)

### 6.1.1 Receiver/Monitor System

The receivers are the interface between the Front End (FE) electronics of the calorimeters and the Level 1 calorimeter-based trigger. The receivers are located off the detector in a nearby underground service area (USA15). The system consists of eight receiver crates, four serving each side of the detector. Each receiver crate includes 16 transition boards, 16 receivers, two monitoring boards, and one controller board.

The R/M system has the following functions:

- a) Differential receiver: the analog trigger signals from the detector arrive to the USA15 in shielded twisted-pair cables. The first section of each receiver is a wideband stripline transformer, which converts differential signals to single-ended (locally grounded) signals.
- b) Gain adjustment. A critical active element in the receiver is the variable gain amplifier whose gain is set by a direct current (DC) voltage provided by a 12-bit digital-to-analog converter (DAC), configured such that the gain of each receiver channel can be varied between 0 and 2.
- c) Reordering of signals. The signals arrive at the receivers in an order determined by the physical layout of the calorimeters. The L1 electronics require the signals ordered in a specific pattern in  $(\eta, \phi)$  space. This reordering is done via a “remapping” daughterboard located on each receiver.
- d) Summation. Most of the summing of the L1 trigger signals is carried out by the on-detector electronics (trigger tower builders). However, there are certain cases where it is necessary to make additional summing in USA15, *e.g.*, for trigger towers that comprise of cells from both the barrel and the endcap LAr detectors. This summing is being done in both the receivers and the L1 preprocessor.
- e) Monitoring. In the main readout of the calorimeter, the signals are directly digitized in the FE electronics. Thus the only place where analog signals can be examined is by analyzing the (analog) trigger sums, the output of which goes to the R/M system. The receivers contain monitoring pickoffs for each channel, and routing circuitry permits any input signal to be routed to any output of either of the two monitoring modules in each receiver crate.

f) Differential driver. The final stage of the receiver electronics chain is a transformer-coupled differential driver. The outputs of the receivers are sent to the L1 preprocessor module over twisted pair cables identical to the input cables.

A schematic diagram of the chain of electronics which performs the described functions is shown in figure 6.2.

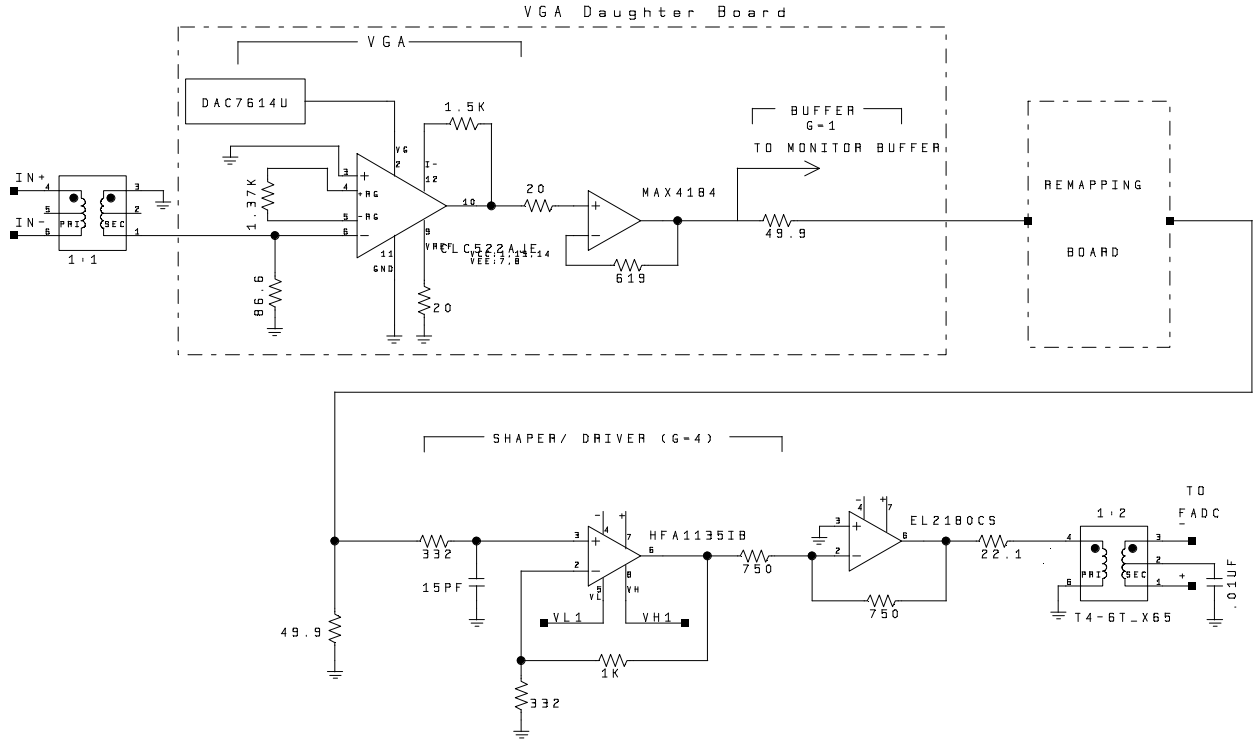


Figure 6.2 Diagram of the analog circuitry for one receiver channel. The (incoming) trigger sum cable is shown at the upper left, and the output to the cable leading to the L1 preprocessor is shown at the lower right.

After passing through the 1:1 input transformer, where the conversion from the differential to the single-ended mode is carried out with the output inverted, the signal enters the VGA (variable gain amplifier) daughterboard. Here it is inverted again and amplified by a gain (max value=2.0) to adjust the signal level to its correct amplitude (10mV=1 GeV at the ADC (analog-to-digital converter) input). The gain is changed by adjusting the value of

a DAC which is also located on the VGA daughterboard. A DAC value of 4096 corresponds to a gain of 2, while a DAC value of 0 corresponds to a gain of 0. At the exit of this daughterboard, the signal, is sent to both a buffer amplifier and to the remapping board. The signal in the monitoring branch is sent to a buffer amplifier, where it enters the monitoring circuitry. The signal sent through the remapping board becomes transposed in its position among the output signals to the ordering required by the L1 calorimeter-based trigger. It then undergoes an RC shaping ( $\tau=5$  ns) to provide the bandwidth filtering and amplification by a fixed gain of 2. This final factor of 2 serves as an approximate compensation for the signal attenuation in the 70 meter-long twisted-pair cables from the detector. A differential driver consisting of an amplifier and a 1:2 wideband transformer converts the signal back to the differential mode (with its original polarity) for transport over twisted-pair cables to the preprocessor of the L1 trigger system.

Each receiver motherboard has 64 channels, and contains four VGA daughterboards, one remapping daughterboard, and one serial control daughterboard (SCDB).

The remapping board [45] is a 253 mm  $\times$  50 mm PCB (printed circuit board) located in the center of the receiver motherboard. Its purpose is to change the ordering of the signals from the input ordering to the one required by the L1 system. It is, in most cases, totally passive, the exception being for the case where the two-fold sums are carried out in the receiver for the transitional region between the barrel and the endcap LAr calorimeters.

The SCDB sends and receives digital data over the crate backplane. Mounted directly on the receiver motherboard are the shaper/driver circuitry and the circuitry for driving the monitoring lines, which are located in the crate backplane. A photograph of the receiver and the transition modules in a test bench setup is shown in Fig. 6.3.

Monitoring is accomplished in this system by picking off an input signal and routing it into one of the 16 monitoring channels. Two monitoring boards, each handling 8 channels, present the output of the monitoring lines on two output connectors, one with a shaping identical to the signal output and the other with additional filtering, designed to have a sensitivity to the different regions of the noise spectrum. The heart of the monitoring circuitry is a crosspoint switch, located physically on the VGA daughterboard. This device routes a signal on one of its 16 inputs to any of its 16 outputs. The four crosspoint switches

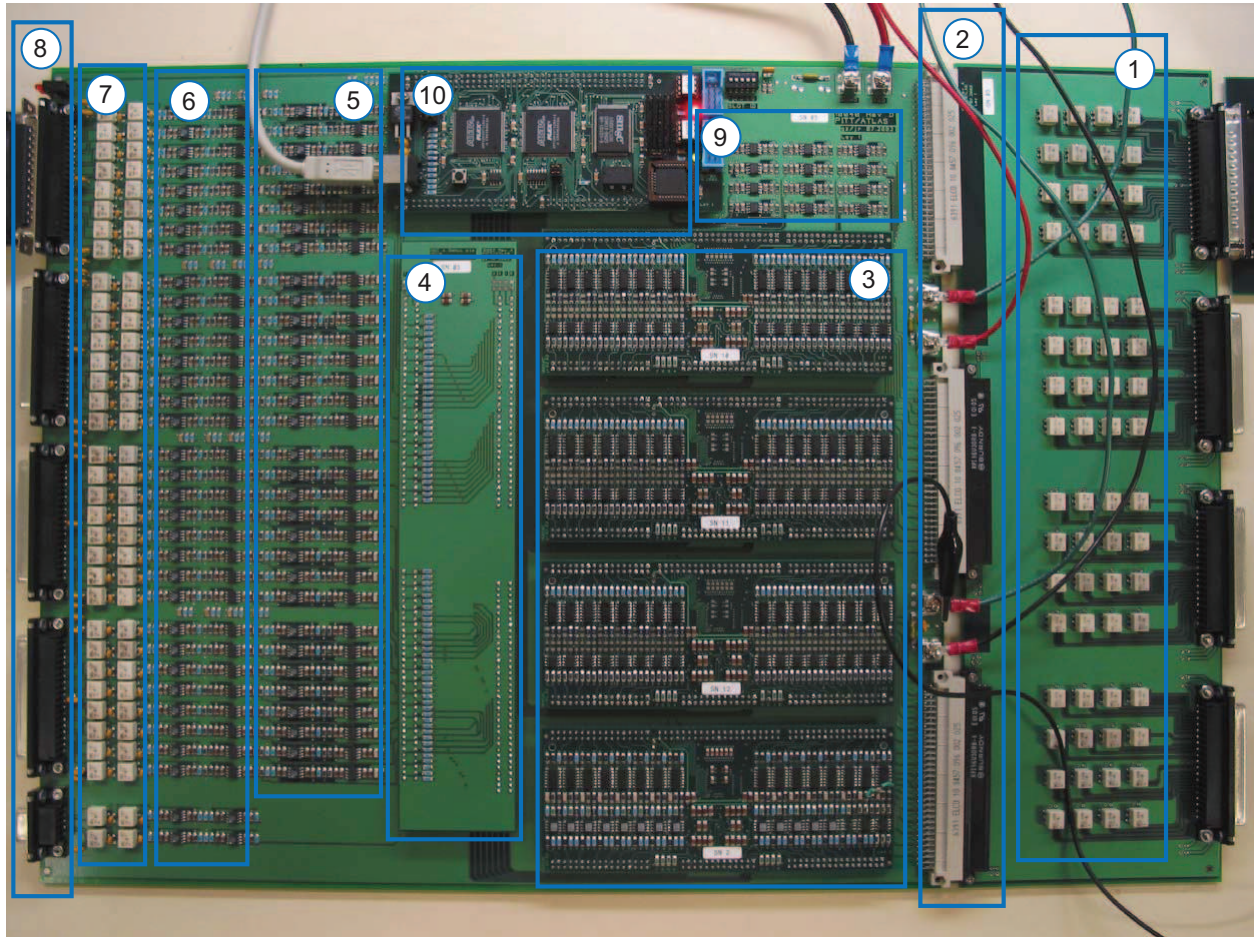


Figure 6.3 Photograph of the receiver and the transition boards in a test setup. The signals enter on the right side at the front panel of the transition module. The elements through which the signals pass can be identified (right to left) as (1) input transformers, (2) backplane connectors, (3) VGA daughterboards, (4) remapping board, (5) voltage limiting circuitry, (6) output drivers, (7) output transformers, (8) output connectors on receiver motherboard, and (9) are drivers for monitoring channels. The SCDB, (10), is a special test bench version with a USB interface, permitting direct control of the receiver module with a computer. The monitoring line drivers are located just to the right of the SCDB.

in a receiver module are bussed together in such a way that any of the 64 channels in a receiver module can be routed to any of the 16 monitoring channels. The signals pass through a buffer amplifier with an output enable. In the monitoring module, the same chip is used (see Fig. 6.4) to select which of the receiver modules are to be transmitted to the monitoring outputs. Enabling the signal at both the source and the receiver ends is not logically necessary, but this arrangement reduces possible crosstalk between the active and the inactive monitoring lines in the backplane. The gain in the receiver chain is chosen to make equal the monitoring signal and the signal on the front panel of the receiver. Due to attenuation in the backplane, which depends on the position of the receiver, this equality is accurate only to the level of a few percent.

The R/M system is computer-controlled via USB. The controller module, which resides in the slot 1 of each receiver crate, contains two USB ports. One is dedicated for the data acquisition system and is the port through which all the digital data are transmitted, including the gain data as well as the monitoring setup data, and the identification information is read from the receiver modules. The second port is used solely for monitoring purposes, and it therefore implements a much more restrictive set of instructions available to the computer connected to it.

Communications between the controller and the receiver or the monitoring modules are carried out using a serial link running at 6 MHz. As mentioned above, each receiver or monitoring board contains an SCDB, which communicates with the controller and carries out the required digital operations on the board. More information on the digital communications in the receiver system can be found elsewhere [46].

Due to the fact that the receiver modules must rearrange the signal ordering between the input and the output, it is of utmost importance that the receivers are placed in the slot for which they were configured and that each module is correctly configured to its slot. For this reason, all the daughterboards and the receiver motherboard have been given electronically readable ID numbers (reprogrammable using DIP switches).

The (custom) crate backplane has several functions. Each receiver or monitoring module contains three 96-pin connectors (mechanically, the backplane conforms to the standard used for VME) which mate with the connectors on the backplane. On the receiver, the two lower

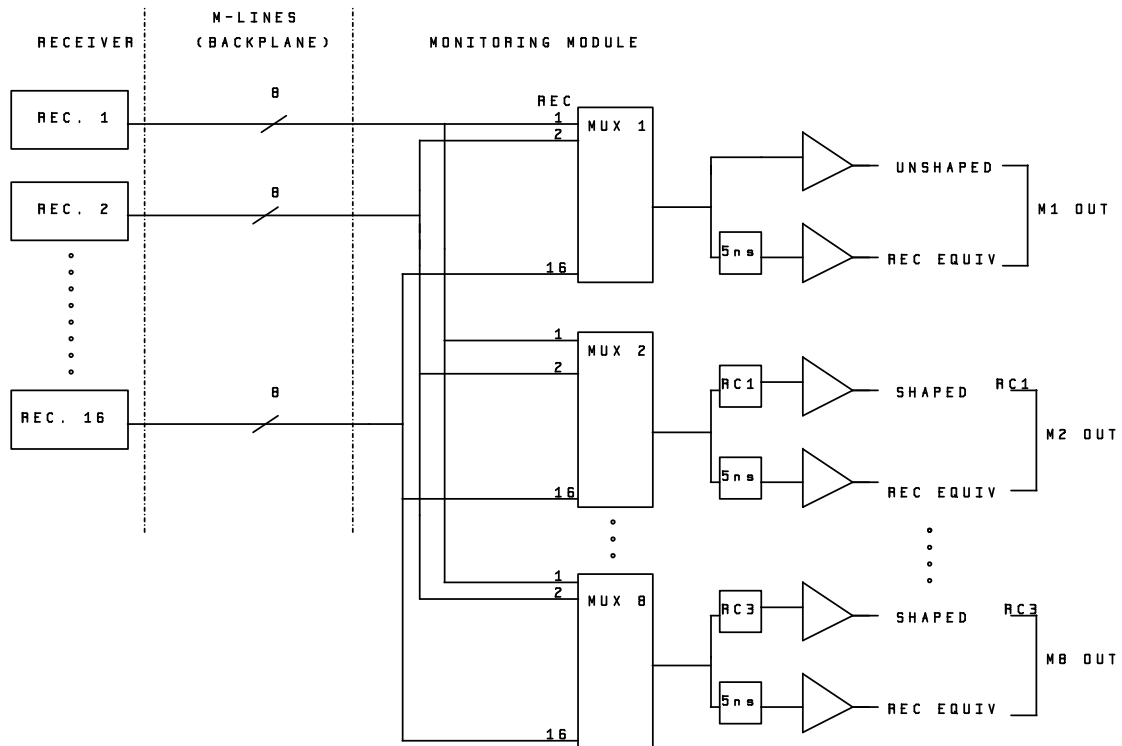


Figure 6.4 Block diagram of the monitoring module.

connectors are used to transport the signals from the transition module into the receiver module. The upper connector is used to transmit the digital signals from the controller to each receiver module over a common set of lines, which are carried by the backplane. The bus of this connector is also used to transport the 16 monitoring signals out of the receiver module. On the monitoring module, the two lower connectors are used as the input of the 128 monitoring lines from the 16 receiver modules, and the upper connector is used for digital communications. The traces in the backplane carry the monitoring signals from the receivers to the monitoring boards. Monitoring lines 1 through 8 are sent to monitoring board No. 1, which occupies the slots 2 and 3, while lines 9 through 16 are transmitted to the monitoring board No. 2 located in the slots 4 and 5. Power is also distributed over the backplane, using the power bus provided by the crate manufacturer (WIENER).

Analog power for the system is provided by two 100 A power supplies running at  $\pm 5$  V (one for each polarity). Digital power is provided by an identical but separate +5 volt power supply. A full crate consumes about 730 watts, and is air cooled in a closed rack with recirculating water-cooled air.

### 6.1.2 Performance tests

Several automated test stations were set up to evaluate the performance of electronic circuit boards of the receiver system. A complete description of the testing program is contained in reference [47]; here the results of the more important tests are highlighted.

The most critical component in the analog chain is the VGA, for which its own test bench was developed (see Fig. 6.5). In the VGA test bench each unit was evaluated thoroughly for dynamic range and linearity. Fig. 6.6 shows how the integral nonlinearity is evaluated for each channel of the VGA daughterboard. In this test a standard value of the DAC (2700) is used, which corresponds to a gain of about 1.4. A DC signal is ramped at the input, from -3.5 V to +3.5 V, and the output is measured on a digital voltmeter, yielding the DC response curve for each of the 16 channels (see Fig. 6.7). The slope of this curve is the gain, which is evaluated separately for each channel. The integral nonlinearity is evaluated separately for negative and positive voltages. One thing to notice is that the response curve is asymmetric, with a larger dynamic range for negative voltages. This is a property of the variable gain op-amp used in the system, and is the reason why a double inversion of the signal in the receiver is necessary.

Another quantity which is measured for the VGA is the variation of the gain as the control voltage is varied using the DAC on the VGA daughterboard (see Fig. 6.8). This relationship is a linear one, and the behavior can be quantified by nonlinearity, but in our application it is not essential for the gain vs the voltage relationship be linear, as the gains are set iteratively. The gain nonlinearity is better than 1% over the full range. A total of 512 VGA daughterboards were tested before installing them on the receiver boards.

One of the more important quantities measured in our acceptance tests is the overall integral nonlinearity of the receiver circuit. This measurement was carried out using another test bench shown in Fig. 6.9. This measurement, carried out with bipolar pulses of 38 ns rise time, simulates closely the signals to be encountered in the experiment. Due to the short rise time of the pulse and the relatively long RC time constant of 15 ns (later reduced to 5 ns) the midrange gain of the channel is 1.7 instead of its DC value of 2.0 as shown in figure 6.10

Figure 6.11 shows the user interface for the LabView [48] based program used to carry

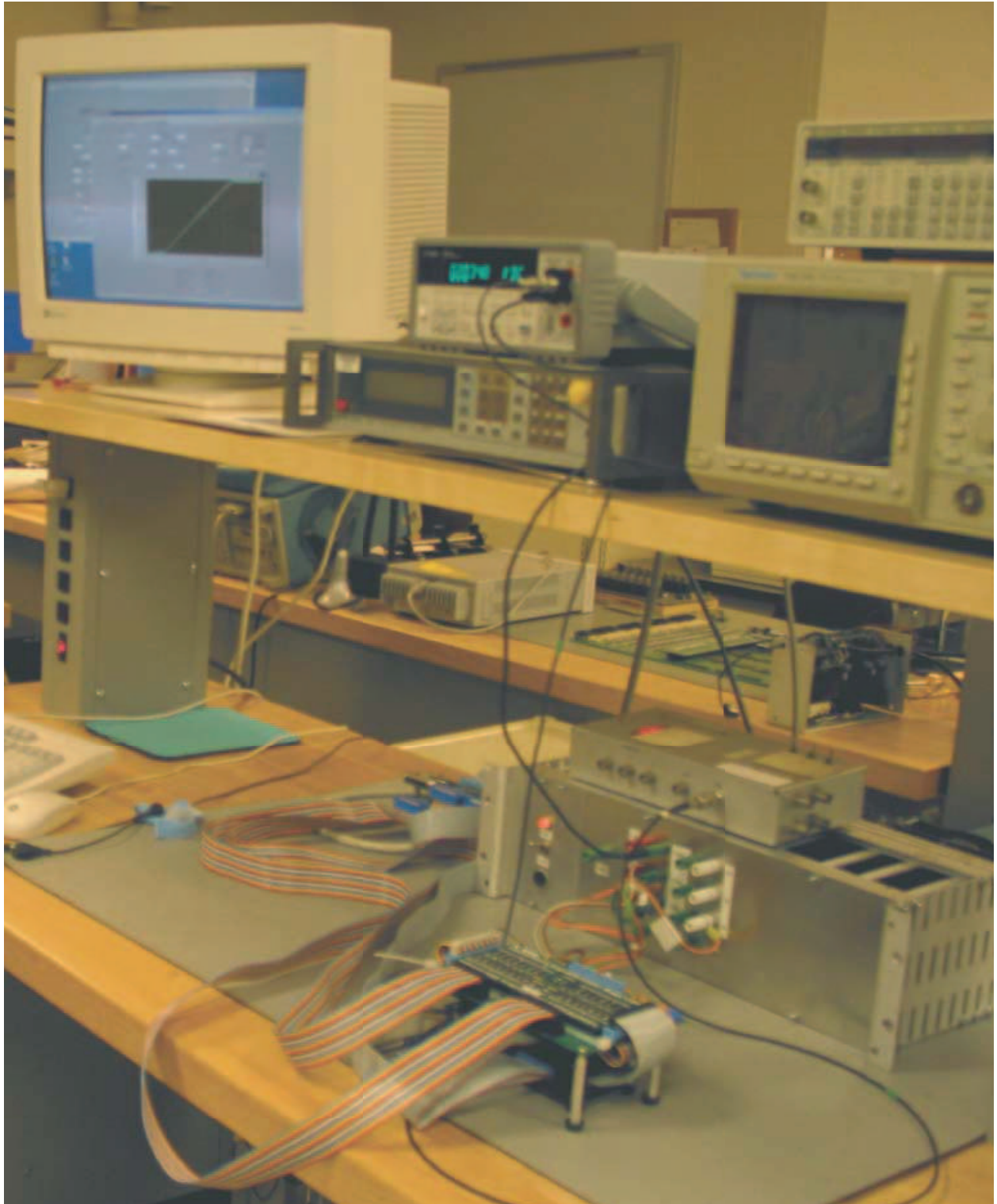


Figure 6.5 VGA daughterboard test bench.

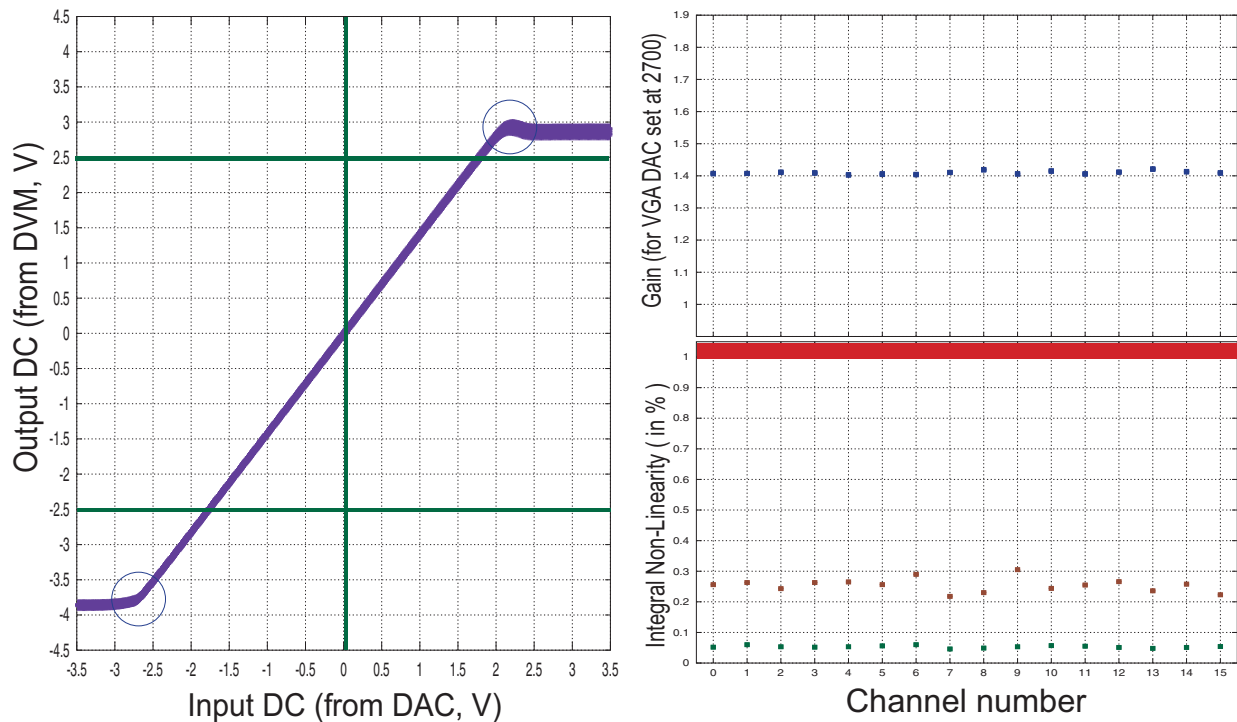


Figure 6.6 Left: DC response curves of the 16 channels of one VGA board, with all channels set at DAC=2700. The green horizontal lines represent the maximum signal amplitude received by the R/M system. The slope of each curve yields a value for the gain, which is plotted in the upper right hand graph. The integral nonlinearity is evaluated separately for the positive and negative portions of the response curve, and the values are plotted in the lower right hand graph. The lower set of points (all below 0.1%) are for the negative region and the upper set of points (between 0.2% and 0.3%) are for the positive region. The thick red line at 1% represents the specification for the nonlinearity for the entire electronics chain in the R/M system.

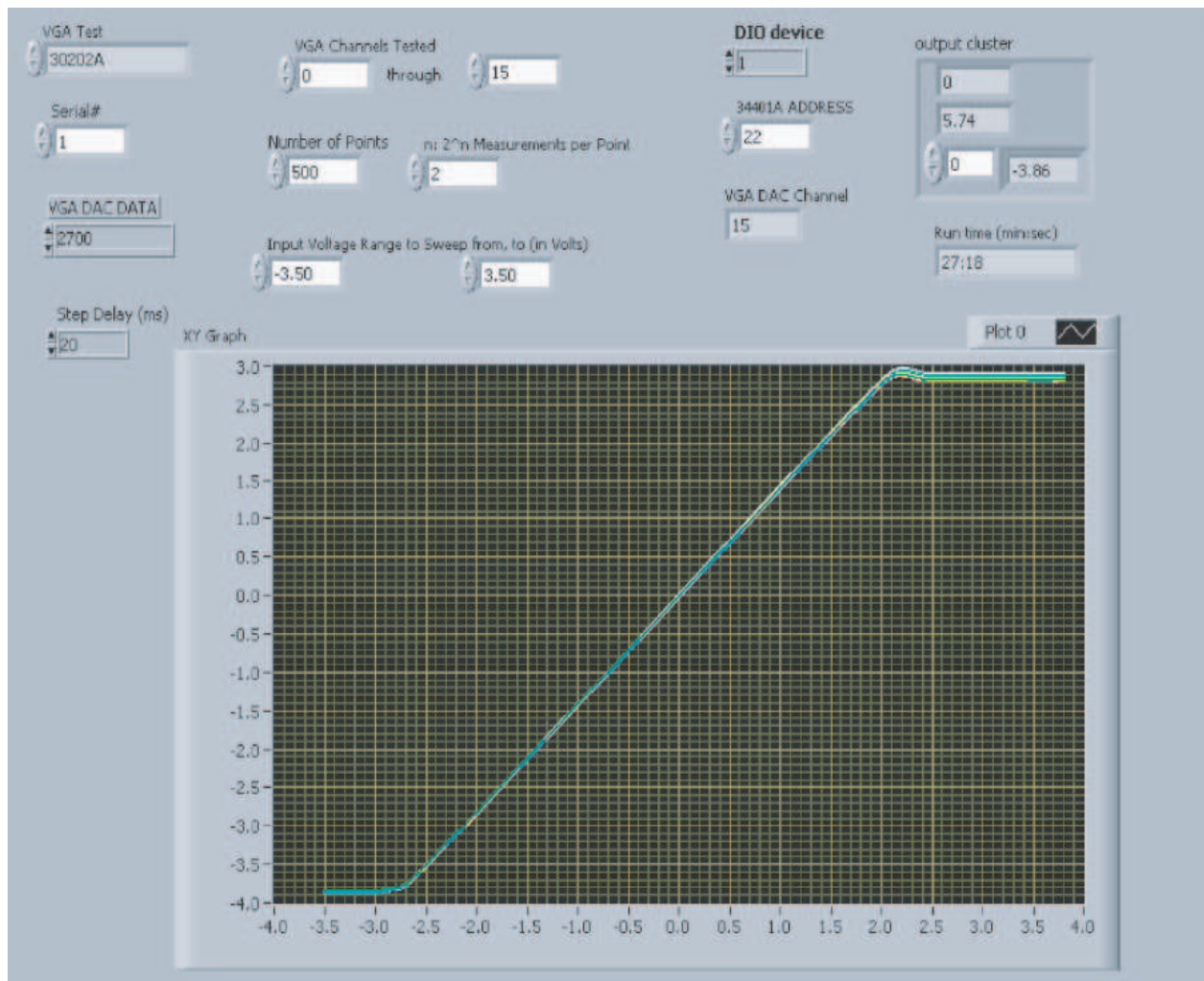


Figure 6.7 Gain and integral nonlinearity for each of the 16 channels of a single VGA board shown in LabView VI's front panel.

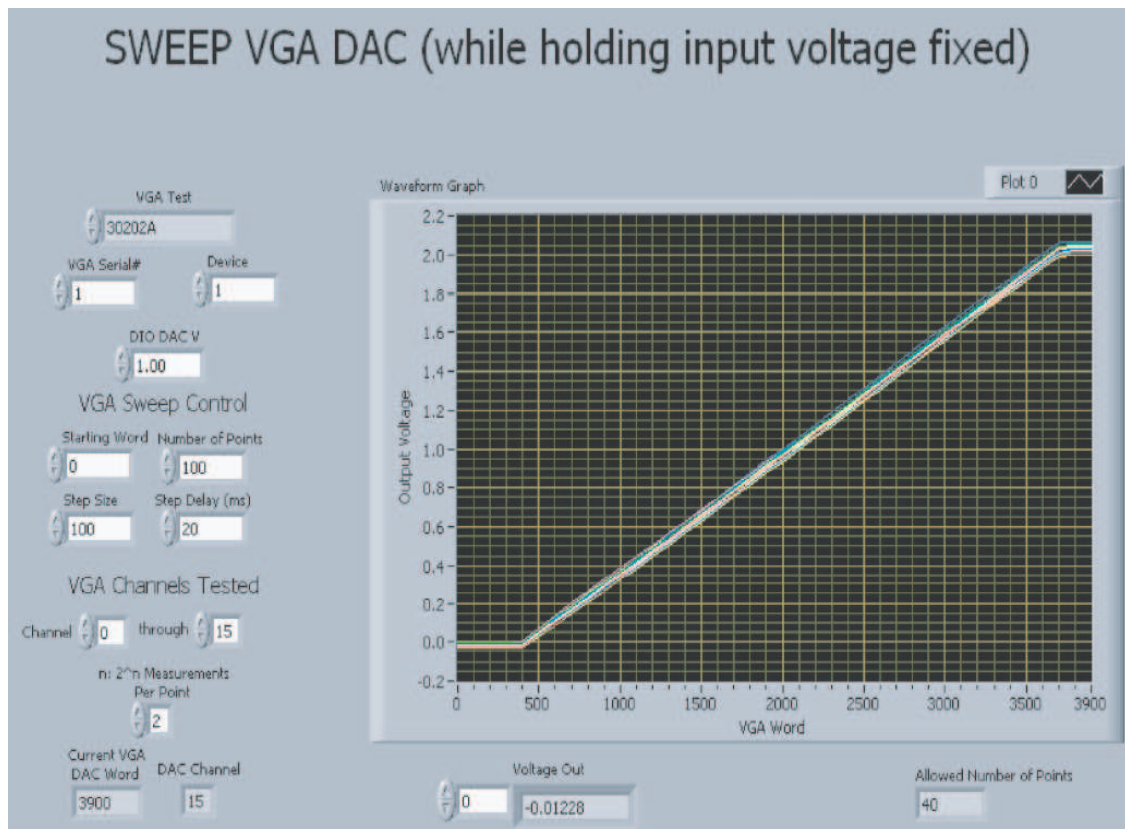


Figure 6.8 DAC linearity for each of the 16 channels of a single VGA board shown in LabView VI's front panel.

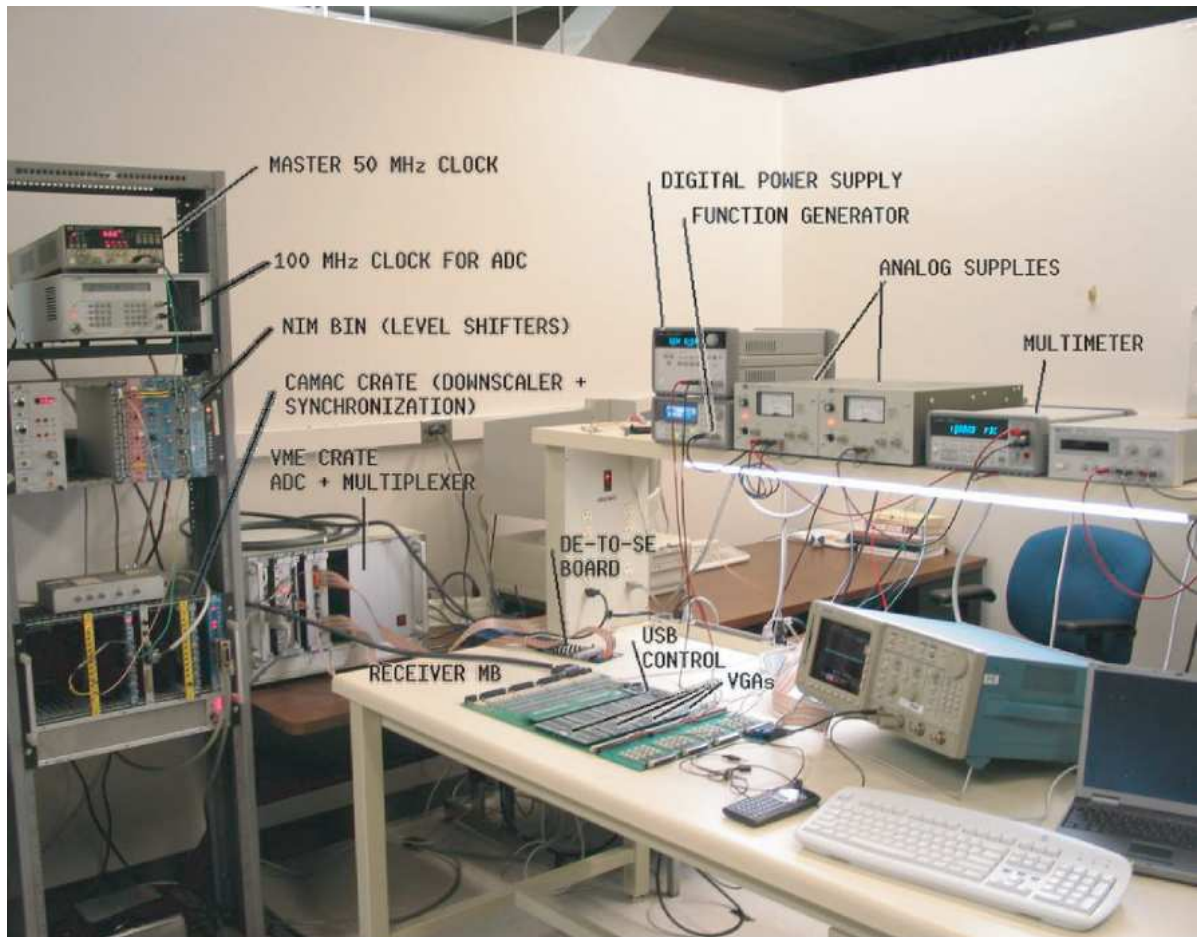


Figure 6.9 R/M system test bench.

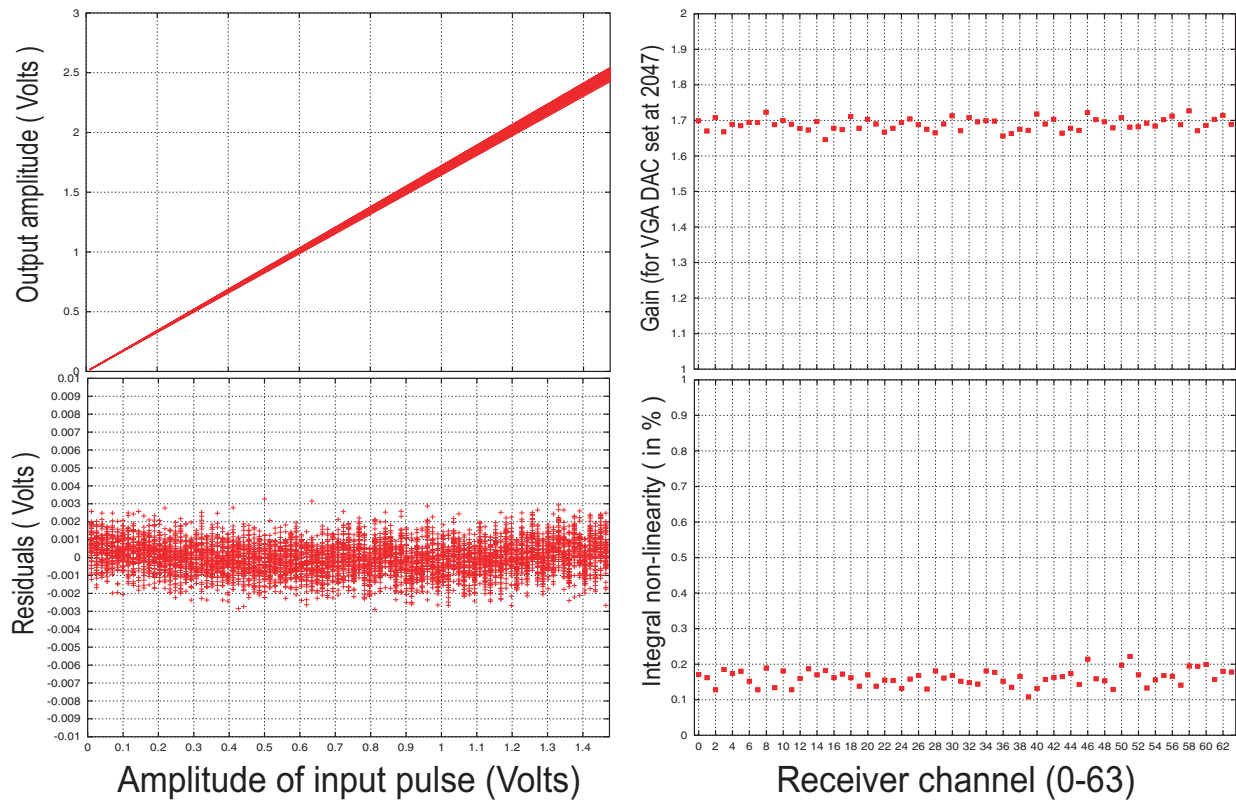


Figure 6.10 Pulse linearity test of the 64 channels of a receiver board, with all the channels set at DAC=2047. Upper left: the response data for a bipolar pulse of 38 ns rise time. Lower left: the residuals of the linear fit of the response data. Upper right: gain value for each channel. Lower right: integral non-linearity (for maximum output pulse height of 2.5 V) for each channel.

out the gain measurements of the receiver circuit. Fig. 6.12 shows a similar interface used to measure the VGA linearity in the receiver chain.

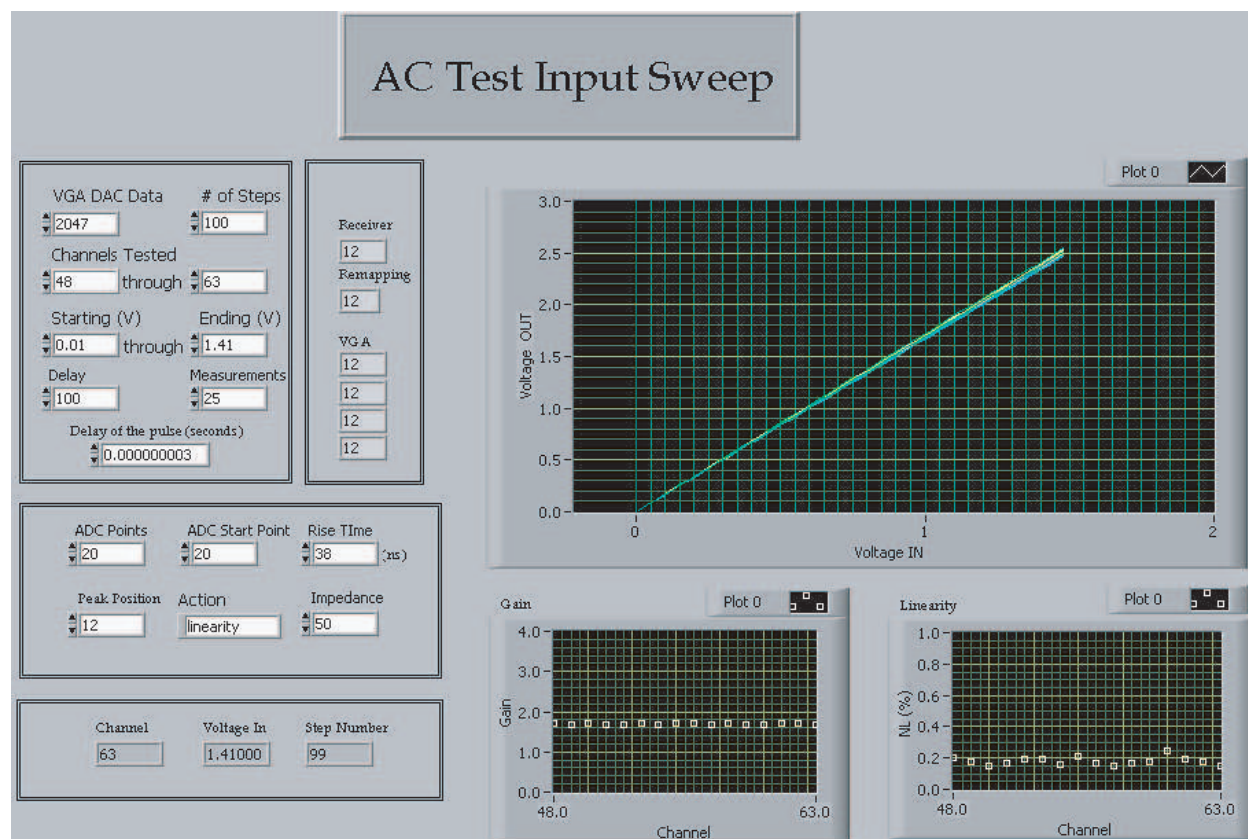


Figure 6.11 Graphical User Interface of the LabView-based program used to carry out test of receiver response to LAr calorimeter signals.

Another important aspect of the receiver is the electronic noise which is contributed into the system by the receiver module. The noise is dominated by the contribution from the VGA integrated circuit, which, according to a model given by the manufacturer [49], depends upon the gain of the circuit. Figure 6.13 shows measured values of the electronic noise at the output of the receiver, along with the evaluation of the noise model for the circuit. The dependence on gain is well described by the model, but it gives values which are approx. 10% higher than the measurements. The agreement is seen as reasonable, given that the VGA chip is being operated with very low gain ( $G=2$ ) compared to the common applications it was originally developed for. The maximum noise seen in the test (where  $\tau=15$  ns) is about 0.5 mV, corresponding to 50 MeV. The reduction of the time constant from 15 ns to 5 ns increases the overall electronic noise to about 0.7 mV or 70 MeV. Typical values of the noise in the trigger sums are  $\approx 500$  MeV. Therefore, the receivers contribute

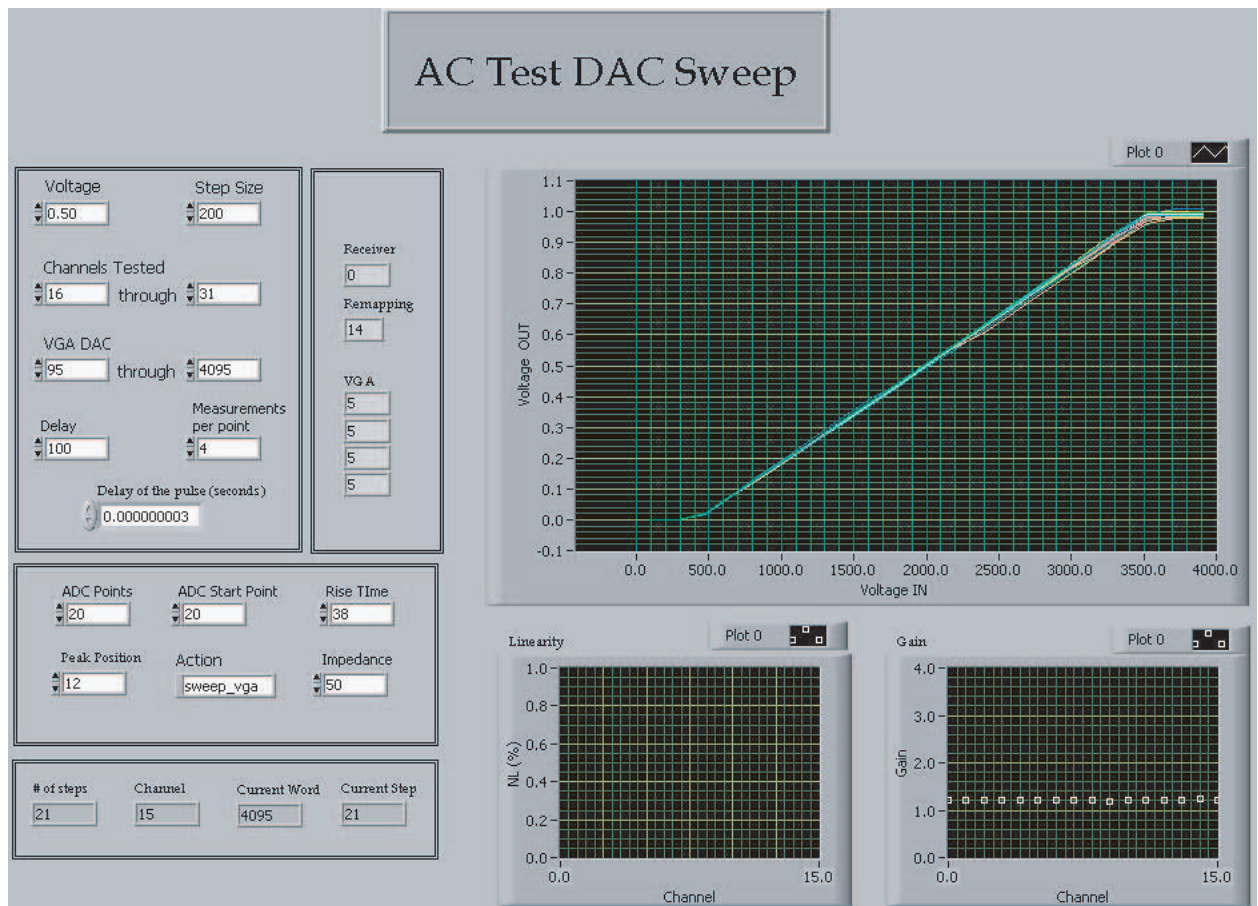


Figure 6.12 Graphical User Interface of the LabView based program used to carry out tests of VGA response to the LAr signals.

relatively small amount of electronic noise to this total amount.

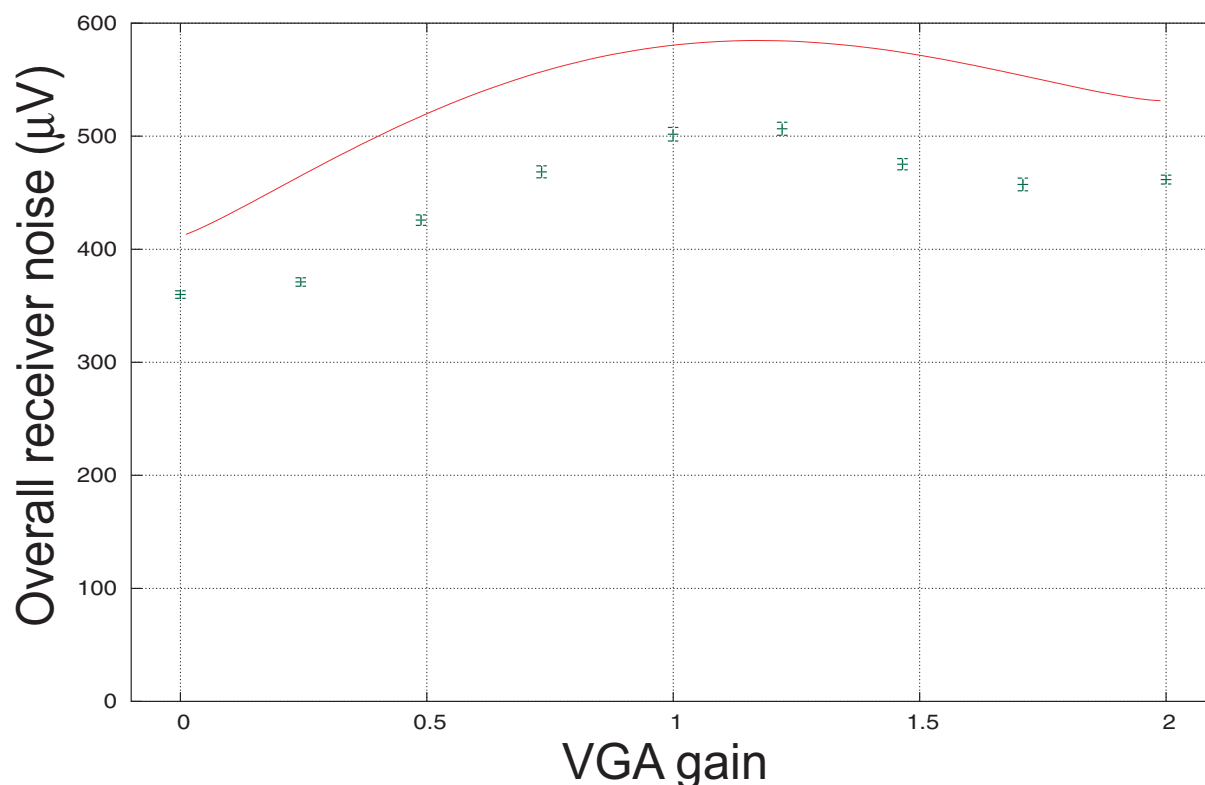


Figure 6.13 Receiver noise vs gain, as measured with a wideband RMS voltmeter at the receiver output. The solid curve is an evaluation of the noise model provided by the manufacturer of the vga chip for this particular circuit of receiver system. The points are the measurements.

Tests of the system's digital logic were also performed using an automated test bench that included Tektronix Prism 3001 Logic Analyzer. Commands were downloaded into the controller, and its output bit pattern in the internal serial link was recorded in the logic analyzer and compared to the standard pattern, produced by a controller known to be operating properly (tested manually). Similar tests were carried out for each SCDB. Any board which failed a test was either repaired, or, in rare cases where repair was not possible, rejected.

Tests of two passive components – the remapping boards and the crate backplane – were also part of the test program. The position of output vs input signals was measured and compared with the required mapping [45]. For the backplane tests, a receiver module was moved systematically from slot 6 to slot 21, while the automated performance tests were carried out. This test not only checked the proper connectivity of the backplane but also validated the operation of the serial link over the full length of the communication paths in

the receiver crate backplane. As a result 128 receiver boards with 512 VGA daughterboards, 128 remapping boards and 8 backplanes were fully tested.

In the final test of the Receiver/Monitoring system all the receiver channels on all the receiver boards were actively tested with the bipolar pulse by routing them to all 16 monitoring channels one by one. In the course of this final QC/QA test the measurements of linearity and gain were also performed. A dedicated LabView-based suite of programs was designed and implemented to exercise the R/M system (see Fig. 6.14). The final QC test was successfully performed on all 8 receiver crates. The receiver crates and circuit boards were then sent to the apparatus site at CERN, Geneva where their installation, commissioning and integration with the rest of ATLAS took place.

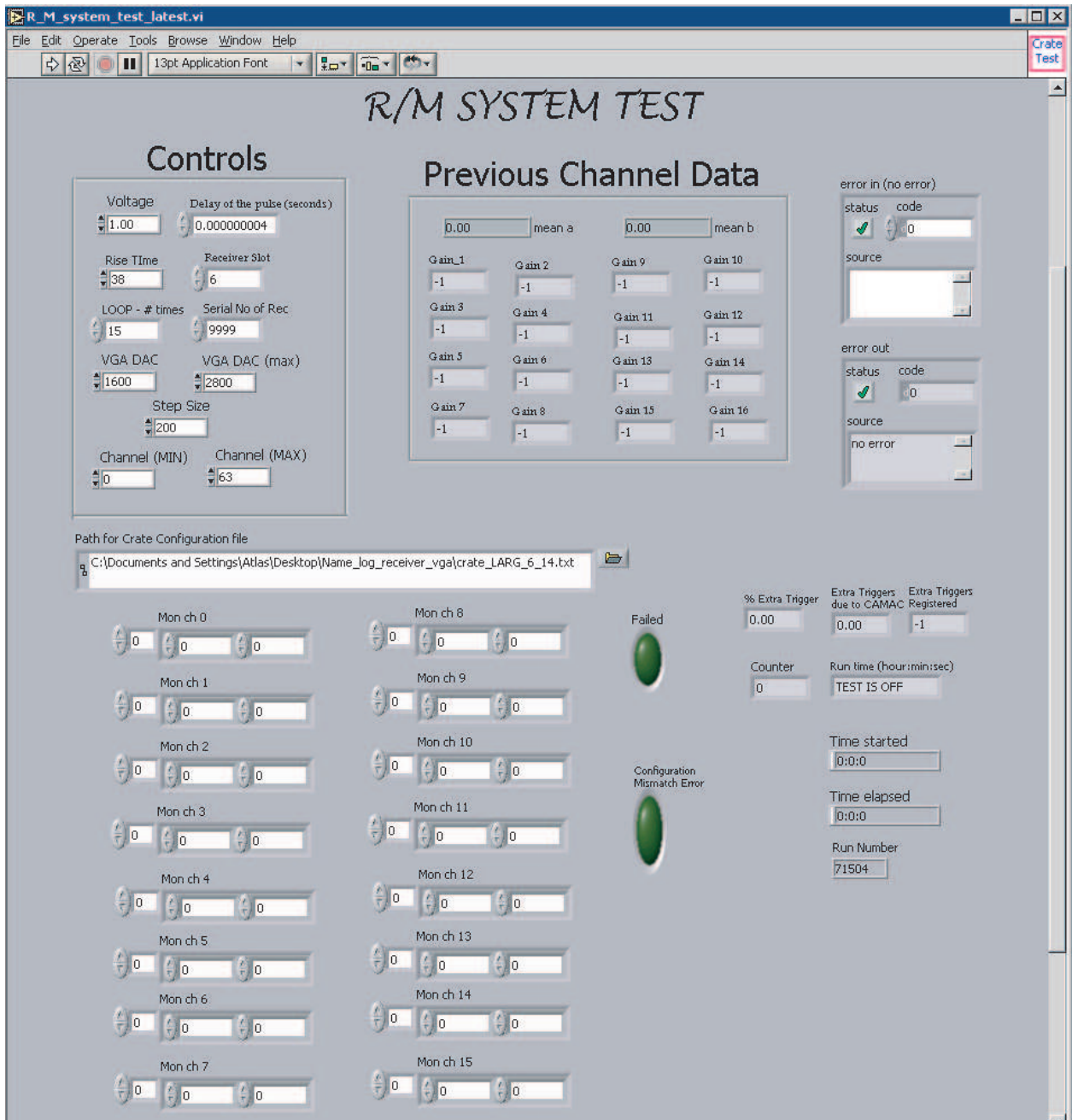


Figure 6.14 Graphical User Interface of the LabView based program used to carry out the final QC/QA of the entire receiver crate.

## 7.0 CONCLUSIONS

The standard model of particle physics exhibits a remarkable symmetry between quarks and leptons which may imply possible existence of undiscovered phenomena. A more fundamental theory could explain the observed symmetry between the two kinds of fermions that are predicted to interact via bosons known as leptoquarks.

This thesis described studies of ATLAS sensitivity to leptoquarks discovery with early LHC data corresponding to an integrated  $pp$  luminosity of  $100 \text{ pb}^{-1}$  at 14 TeV center-of-mass energy. The presented analysis was carried out in the dielectron-dijet final state corresponding to the pair production of leptoquarks. To restrict the parameter space of leptoquarks to mass only, single production of leptoquarks, the process that depends on an unknown Yukawa coupling  $\lambda$ , was not presented in this thesis but will be the subject of future studies.

Assuming that leptoquarks primarily decay into a charged lepton, such as an electron, and a quark, ATLAS would be able to discover the leptoquarks with masses up to 565 GeV at  $5\sigma$  significance level. The 565 GeV mass limit incorporates a conservative estimate of the systematic errors associated with the uncertainties in luminosity, jet energy scale, jet energy resolution, and other measurements.

The studies presented in this PhD thesis also include a substantial body of work on the interface between ATLAS calorimeters and the L1 trigger. This interface, also known as the Receiver/Monitoring (R/M) system had been built and tested at the University of Pittsburgh and later installed at the ATLAS site at CERN, Geneva. Contributions to R/M system's QC/QA, installation, commissioning, and integration with the rest of ATLAS have been described.

The ATLAS experiment is fully operational and ready to record collision data. As soon

as the LHC restarts and the first data are accumulated, the analysis techniques presented in this thesis will be applied to real data.

## BIBLIOGRAPHY

- [1] M.E. Peskin and D.V. Schroeder, *An Introduction to Quantum Field Theory*, (Perseus Books, 1995).
- [2] The LEP Higgs working group, *Search for the Standard Model Higgs boson at LEP*, Phys. Lett. B **565** (2003) 61–75.
- [3] [http://www.fnal.gov/pub/presspass/press\\_releases/Higgs-mass-constraints-20090313.html](http://www.fnal.gov/pub/presspass/press_releases/Higgs-mass-constraints-20090313.html).
- [4] Nilles, H.P., *SUPERSYMMETRY, SUPERGRAVITY AND PARTICLE PHYSICS*, Phys. Rep. **110** (1984) 1–162.
- [5] J. C. Pati and Abdus Salam, *Lepton number as the fourth “color”*, Phys. Rev. D **10** (1974).
- [6] L.F. Abbott and E. Farhi, *Are the weak interactions strong?*, Phys. Lett. B **101** (1981) 69–72.
- [7] E. Eichten, I. Hinchliffe, K.D. Lane and C. Quigg, *Signatures for technicolor*, Phys. Rev. D **34** (1986).
- [8] Howard Georgi and Sheldon L. Glashow, *Unity of all elementary particle forces*, Phys. Rev. Lett. **32** (1974) 438.
- [9] H. Murayama and T. Yanagida, *Viable  $SU(5)$  GUT with Light Leptoquark Bosons*, Mod. Phys. Lett. A **7** (1992).
- [10] J.L. Hewett and T.G. Rizzo, *Low energy phenomenology of superstring-inspired  $E_6$  models*, Phys. Rep. **183** (1989) 193–381.
- [11] W. Buckmuller, R. Ruckl and D. Wyler, *Leptoquarks in lepton-quark collisions*, Phys. Lett. B **191** (1987).
- [12] J. Blumlein, E. Boos, and A. Kryukov, *Leptoquark Pair Production in Hadronic Interactions*, hep-ph (1996).

- [13] J.L. Hewett and S. Pakvasa, *Scalar-leptoquark production at hadronic colliders*, Phys. Rev. D **37** (1988).
- [14] M. Kramer, T. Plehn, M. Spira, and P.M. Zerwas, *Pair Production of Scalar Leptoquarks at the LHC*, hep-ph (2005).
- [15] J. Pumplin, D.R. Stump, J. Huston, H.L. Lai, P. Nadolsky, W.K. Tung, *New Generation of Parton Distributions with Uncertainties from Global QCD Analysis*, JHEP **0207** (2002).
- [16] D. Acosta and S. Blessing, *LEPTOQUARK SEARCHES AT HERA AND THE TEVATRON*, Ann. Rev. Nucl. Part. Sci **49** (1999).
- [17] The DØ Collaboration, Abazov et al., *Search for first-generation scalar leptoquarks in  $p\bar{p}$  collisions at  $s = 1.96\text{TeV}$* , Phys. Rev. D **71** (2005) 071104.
- [18] The CDF Collaboration, D. Acosta et al., *Search for first generation scalar leptoquark in  $p\bar{p}$  collisions at  $\sqrt{s}=1.96\text{ TeV}$* , Phys. Rev. D **72** (2005).
- [19] The DØ Collaboration, Abazov et al., *Search for pair production of second generation scalar leptoquarks in  $p\bar{p}$  collisions at  $\sqrt{s} = 1.96\text{TeV}$* , Phys. Lett. B **636** (2006) 183–190.
- [20] The CDF Collaboration, Abulencia et al., *Search for second-generation scalar leptoquarks in  $p\bar{p}$  collisions at  $\sqrt{s} = 1.96\text{TeV}$* , Phys. Rev. D **73** (2006) 051102.
- [21] Baconnier, Yves ; Brianti, Giorgio (ed.) ; Lebrun, P (ed.) ; Mathewson, A G (ed.) ; Perin, R (ed.) ; Baconnier, Yves (ed.), *LHC : the Large Hadron Collider accelerator project*, Report CERN-AC-93-03-LHC, CERN, 1993.
- [22] Pettersson, T S (ed.) ; Lefèvre, P (ed.), *The Large Hadron Collider : conceptual design*, Preprint CERN-AC-95-05 LHC, CERN, 1995.
- [23] J.M. Campbell, J.W. Huston, W.J. Stirling, *Hard Interactions of Quarks and Gluons: a Primer for LHC Physics*, Rept. Prog. Phys. **70** (2007).
- [24] ATLAS Collaboration, *Atlas Detector and Physics Performance - Technical Design Report Vol. I*, ATLAS TDR 14, CERN/LHCC 99-14.
- [25] The ATLAS Collaboration G. Aad et. al, *The ATLAS Experiment at the CERN Large Hadron Collider*, JINST **3:S08003** (2008).
- [26] J.C. Collins and D.E. Soper, *The Theorems of Perturbative QCD*, Ann. Rev. Nucl. Part. Sci **37** (1987).
- [27] G. Altarelli et. al., *Transverse momentum in Drell-Yan processes*, Phys. Lett. B **76** (1978).

- [28] J.M. Campbell, *Hard Interactions of quarks and gluons: a primer for LHC physics*, Rep. Prog. Phys. **70** (2007).
- [29] Torbjörn Sjöstrand et al., *PYTHIA 6.4 physics and manual*, JHEP **05** (2006).
- [30] G. Corcella et al., *HERWIG 6.4 release note*, hep-ph **0201201** (2001).
- [31] S. Agostinelli et al., *G4—a simulation toolkit*, Nuclear Instruments and Methods in Physics Research Section A: Accelerators, Spectrometers, Detectors and Associated Equipment **506** (2003) 250–303.
- [32] W.R. Leo, *Techniques for Nuclear and Particle Physics Experiments: A how-to approach*, (Springer-Verlag, 1994).
- [33] *ATLAS computing: Technical Design Report*, Technical design report ATLAS, CERN, Geneva, 2005.
- [34] M.Cacciari and C.P.Salam, *Dispelling the  $N^3$  myth for the  $k_t$  jet-finder*, Phys. Lett. B **641** (2006).
- [35] G.C. Blazey et al., *Run II Jet Physics*, arXiv:hep-ex **0005012** (2000).
- [36] ATLANTIS team, *ATLANTIS event display for ATLAS*, <http://www.hep.ucl.ac.uk/atlas/atlantis>.
- [37] <http://www.phys.hawaii.edu/~kirill/FEHiP.htm>, *Fewz*.
- [38] Frixione, Stefano and Webber, Bryan R., *Matching NLO QCD computations and parton shower simulations*, JHEP **06** (2002) 029.
- [39] Bonciani, Roberto and Catani, Stefano and Mangano, Michelangelo L. and Nason, Paolo, *NLL resummation of the heavy-quark hadroproduction cross-section*, Nucl. Phys. **B529** (1998) 424–450.
- [40] The ATLAS Collaboration, *Expected performance of the ATLAS experiment detector, trigger, physics*, Internal Report CERN-OPEN-2008-20, CERN, Geneva, 2008.
- [41] Bitjukov, S. I. and Erofeeva, S. E. and Krasnikov, N. V. and Nikitenko, A. N., *Program for evaluation of significance, confidence intervals and limits by direct calculation of probabilities*, Prepared for PHYSTATO5: Statistical problems in particle physics, astrophysics and cosmology, oxford, england, united kingdom, 12-15 sep 2005, 2005.
- [42] A.D. Martin, R.G. Roberts, W.J. Stirling and R.S. Thorne, *Uncertainties of predictions from parton distributions, I. Experimental errors*, Eur. Phys. J. C **28** (2003).
- [43] N.J. Buchanan et al., *ATLAS liquid argon calorimeter front end electronics*, JINST **3 P09003** (2008) 59.

- [44] W. E. Cleland, et al., *Receiver/Monitor System for the ATLAS Liquid Argon Calorimeters*, Internal Report ATL-AL-EN-0043, 2006.
- [45] V. Paolone, *Remapping Boards for the ATLAS Liquid Argon Receiver System*, Internal Report ATL-AL-EN-0046, 2002.
- [46] W.E. Cleland, et al., *Digital Communications in the ATLAS Receiver/Monitor System*, Internal Report ATL-AL-EN-0048, 2003.
- [47] V. Savinov, *Tests of the Receiver/Monitor Stations for the ATLAS Calorimeters: Part 1*, Internal Report ATL-AL-EN-0049, 2003.
- [48] National Instruments, *LabView*, <http://www.ni.com/labview/>.
- [49] National Semiconductor Corp., *Application Note OA23*, Internal report.

## APPENDIX A

### ELECTRON IDENTIFICATION

Electron candidates are identified by using information on the characteristic energy deposits in the calorimeters (both LAr and Tile), the spacial and the depth distributions of these energy deposits, hits associated with the best-match inner detector track and the agreement between this track and its projection to the LAr calorimeter.

A sketch of the ATLAS calorimeters system 3.2.2 is shown in Fig. A1. The LAr electromagnetic (EM) calorimeter is primarily used to identify electrons and photons. Fig. A2 shows  $\eta$  coverage of the EM calorimeter. Reconstruction of the deposited energies in the various part of the calorimeters is used to identify electron candidates and to suppress backgrounds from single charged hadrons and hadronic jets. Four independent identification methods have been developed on ATLAS to identify electrons. These methods are based on the maximum likelihood approach, the boosted decision trees, the neural net and a set of selection criteria, called **isEM**, applied to the reconstructed quantities. The work presented here is based on **isEM**-based identification. This identification is described in more detail below.

#### A.1 SELECTION CRITERION FOR ISEM IDENTIFICATION

The **isEM** method requires an optimal selection on discriminating variables measured from the calorimeters and the inner detector. By design, the calorimeter response is a func-

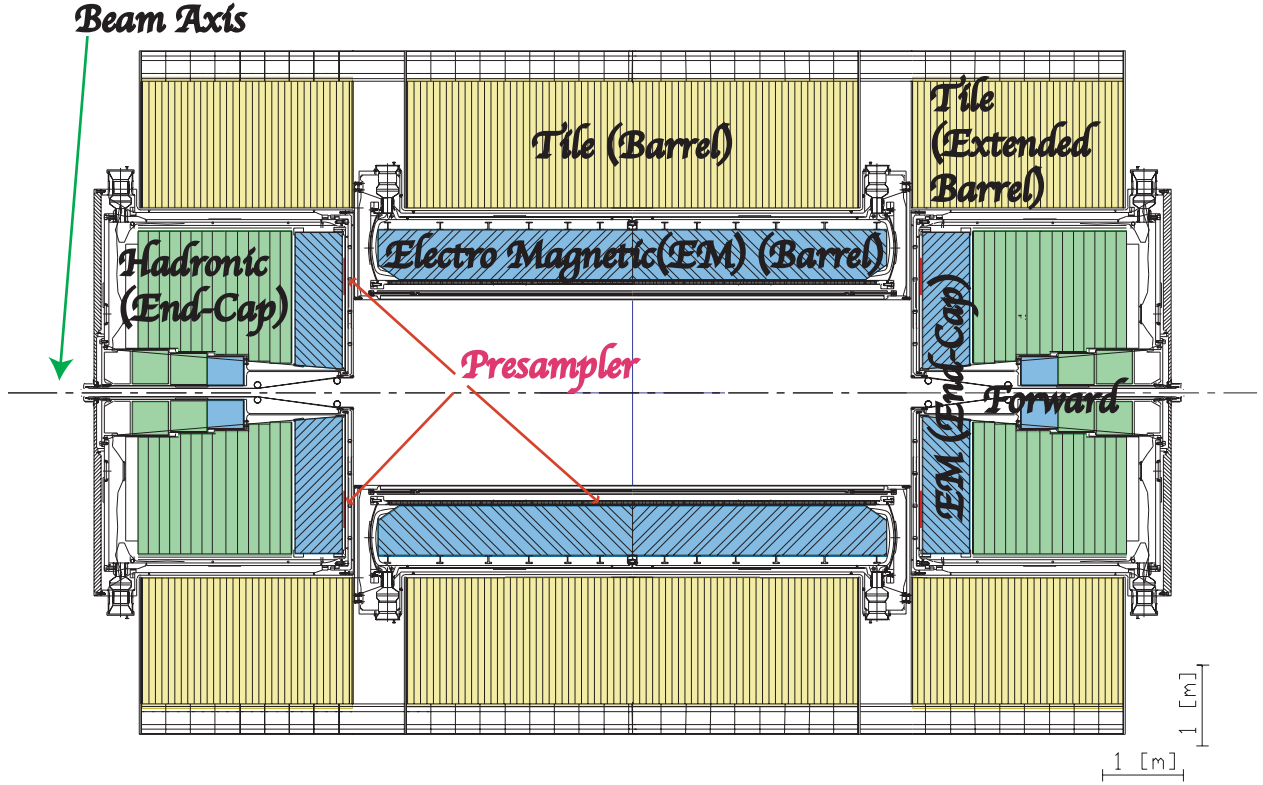


Figure A1 ATLAS calorimeters: longitudinal cross-sectional view.

tion of pseudorapidity. For the purpose of the presented study it is sufficient to study calorimeter response in seven pseudorapidity bins with the upper edge of these bins defined as 0.8, 1.35, 1.5, 1.8, 2.0, 2.35, 2.47. The choice of the bins is determined by the acceptance of various calorimeters. The region  $|\eta| \leq 0.8$  represents the barrel part of EM calorimeters. Endcap calorimeters start at  $|\eta| = 1.35$ , while the barrel extends up to  $|\eta| = 1.5$ . Presampler starts at  $|\eta| = 1.8$ , granularity of the end-cap electromagnetic calorimeters change at  $|\eta| = 2.0$  and  $|\eta| = 2.5$ . For electron identification the LAr energy clusters are required to be at  $|\eta| \leq 2.47$ .

The calorimeter-based variables used to distinguish electrons from hadrons and jets include

- **Hadronic Leakage:** The fraction of the electron’s “transverse energy” – energy in transverse direction – deposited in the first sampling of hadronic calorimeters (see Fig. A3),
- **Lateral shower shape:** The ratio of the energy deposited in  $3 \times 7$  and  $7 \times 7$  cells,

around the cell with the largest energy deposit<sup>1</sup>, in  $\eta \times \phi$  space of the second sampling layer of electromagnetic calorimeter (see Fig. A4),

- **Weighted shower width in the middle sampling layer:** As electrons are likely to shower into a narrower region compared to hadronic jets, RMS of pseudorapidity of cells in cluster weighted by the cells' energy in the second layer of the electromagnetic calorimeter is used as an identification variable. (see Fig. A5),

The energy deposition in the hadronic calorimeter and the second sampling of the electromagnetic calorimeter are used to reject jets with high energy hadrons and wide energy clusters. Jets with single or multiple hadrons pose as the main source of fake electrons. The first sampling layer of the electromagnetic calorimeter, with its very fine granularity in pseudorapidity, can be used to detect substructures within a shower and thus identify  $\pi^0$  and pair-converted photons. To reject such background contribution the following measurements are employed

- **Maximum energy difference:** Pair-conversions and  $\pi^0$  decays often result in two distinct maxima in the first layer of the electromagnetic calorimeter. The difference between the energy of the second “hottest” cell in the first sampling and the energy of the cell with the lowest energy deposit that lies in between the two cells with the largest energy deposit can be used to suppress the backgrounds (see Fig. A6).
- **Second largest deposit:** The second “hottest” cell, as defined above, is chosen only if its energy is above a certain threshold. This is necessary to reduce the sensitivity to the energy fluctuations. The threshold is a function of the transverse energy and is defined as  $1 + 5 \times 10^{-3} E_T$ . The ratio of the energy of this second hottest cell and the threshold is another useful variable (see Fig. A7).
- **Shower width in the first layer** (see Fig. A8).
- **Shower shape core:** Fraction of energy deposited in the core part of the cluster in the first sampling layer of the electromagnetic calorimeter (see Fig. A9).
- **Weighted shower width in the first sampling layer:** RMS of pseudorapidity of cells in the cluster weighted by the cells' energy in the first layer of the electromagnetic

---

<sup>1</sup>This ratio could be larger than 1.0 in the pseudorapidity region [1.37, 152]. This is possible because of the higher level of electronic noise in that part of the detector.

calorimeter (see Fig. A10).

Selection criteria applied to the values of the variables based on information obtained from the inner detector primarily suppress electrons from photon conversions and  $\pi^0$  mesons from jets. These **isEM** variables include the numbers of hits associated with a track in subdetectors as described below.

- The number of hits in the vertexing layer. This variable discriminates against photon conversions and hadrons originating from  $c$  and  $b$  quarks.
- The number of hits in the pixel detectors.
- The number of hits in the SCT detectors.
- The number of hits in the TRT detectors.

Also, a selection is applied to the track's impact parameter, distance of the track perigee from the beam axis. This selection criterion discriminates against the particles from the secondary vertices. Besides quality selection on the measured quantities in the inner detector and calorimeters,  $\eta$  and  $\phi$  differences between that of the cluster and the associated track are also taken into account. The other important quantity used is  $E/|p|$ , which is the ratio of the cluster energy and the track momentum.

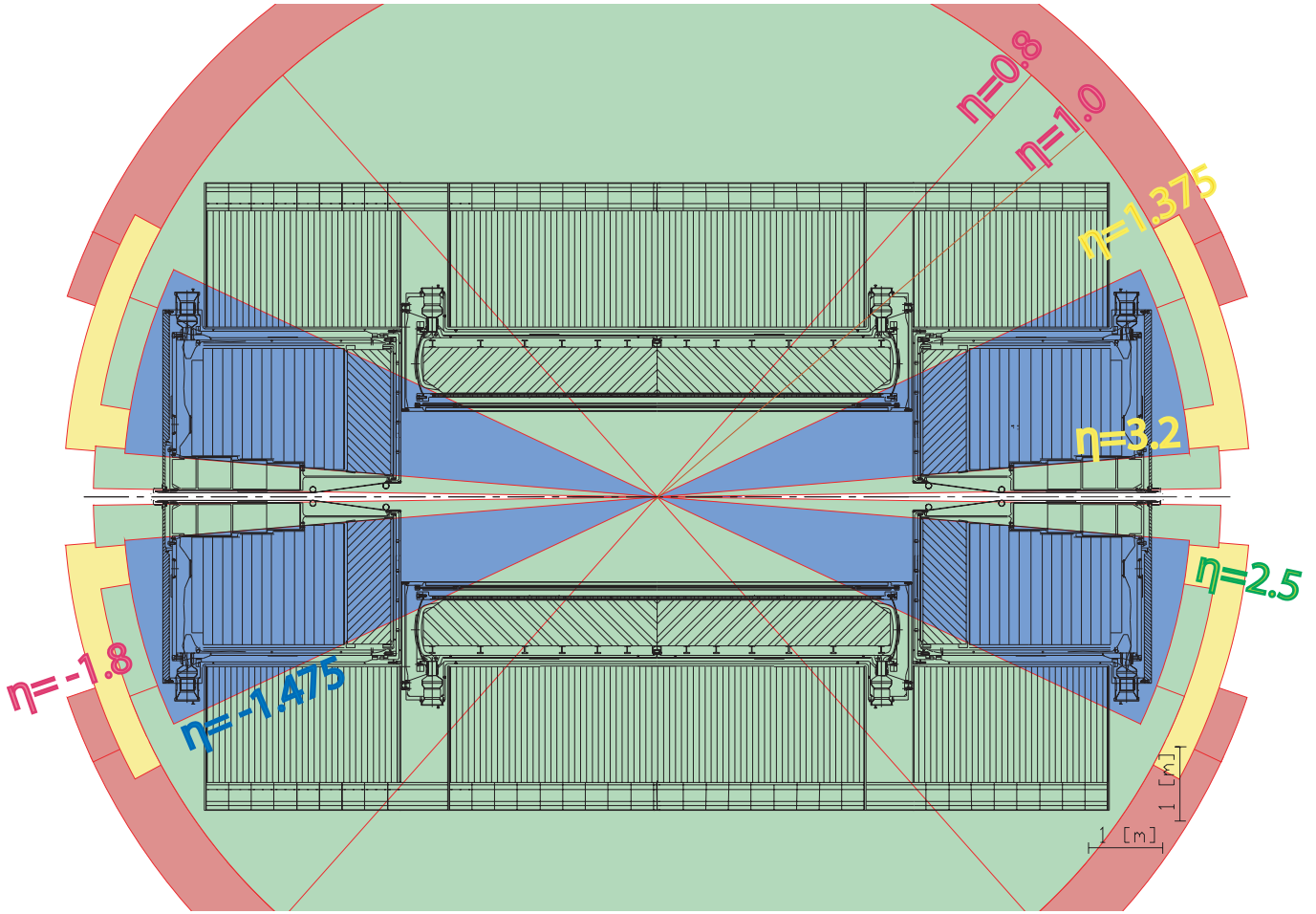


Figure A2 ATLAS calorimeters:  $\eta$  coverage.

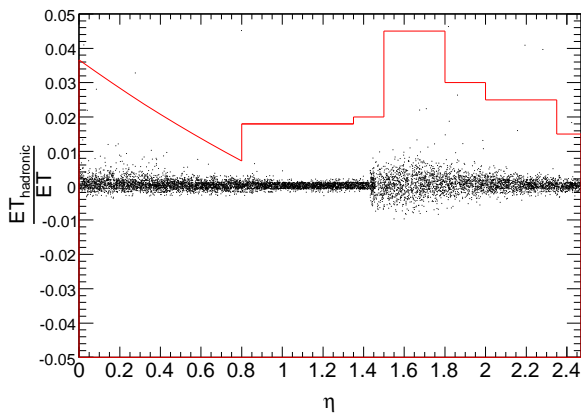


Figure A3 The fraction of the electron's transverse energy in the first sampling layer of a hadronic calorimeter. The red contour defines the optimal selection on this discriminating variable.

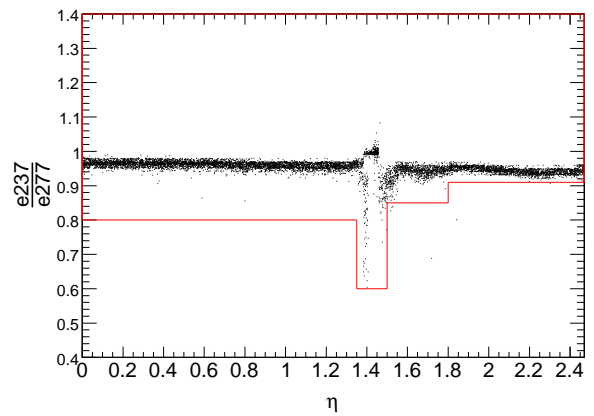


Figure A4 Ratio of energy deposited in  $3 \times 7$  and  $7 \times 7$  cells in  $\eta \times \phi$  space of a second sampling layer of electromagnetic calorimeter. The red contour defines the optimal selection on this discriminating variable.

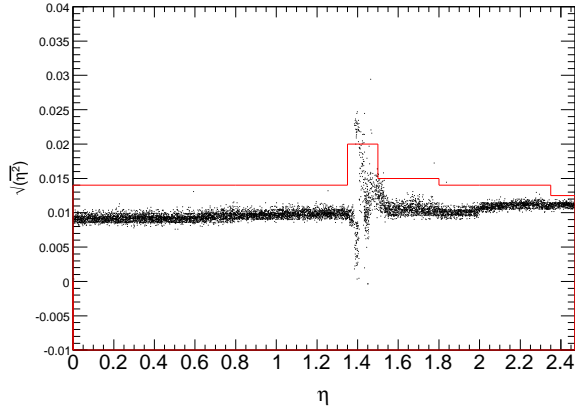


Figure A5 RMS of pseudorapidity of cells in energy clusters weighted by cell energies as detected in the second layer of the electromagnetic calorimeter. The contour in red defines the optimal selection.

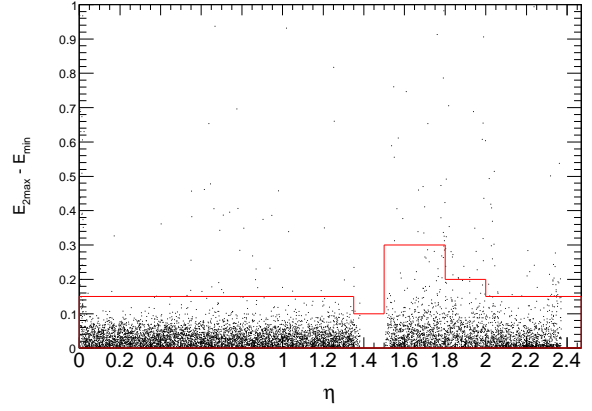


Figure A6 The difference between the energy of the second “hottest” cell in the first sampling and the energy of the cell with the lowest energy deposit that lies in between the two cells with the largest energy deposits. The contour in red defines the optimal selection.

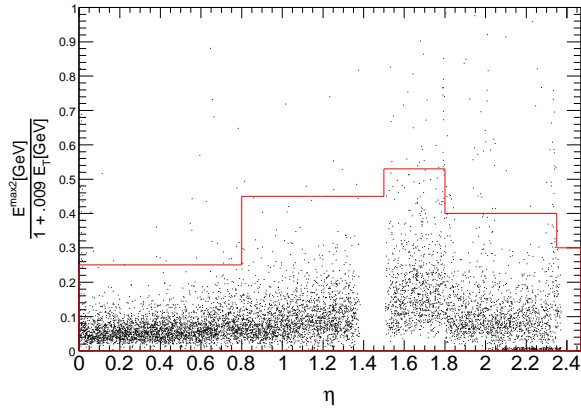


Figure A7 The ratio of the energy of the second hottest cell in the first sampling of the electromagnetic calorimeter and the  $E_T$  dependent threshold. The contour in red defines the optimal selection.

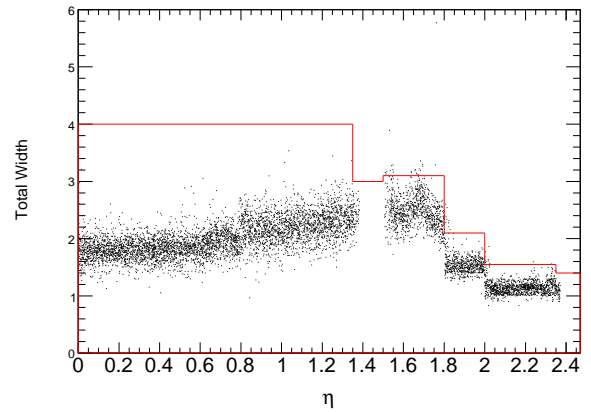


Figure A8 The distribution of the shower shape width in the first sampling layer of the electromagnetic calorimeter. The contour in red defines the optimal selection.

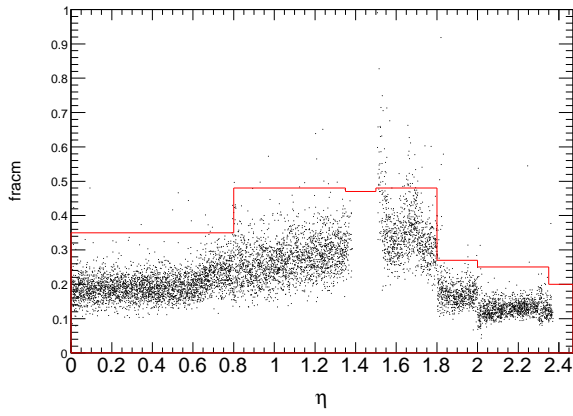


Figure A9 The distribution of the fraction of energy deposited in the core part of clusters from the first sampling layer of the electromagnetic calorimeter. The contour in red defines the optimal selection.

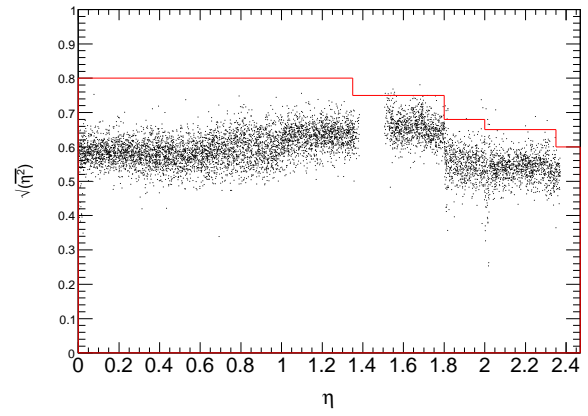


Figure A10 RMS of pseudorapidity of cells in a energy cluster weighted by cell energies detected in the first layer of the electromagnetic calorimeter. The contour in red defines the optimal selection.

## APPENDIX B

### BACKGROUND CONTRIBUTION FROM SINGLE-TOP PRODUCTION

The production of a single top quark accompanied by a charged vector boson  $W$ , i.e.  $tW$  production process, could contribute to two leptons plus jets final states when both the  $W$  bosons decay leptonically. The cross-section for this process is about 1 pb. Unfortunately, the only available MC sample for this process has one  $W$  decaying hadronically and the other  $W$  decaying leptonically. To estimate the number of background events potentially arising from this process in dilepton plus jet channels, the following algorithm was developed.

One signal electron candidate and two jets were selected using the same definitions as described in “first selection criteria” section. Assuming that the selected electron was a daughter of  $W$  that decayed leptonically, and the two selected jets were daughters of the other  $W$  that decayed hadronically, one of these two jets was randomly selected and labelled to be the second signal “electron” candidate with a 60% probability, provided its absolute value of pseudorapidity was less than 2.5. The other jet was then taken to be the associated daughter neutrino. The efficiency of 60% was used to mimic the electron reconstruction and identification efficiency.

This way the two electrons were “identified” as daughters of correspondent  $W$  bosons. To complete the final state, two additional jets were then identified in the events, and the sample was scaled appropriately to correspond to the cross-section of 1 pb. These four final state particles were then studied in the leptoquark analysis. Only 0.007 events survived at  $100 \text{ pb}^{-1}$  luminosity in the analysis. Hence it was concluded that this background process can be safely ignored in this analysis.